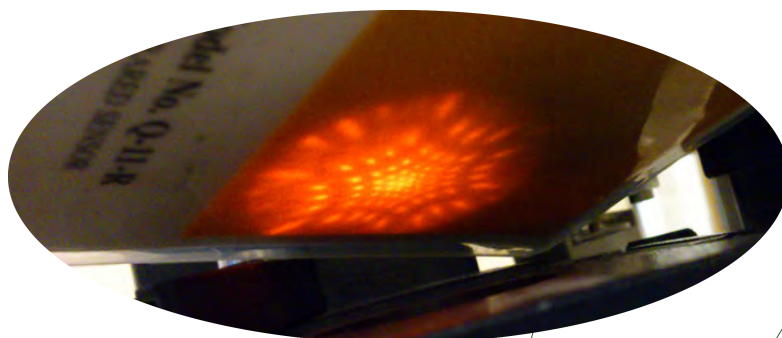# Photodiode based detection for

# multiple trap optical tweezers

Dino Ott

Supervisor:
Prof. Lene B. Oddershede

This thesis has been submitted to the
PhD School of The Faculty of Science,
University of Copenhagen

Niels Bohr Institute
University of Copenhagen
Denmark

June 29, 2015

# Abstract

This thesis is concerned with the position tracking of microscopic, optically trapped particles and the quantification of the forces acting on them. A new detection method for simultaneous, three-dimensional tracking of multiple particles is presented, its performance is evaluated, and its usefulness is illustrated in specific application examples.

Optical traps enable contact-less, all-optical manipulation of microscopic objects. Over the last decades, this laser-based micro-manipulation tool has facilitated numerous exciting discoveries within biology and physics, and it is today regarded as one of the workhorses of biophysical research. There exists a variety of implementations of optical traps, from simple single traps to complex multiple traps with engineered three-dimensional light fields. In comparison to single beam optical traps, multiple beam optical traps offer more freedom in terms of the design of experiments due to the extended manipulation capabilities. However, this advantage typically comes at the price of a more challenging detection of the trapped particles' positions and the forces they experience.

To alleviate these problems, we have developed a new detection technique that is simple, effective and easy-to-implement in existing optical setups. The technique relies on spatial filtering and is compatible with the prevalent photodiode based detection method, i.e., back focal plane interferometry, both in terms of the technical implementation and the subsequent data analysis. The proposed method is demonstrated experimentally, and it is confirmed that hallmarks of photodiode based detection remain valid. Its efficiency is experimentally quantified and the results are supported by simulations.

## Abstract

Two important application cases are explored in more detail: Crosstalk elimination in dual-beam optical traps and the three-dimensional tracking of multiple trapped particles in parallel in holographically generated traps.

Standard dual-beam optical traps rely on polarization states – not only to create the two individual traps, but also to separate the signals from the respective optical traps that contain information about the movement of the trapped particles. Incomplete separation of the two signals, termed crosstalk, compromises the accuracy of position and force measurements. We showed that the presented method can be used in conjunction with the common polarization based signal separation, reducing crosstalk up to five times more efficiently than polarization filtering alone. Experiments employing dual-beam optical traps as, e.g., single molecule studies, profit from this improved crosstalk suppression, guaranteeing more scientific value for the experimental efforts.

Furthermore, this simple and cost-effective technique is useful for position and force detection of particles optically manipulated by holographic optical traps. Holographic optical traps are normally not compatible with photodiode based detection and instead rely on dedicated cameras with high frame rates for particle tracking. It is here shown that the proposed method enables simultaneous detection of multiple particles by photodiodes that feature spatial and temporal resolution superior to established camera based tracking schemes. Notably, particle tracking with high acquisition speeds and accuracy is also possible in the direction parallel to the optical axis of the optical trapping system; a feature that is challenging to achieve using other existing detection methods that are often limited to two-dimensional tracking.

Currently, the presented technique is limited to static traps. In the outlook, possible modifications to the optical setup are proposed that would allow for photodiode based detection of dynamically movable traps.

# Acknowledgments

First of all, I would like to thank my supervisor Professor Lene Oddershede. Lene, thank you so much for the advice and guidance you provided the last three years. I very much enjoyed being part of your group, both scientifically and personally. You created a flexible and dynamic atmosphere, providing room to develop and follow own research ideas, which has been both challenging and valuable. Being allowed to follow new ideas and research directions - and not fearing to fail on some of them - is integral for progress in science. Thank you for trusting in me, guiding me and letting me thrive – I will remember my years as part of your group with fondness.

Nader Reihani has played a central role in my research and has contributed significantly to the progress. Nader, thank you for your thoughtful insights and, especially, for sharing your passion for optics with me. I very much enjoyed our highly productive and creative summer months. Let us make sure that unjust, though all too often existing, prejudices do not separate Denmark and Iran further than the physical distance actually is. My friend, I hope you will spend many more summers in Denmark and that I will visit you soon in Iran.

Furthermore, I would like to thank Kamilla Nørregaard, Nader Reihani, and Florian Biermann for critical reading of the manuscript.

During my visit to Stanford University, I had the great pleasure to work with Manu Prakash and Jim Cybulski. Dear Manu, dear Jim, thank you for a fantastic time in Stanford - you are among the most inspiring people I have ever met in science.

# List of publications

CONTRIBUTIONS TO SCIENTIFIC JOURNALS

- **Ott, D.**, Reihani, S. N. S. & Oddershede, L. B. *Simultaneous three-dimensional tracking of individual signals from multi-trap optical tweezers using fast and accurate photodiode detection.* **Optics Express** 22, 23661 (2014).

- **Ott, D.**, Reihani, S. N. S. & Oddershede, L. B. *Crosstalk elimination in the detection of dual-beam optical tweezers by spatial filtering.* **Review of Scientific Instruments** 85, 053108 (2014).

- Kreysing, M., **Ott, D.** et al. *Dynamic operation of optical fibres beyond the single-mode regime facilitates the orientation of biological cells.* **Nature Communications.** 5, 5481 (2014).

- **Ott, D.**, Bendix, P. M. & Oddershede, L. B. *Revealing Hidden Dynamics within Living Soft Matter.* **ACS Nano** 7, 8333–8339 (2013).

- Andersen, T., Bahadori, A., **Ott, D.** et al. *Nanoscale phase behavior on flat and curved membranes.* **Nanotechnology** 25, 505101 (2014).

PROCEEDINGS

- **Ott, D**., Reihani, S. N. S. & Oddershede, L. B. *Enabling accurate photodiode detection of multiple optical traps by spatial filtering.* **Proc. SPIE** 9164, 916411 (2014).

PATENTS

- **Ott, D.**, Reihani, S. N. S., Oddershede, L. B. *"A detection system for an optical manipulation system for manipulating micro-particles or nano-particles of a sample by means of at least two optical traps"*, International PCT patent, filed 2015.

# Preface

As one sets out on an exploratory research journey, it is impossible to know where the path might lead. I am convinced that counts for a large number of PhD studies and each PhD project has its own unique history – and so does mine. To understand what prompted the research questions and why certain changes happened, follows a short summary of the three year research period that I have spent in the 'Optical Tweezers Group' at the Niels Bohr Institute (University of Copenhagen, Denmark) under the supervision of Professor Lene Broeng Oddershede.

Originally, the aim of this PhD was to investigate the possibility to use optically trapped nanoparticles as ultra sensitive sensors for acoustic vibrations in the context of biophysical research. This idea was based on a paper which was published shortly before the start of my PhD by Ohlinger et al. titled 'Optically trapped gold nanoparticle enables listening at the microscale'. The first step of my PhD project was to build a dual-beam optical trapping setup, on which we planned to conduct the experiments. While the preliminary results looked promising, we realized that crosstalk between the two optical traps not only compromised the accuracy of our results, but also presented a more general problem in the detection of dual-beam optical traps, which are often used in single molecule experiments. When consulting the existing literature, we noted that other researchers had experienced similar problems. This prompted us to think more about this technical problem, and we decided to try finding a solution, before continuing pursuing the original aims of the PhD project. As we succeeded,

we realized that our solution could potentially be used in a more general way to enable three-dimensional simultaneous tracking of multiple particles with high temporal resolution. Excited by this new possibility, we modified the setup and were able to demonstrate the feasibility and advantages of the technique. In summary, the development of this new technique has resulted in two articles in peer-reviewed scientific journals, a contribution as a conference proceedings paper and a filed patent.

By the time we had finished these projects, however, another research group had published what we originally set out for regarding the detection of acoustic oscillations. Consequently, we developed ideas for alternative projects, and we thus led the research in another direction. One project aims at quantifying the minuscule thermophoretic force that acts on a single particle in a temperature gradient. A second one focuses on investigating the interactions between nanoparticles and endothelial cells, which is important in the context of drug delivery and has applications in nanomedicine. Both research projects are still ongoing.

Besides this, I had the possibility to engage myself in several side projects which enriched my research experience. I spend time designing a new setup for our group, a steerable dual-beam optical trap, which was implemented in cooperation with Azra Bahadori and S. Nader S. Reihani. In parallel, I finished work from a previous research visit to Professor Jochen Guck's group at the University of Cambridge on a technique for the all-optically induced rotation of single cells.

When I set out on this journey, it was difficult to say where it would lead me – I am grateful for the detours I took and what my colleagues and I have accomplished.

For reference, all articles that were published in the course of the PhD can be found in the Appendix.

# Contents

# Contents

# 1. Introduction

This introductory chapter aims to provide the reader with an overview of the main project that was worked on during the 3 year PhD period. Other side projects that were pursued during the PhD studies, which collectively fall into the realm of optical systems design, are summarized separately in Chapter 6.

Here, I start by motivating the main project regarding photodiode based detection for multiple trap optical tweezers. Subsequently, the research question is formulated, and a brief presentation of the proposed solution is given.

## 1.1. Photodiode based detection for multiple trap optical tweezers

### 1.1.1. Optical manipulation of microscopic objects

In our perception of the macroscopic world, we normally do not experience that light exerts forces on the objects it interacts with. However, this is actually the case, and on a microscopic scale this becomes much more apparent. In fact, intense light can exert significant forces on microscopic objects of up to several hundreds of piconewtons [Ashkin 2000]. Optical tweezers are a laser based tool that exploits the interaction between the light's electromagnetic fields and matter to hold microscopic objects in defined locations, move them around, and uses them as handles to probe mechanical properties at microscopic length scales [Svoboda and Block 1994]. Since the pioneering work by Arthur Ashkin forty-five years ago [Ashkin 1970], optical trapping has progressed into being one of

the main workhorses of modern biophysical research. To name a few prominent examples, optical trapping has been instrumental in studies on molecular motors, nucleic acid mechanics, microrheology, non-equilibrium thermodynamics, and the motility of microorganisms [Dholakia and Reece 2006; Perkins 2009; Stevenson et al. 2012].

A large variety of technical implementations of optical traps has been presented in the literature. These range from simple static single beam traps, which are essentially not much more than an expanded laser beam that is tightly focused by a microscope objective, to complex optical trapping platforms that enable precise and dynamic three-dimensional control of the trapping fields' intensity distribution, wavefronts and polarization states [Dholakia et al. 2008; Bowman and Padgett 2013]. Said standard optical tweezers and holographic optical traps are the two prevalent implementations of optical traps.

In standard optical tweezers, a laser beam with a flat wavefront is focused by a high numerical aperture (NA) objective, generating a single spot of high field intensity in the focal plane of the objective. This localized volume of high field intensity presents an optical potential well for particles with a refractive index higher than the surrounding medium. These particles are thus drawn into the beam focus where they get optically trapped. To generate holographic optical traps, in comparison, the trapping beam's wavefront can be modified in such a way that a desired intensity distribution is generated in the sample chamber. This can include several hundreds of traps in three-dimensions that can dynamically be moved relative to each other [Schmitz et al. 2005]. Holographic optical traps feature clearly more freedom in terms of manipulation possibilities. Which implementation is chosen for a particular experiment depends typically not only on the required manipulation capabilities, but also on whether the forces that the trapped object experiences are of interest and should be measured.

### 1.1.2. Current challenges in position and force detection

A great strength of optical tweezers is that they enable the measurement of the minuscule forces that act on the trapped particles. Quantification of these forces requires a detection system that both records the time-dependent particle positions and that can be calibrated, such that particle displacements can be related to forces.

The prevalent detection methods are photodiode based back focal plane interferometry and camera based imaging [Neuman and Block 2004]. Typically, interferometric photodiode based detection is preferred for standard single- and dual-beam optical tweezers due to its sensitivity, linearity and bandwidth [Moffitt et al. 2008]. The method enables three-dimensional position and force measurements with sub-nanometer and piconewton accuracy at bandwidths of hundreds of kHz [Gittes and Schmidt 1998; Pralle et al. 1999]. Interferometric detection builds on capturing the fluctuations of an interference pattern that is generated in a Fourier plane relative to the sample plane where the trapping is performed. In the case of multiple trapped objects, their individual detectable interference patterns overlap and cannot be distinguished easily. Thus, the interferometric method cannot directly be used to detect multiple traps simultaneously. This incompatibility is a major shortcoming and has prohibited the use of photodiodes in conjunction with holographic optical traps that offer better manipulation capabilities than standard optical tweezers.

As a result, camera based imaging is the most widely used detection method for holographic optical tweezers. Typically, camera based detection is costly, features a lower temporal and spatial resolution, requires offline data processing and offers only limited tracking capability along the optical axis of the optical system. It readily allows, however, the tracking of several particles in parallel, which is not possible with interferometric detection by photodiodes [Keen et al. 2007; Moffitt et al. 2008; Pacoret and Régnier 2013].

### 1.1.3. Research question

Both interferometric photodiode based detection and camera based imaging feature unique characteristics regarding accuracy, bandwidth and their compatibility with multiple traps. These capabilities and limitations define their current use for position and force detection in optical trapping experiments. This thesis aims at answering the question: *Is it possible to combine photodiode based back focal plane interferometry with optical setups that feature multiple optical traps?* The new detection method should lend itself to the tracking of multiple particles in parallel and would profit from the photodiodes characteristics that include fast signal acquisition rates and high spatial resolution, also along the optical axis of the trapping system. Preferably, the solution should be compatible with established calibration procedures to leverage available software solutions and make its integration into existing setups uncomplicated.

### 1.1.4. Proposed solution

When an object is optically trapped, a fraction of the light of the trapping beam gets scattered by the object, while other parts of the beam pass the object without interacting with it. Interferometric detection relies on recording the light pattern that is generated when these two light fields interfere in a Fourier plane. Technically, the photodiode could be placed directly in the back focal plane of an condenser which is used to collect the scattered and un-scattered light, since this plane is a Fourier plane to the sample plane. In practice, however, the photodiode is not placed in this plane due to spatial constrains and other technical considerations. Instead a relay lens is used to image this Fourier plane onto a second plane where the photodiode gets placed and the interference pattern is recorded. The interesting aspect of this configuration, as illustrated in Figure 1.1, is that an intermediate plane exists which is optically conjugate to the sample plane. One can perform spatial filtering in this intermediate image plane to separate the signal of one trap of interest from the remaining other traps.

One practical implementation for spatial filtering is the use of pinholes. Pinholes enable the selective transmission of the signal originating from one single trap, while the remaining signals are blocked. This transmitted signal can then be captured and analyzed using the standard photodiode based interferometric detection scheme.
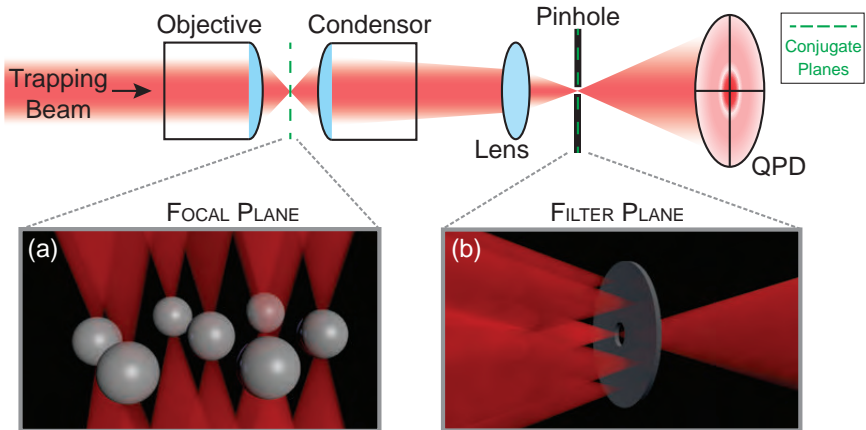


**Figure 1.1.** – **Illustration of the proposed detection method.** An arrangement of multiple optical traps is used to manipulate multiple particles (Inset a). The standard optical layout for photodiode-based interferometric detection is implemented, where a relay lens is used to image the back focal plane of the condenser onto the quadrant photodiode (QPD). Additionally, a spatial filtering device, in this case a small pinhole, is added in the intermediate plane which is optically conjugate the sample plane. The pinhole acts as binary spatial filter and selects a single trap for transmission (Inset b) and subsequent detection by the quadrant photodiode.

## 1.2. Outline of the thesis

The remaining part of the thesis is structured as follows:

First, I present the relevant scientific background and the optical setup that was conceived and implemented (Chapter 2). Following this, results from the evaluation of the proposed technique are discussed (Chapter 3). In the subsequent chapters, I demonstrate how this technique can be used to eliminate

crosstalk in dual-trap optical traps (Chapter 4) and track multiple particles in parallel in holographic optical traps (Chapter 5). Chapter 5 also discusses the limitations of the current implementation and provides an outlook for future work. Chapter 6 contains a summary of the side projects that I was involved in during my PhD. Finally, I present the Conclusions in Chapter 7. All published articles that resulted from the PhD studies are enclosed in the Appendix.

# 2. Background

The purpose of this chapter is to provide an introduction to the field of optical trapping with a focus on certain specific topics that are relevant to the scope of this thesis. Different popular implementations of optical traps are presented, and it is discussed how and why these are typically used in combination with specific types of detection schemes. Moreover, this chapter contains information on the calibration of optical traps, technical aspects of the optical setups that were built, and how the proposed detection method was implemented.

## 2.1. Optical trapping and manipulation

### 2.1.1. Basics of optical trapping

Optical tweezers rely on optical forces that occur when intense laser light interacts with matter. The theoretical explanations of this phenomenon differ depending on the type of the trapping beam, the optical properties of the trapped object, the immersion medium, and the length scale $l$ of the trapped object relative to the wavelength $\lambda$ of the light. In the classical example of a dielectric bead trapped by optical tweezers as, e.g., a polystyrene bead immersed in water, a distinction is made between two regimes called the ray optics regime, where

$$l \gg \lambda \,,$$

and the Rayleigh regime, where

$$l \ll \lambda \,.$$

In the ray optics regime, the optical confinement of particles by the optical trap can be understood in terms of transfer of photon momentum. The basic idea, as illustrated and further detailed in Figure 2.1, is that optical rays are refracted at the surfaces of an object in the focal region of the trapping beam and, since the optical rays have a different direction after the interaction, part of their photon momentum is transferred to the object. For a focused Gaussian beam, the net optical force is directed such that it counteracts a displacement of the bead from its equilibrium position in the center of the trapping beam [Ashkin 1997].

In the Rayleigh regime, on the other hand, the trapping forces can be explained by the electromagnetic interaction between the laser beam and the small dielectric particle. The induced polarization of the particle can be approximated as a point dipole, which interacts with the electric field of the trapping beam. Two forces exerted on the particle can be distinguished, a scattering force $F_{scat}$ and a gradient force $F_{grad}$. The scattering force is acting along the propagation direction of the trapping beam. It is caused by the change in momentum related to the absorption and subsequent re-distribution of light by scattering, and it is proportional to the intensity of the light [Ashkin et al. 1986]. The gradient force arises from the induced dipole minimizing its potential energy in the electromagnetic field of the trapping beam and causes the particle to be attracted to the regions with highest field intensity. The gradient force is proportional to the intensity gradient and the polarizability of the particle. High NA objectives feature steep axial intensity gradients that enable stable trapping in three dimensions, since the gradient forces become sufficiently strong to dominate over the scattering force that would otherwise push the particle out of the trap. While not explicitly discussed here, it should be noted that accurate models have also
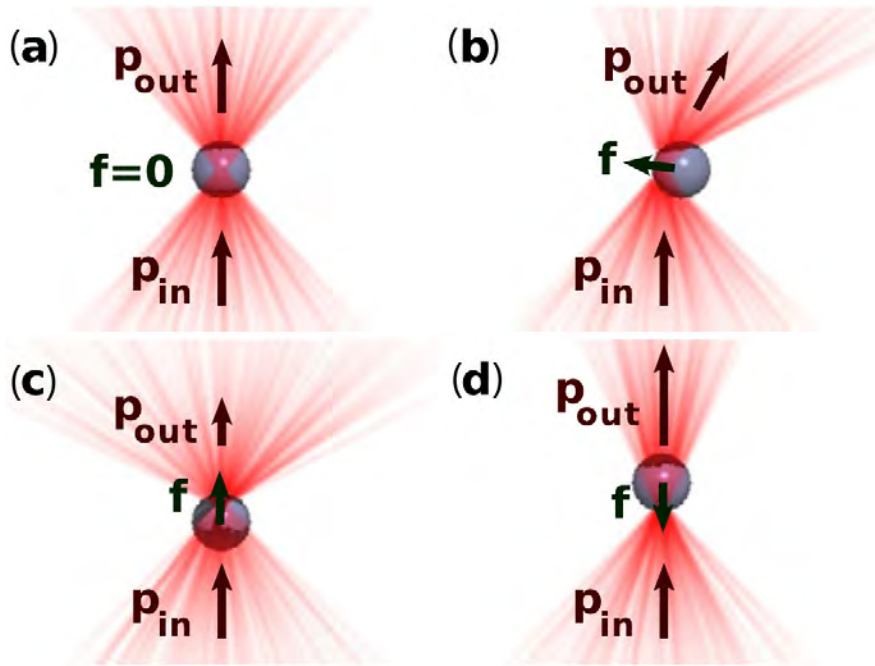
**Figure 2.1.** – **Ray optical representation of optical trapping forces.** A focused Gaussian beam interacts with a spherical object located at different locations relative to the beam focus. (a) For a bead residing at the trap center, no forces act since the incoming and outgoing beams carry the same momentum. (b) In the case of a lateral displacement, the beams are refracted twice at the optical surfaces and ultimately propagate in a direction different from their initial direction. Since light carries momentum, this shift in propagation direction is associated with a change in the light's momentum. The momentum change exerts a force on the object that pulls it laterally towards the center of the Gaussian beam. (c,d) Likewise, at axially offset positions, the momentum of the trapping beam is changed since the divergence of the outgoing beam is different from the incident beam and a net force acts stabilizing the bead axially in its equilibrium position in the optical trap. Figure adapted from [Bowman and Padgett 2013].
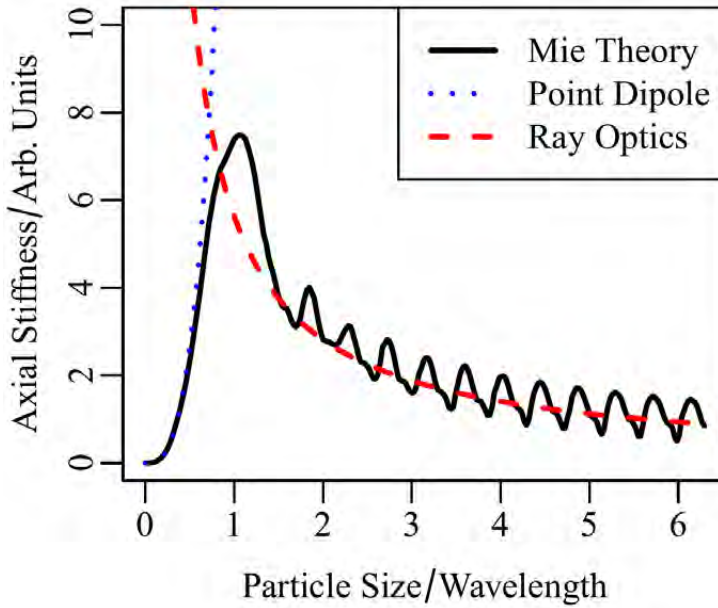
**Figure 2.2.** – **Theoretical models for optical trapping forces.** Comparison of the predicted trap stiffness, a measure for how strong a particle is trapped by an optical trap, by the different theories. The point dipole approximation in the Rayleigh regime is suited for particles small relative to the wavelength, while the ray optics picture captures the situation for larger beads. Predictions based on Mie theory, being more sophisticated, are valid over the full range of particle sizes. Graph adapted from [Bowman and Padgett 2013].

been developed for the intermediate regime where $l \sim \lambda$, since many objects of interest, e.g., biological cells, fall into this size range [Neuman and Block 2004]. The concept in these models is to decompose the trapping field into a superposition of plane waves, employ solutions from Mie theory to calculate the scattering by the trapped object, and subsequently deduce the corresponding forces [Rohrbach 2005]. Figure 2.2 provides an example for the optical forces that are predicted by the different theories for the size range of typically used beads.

### 2.1.2. Common implementations of optical traps

Several different implementations of optical traps have been presented since Ashkin et al. demonstrated the first optical tweezers in 1986 [Ashkin et al. 1986]. Nowadays, the most common techniques are single- and dual-beam optical tweezers and so-called holographic optical traps. Both types of traps were built for and used in this PhD project, and they will be detailed in the following two subsections.

**Single- and dual-beam optical tweezers**

Standard single- and dual-beam optical tweezers are a popular choice for biophysical assays where precise control of two or less objects is required. Classical applications include, e.g., single molecule force spectroscopy studies on nucleic acids and molecular motors [Perkins 2009].

Basic single-beam optical tweezers are easy to implement. In its simplest form, a collimated, expanded Gaussian laser beam is coaxially directed into a high NA objective, creating a single optical trap in the center of the field of view. Beam steering capabilities can be added by introducing optics that allow to pivot the beam around the entrance aperture of the microscope objective. This can be achieved by means of movable lenses, tip-tilt mirrors, or acoustooptical deflectors. The pivot angle corresponds to a well defined lateral displacement of the optical trap in the sample plane [Visscher et al. 1996; Fällman and Axner 1997].

To enable individual manipulation of two separate objects, the polarization of the trapping laser can be exploited. In this approach, two separate trapping beams are generated with perpendicular polarization states, and polarization optics, e.g., polarizing beam-splitters, are used to create two beam paths for independent beam steering [Neuman and Block 2004]. Regarding dual-beam optical tweezers, it is worth noting that the two available polarization states limit the number of optical traps to two.

An interesting extension to this technique which alleviates this limitation are time-shared optical tweezers. Here, a single laser beam is scanned quickly to different trapping locations using fast acoustooptical deflectors (AODs). Trapped objects are insensitive to this high frequency switching of the trapping beam, with typical scanning rates above 20kHz, and thus multiple optical traps can be generated from a single light source [Visscher et al. 1996].

**Holographic optical traps**

Alternatively, multiple traps can also be generated from a single laser beam at once using a technique called holographic optical trapping (Fig. 2.3). As the name suggests, the method borrows from holography to create arbitrary light fields in the sample plane from a single laser beam. To achieve this, holograms are imprinted onto the trapping beam in a Fourier plane, e.g., the back focal plane of the microscope objective. Both static and dynamic diffractive optical elements, like computer-controlled spatial light modulators (SLMs), can be used to modulate the phase of the incident laser beam [Dufresne and Grier 1998; Grier and Roichman 2006]. By being able to impart arbitrary phase patterns, it is possible to dynamically create optical trapping landscapes that include hundreds of optical traps with adjustable trap shapes and positions in the focal volume. The required phase modulations can be calculated efficiently by iterative Fourier transform algorithms, like the Gerchberg-Saxton algorithm and variations thereof [Bowman and Padgett 2013]. Today, holographic optical trapping is among the most used techniques for creating multiple traps.

## 2.2. Position tracking and force measurements

Alongside enabling the manipulation of particles, optical traps are highly sensitive tools for microscopic force measurements. When an external force acts on a bead in an optical trap, the trapped bead is displaced from its equilibrium
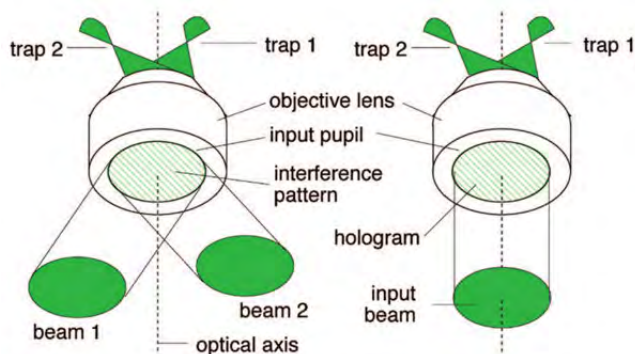
**Figure 2.3.** – **Illustration of the principle behind holographic optical trap generation.** (left) Two beams that are send into a microscope objective at an angle to each other creating two laterally offset optical traps. (right) The same two traps can be generated with a single trapping beam by placing a hologram, which matches the interference pattern that would be formed in the previous 'two beam' method, in the entrance pupil of the microscope objective. Figure adapted from [Grier and Roichman 2006].

position in the center of the trap until the restoring optical force balances the external force. Assuming the position of the bead and the optical potential of the optical trap is known, it is possible to deduce the magnitude and direction of the force that caused the displacement.

Said optical potential can be measured using one of several established calibration methods. In this characterization of an optical trap, which is typically conducted prior to a force measurement, a quantitative relation between the displacement and the restoring force is established by determining the so-called trap stiffness. This will be discussed in detail in Section 2.2.4.

To know the particle's location in the optical potential, a broad range of techniques has been developed to precisely track the movement of the trapped object. Broadly speaking, these can be grouped into two categories – camera based and laser based detection systems. On the next pages, an overview of these available techniques is provided.

## 2.2.1. Camera based techniques

Camera based tracking techniques rely on image analysis to pinpoint particle positions in individual frames of videos captured at high speed. Classically, center-of-mass finding algorithms are used to determine and track the particles' movement in consecutive images. Using specialized algorithms, particle positions can be determined with an accuracy of a fraction of a pixel, i.e., around a few nanometers [Keen et al. 2007; Gibson et al. 2008; Bowman and Padgett 2013]. Traditional cameras, with frame rates of a few tens of Hertz, are sufficient to follow slow processes, e.g., to capture the average position of trapped beads. However, processes that occur at shorter timescales or higher velocities are often of interest and higher frame rates become necessary. Moreover, fast data acquisition allows capturing the trapped bead's rapid temperature-dependent jiggling around its equilibrium position, which is caused by the stochastic collisions with the molecules of the surrounding medium. Recordings of these bead fluctuations can be used to calibrate the optical trap and deduce the trap stiffness. To capture these fast dynamics, high speed video cameras with frame rates on the order of several kHz are used, which have become available and less expensive in recent years. To increase the frame rates, it is typically also necessary to limit the read-out to a smaller subset of pixels, as this decreases the readout time; however, at the expense of a reduced imaging area.

Dedicated "smart cameras" with integrated image and data processing have pushed the boundaries of fast image acquisition to the millisecond range [Di Leonardo et al. 2007; Gibson et al. 2008; Towrie et al. 2009]. Ultimately, the achievable frame rates are limited by the number of detectable photons per captured image. The faster image acquisition reduces the number of arriving photons per image resulting in a low signal-to-noise ratio. Combing specialized cameras with optical fiber delivered high radiance illumination, it is possible to improve this signal-to-noise ratio and reach, for a low number of particles, frame rates of a few kHz with real-time analysis [Otto et al. 2010; Huhle et al. 2015].

While the image analysis is rather straight-forward and computationally efficient for two-dimensional tracking in the imaging plane, it has proven challenging to extend the technique to three-dimensional displacement detection. Recent approaches to enable and improve this axial detection include both purely software based solutions and modifications to the imaging setup. Purely software based solutions extract information about the z-position of the bead, i.e, along the optical axis of the imaging system, by taking advantage of the fact that the appearance of the bead in recorded two-dimensional images depends on the z-position relative to the imaging plane. The alternative approach is to modify the imaging system itself to add axial detection capabilities. Both stereoscopic imaging [Bowman et al. 2010; Hay et al. 2014], where the sample is viewed from various angles, and point spread function engineering [Conkey et al. 2011] have been shown to improve the spatial and temporal resolution of axial detection substantially.

Another interesting, recent approach is to implement imaging systems that use coherent illumination [Lee et al. 2007a; Cheong et al. 2009, 2010]. By capturing and analyzing interferograms of the trapped beads, information about the axial position can be inferred (see Fig. 2.4). As these holographic schemes require coherent illumination, spatial resolution is challenged by speckle and crosstalk between the individual holograms [Conkey et al. 2011]. Still, remarkably precise tracking with nanometer accuracy has been demonstrated both in lateral and axial directions. The setbacks of this technique are that the temporal resolution is low and that the image analysis is computationally demanding, thus prohibiting on-the-fly analysis at the required high frame rates [Cheong et al. 2009; Padgett and Di Leonardo 2011]. The rapidly progressing development of graphics processing units (GPUs) and their use to accelerate image analysis will presumably help to push the limit towards real-time analysis with frame rates of several kHz.
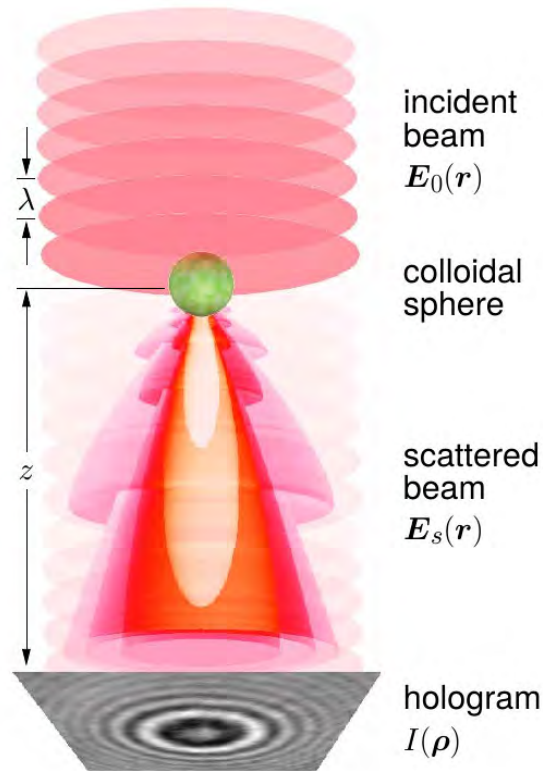
**Figure 2.4.** – **Principle of holographic tracking schemes.** The sample plane is illuminated with a coherent laser beam. In the presence of an particle a fraction of the beam is scattered. This scattering signal interferes with the unscattered light, producing an interferogram that depends sensitively on the particle position. Analysis of the interference fringes and comparison with predictions based on Mie theory allow to extract information about the lateral and axial particle position. Illustration adapted from [Lee et al. 2007a].

### 2.2.2. Laser based techniques

Techniques that involve a tracking laser and photodetectors enable significantly faster detection than cameras because shot noise does not limit the acquisition speeds until very high frequencies due to the high flux at the detector [Visscher et al. 1996]. An early technique that employs this instrumentation are optical trapping interferometers. Here, two slightly offset trapping beams in perpendicular polarization states are created using Wollaston prisms, in a configuration similar to DIC microscopy. Displacements of the bead from the trap center cause a change in polarization, which serves as a highly sensitive read-out signal for the bead position [Svoboda and Block 1994].

Alternatively, the unmodified trapping beam of single-beam optical tweezers itself can be used to measure particle displacements. One early implementation was to replace the camera, which was classically used to image the trapped particle, with a quadrant photodiode facilitating significantly improved temporal resolution [Finer et al. 1994].

However, there are several advantages of locating the position detector in a non-imaging plane instead; namely both easier alignment and improved tracking performance in general. The most common technique featuring this configuration is so-called back focal plane interferometry [Visscher et al. 1996; Gittes and Schmidt 1998]. Here, the changes of the interference pattern in the back focal plane of a light collecting condenser are used to infer the particle motion (see Fig. 2.5). In the focal region, a portion of the trapping beam's light is scattered by the trapped particle, while a second portion passes through the focus unscattered. Due to coherence, an interference pattern is generated in the back focal plane of the condenser, which is a Fourier plane to the sample plane. This interference pattern is then imaged onto a photodetector recording the intensity fluctuations as voltage signals. Quadrant photodiodes are a popular choice, but position sensitive detectors can be used as well [Huisstede et al. 2005].

In the case of a quadrant photodiode, the fluctuations in the differential signal of two opposing halves of the quadrant photodiode provide information about the lateral movement of the particle. The captured voltage signals can be related to lateral displacements in metric units of distance in a calibration procedure, as detailed later in Section 2.2.4. It is important to note that in this configuration, the interference pattern becomes sensitive to the *relative* displacement of the bead from its equilibrium position, instead of being sensitive to the absolute position in the microscope's field of view. Setups that capture the forward scattered light are the standard, but back focal plane interferometry has also been implemented in reflection based geometry where the backward scattered light is detected instead [Huisstede et al. 2005].

Besides lateral displacements, it is also possible to detect axial movement of the bead [Pralle et al. 1999]. Similar to its lateral counterpart, it is fluctuations of the interference pattern that provide a read-out of the particle's axial location. Here it is, however, the changes in total intensity that carry the position information. These fluctuations stem from the Gouy phase, i.e., a $\pi$ phase shift acquired by a laser beam going through a focus, that renders the scattered signal sensitive to the axial position of the trapped bead [Neuman and Block 2004]. The axial detection sensitivity depends on the opening angle of the detection cone defined by the numerical aperture of the condenser and can be optimized by restricting the aperture of the condenser [Dreyer et al. 2004; Friedrich and Rohrbach 2012].

Notably, direct measurement of forces, without the intermediate step of measuring positions and relating these to forces, has recently been demonstrated. This concept relies on precisely determining the momentum change of the trapping beam, which is a direct measurement of the optical force that acts on the particle [Neuman and Block 2004; Farré et al. 2012].

Photodiodes are unrivaled in terms of the bandwidth and resolution they offer. An especially impressive demonstration of these capabilities was recently
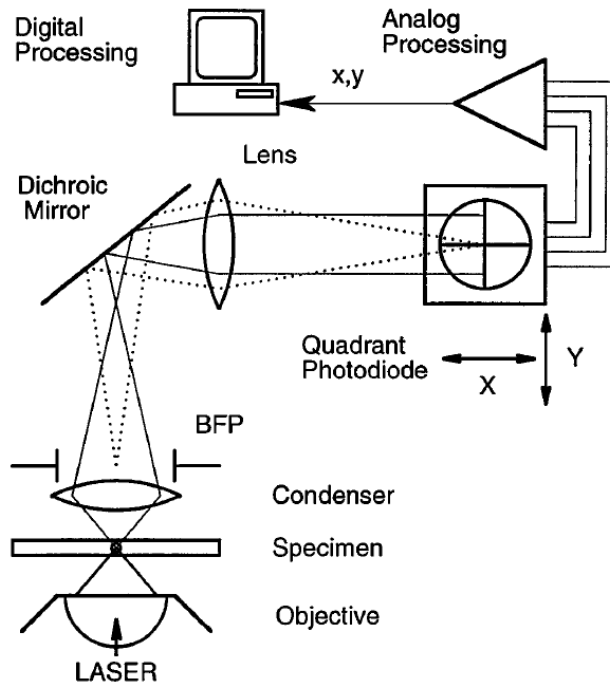
**Figure 2.5. – Back focal plane interferometry.** A high numerical aperture condenser is used to collect the forward scattered and the unscattered light from the sample chamber. The resulting interference pattern in the back focal plane (BFP) of the condenser is imaged onto a quadrant photodiode by a relay lens. This imaging is indicated by dotted lines. Differential signals from opposing halves of the quadrant photodiode provide information about the particles position in the optical trap. Illustration adapted from [Gittes and Schmidt 1998].

reported by Huang et al., who captured the transition from diffusive to ballistic movement of a Brownian particle in an optical trap at a bandwidth of 75 MHz and sub-ångström resolution using fiber-coupled photodiodes [Huang et al. 2011].

Extending this laser- and photodiode based detection to multiple optical traps, e.g, holographic optical traps, where multiple beads are to be monitored in parallel has proven challenging [Moffitt et al. 2008; Marsà et al. 2013]. One solution, following the same line of thought as in the generation of dual-beam optical traps, was to create one trap in a polarization state perpendicular to the remaining traps. The signal from this orthogonally polarized trap is then easily separated from the other signals by polarization based filtering before the photodiode [Dame et al. 2006; Noom et al. 2007; Marsà et al. 2013]. On the positive side, this allows for particle tracking in a back focal plane interferometry configuration. On the downside, however, while multiple particles can be *manipulated*, the two available polarization states limit the number of *detectable* traps to a single one.

Other interesting approaches are sequential detection and calibration schemes. A sequential photodiode based calibration method for holographic optical traps was suggested by van der Horst and Forde. Assuring that only one single particle is trapped at all times, the fluctuations of the interference pattern stem solely from the single occupied trap and an interferometric photodiode based calibration is possible [van der Horst and Forde 2008]. Whether this approach of calibrating one trap at a time is feasible and advantageous depends on the experimental conditions and protocol.

For time-shared optical traps, the possibility to implement back focal plane interferometry comes quite naturally. Since the traps are generated in a time-shared fashion, the signals from the individual traps reaching the photodiode are also separated in time. By synchronizing the read-out of the quadrant photodiode with the duty cycle of the trapping laser, the particles' movement can

| Techniques | Ref. | Dim | Price (K€) | Illumination | Acquisition | Image processing | Algorithm |
|---|---|---|---|---|---|---|---|
| Interferometer | 63 | 1D | € € € € | Laser | 100 kHz | ... | ... |
| Back focal plane | 20 | 3D | € | Laser | 850 kHz | ... | ... |
| Photodiode imaging | 47 | 2D | € | Tungsten 100W | 2 kHz | ... | ... |
| Fast CMOS | 65 | 2D | € € | Halogen 100W | 2 kfps | Off line | ... |
| Fast CMOS | 66 | 2D | € € | Halogen 50W | 2 kfps | 0. 5 kHz | Centroid |
| FPGA | 67 | 2D | € € | Cold LED 15W and optical fiber | 10 kfps | 10 kHz | Hardware |
| Stereoscopy | 68 | 3D | € € | 2 × white LED 3W and optical fiber | 340 Hz | 340 Hz | Symmetry recognition |
| DVS | 69 | 2D | € € | Cold LED 5W | 3 kHz | 30 kHz | Spare matrix hough circle |

**Figure 2.6.** – **Overview of selected detection techniques.** Several laser- and photodiode based detection methods (interferometer, back focal plane, photodiode imaging) are compared to camera based schemes in terms of price, tracking performance, acquisition speed, and required data processing. Table adapted from [Pacoret and Régnier 2013].

be recorded in time-shared intervals [Guilford et al. 2004; Ruh et al. 2011]. The limitation of this combined optical trapping and detection method is that there is a direct trade-off between the number of traps and the detection's sampling rate. Furthermore, each particle can only be monitored during the duty time when the trapping laser is creating the respective trap.

### 2.2.3. Comparison of detection methods

In the literature, a number of publications can be found that provide guidance regarding the available detection methods for optical tweezers and discuss the respective advantages and limitations [Neuman and Block 2004; Keen et al. 2007; Gibson et al. 2008; Bowman and Padgett 2013; Pacoret and Régnier 2013]. The main categories for comparison are bandwidth, spatial resolution, cost, simplicity of implementation, illumination requirements, the number of spatial dimensions that can be tracked, and whether on-the-fly analysis is possible with currently available hardware (Fig. 2.6). Through the last decades, two detection methods have emerged to be prevalent: camera based tracking and back focal plane interferometry.

Back focal plane interferometry is typically used for single- or dual-beam optical tweezers, and has, quoting Moffitt et al., *"become the standard in the field owing to its sensitivity, linearity, and speed in all three dimensions"* [Moffitt

et al. 2008]. However, the method's incompatibility to monitor several particles in parallel has severely limited its application when multiple optical traps, like holographic optical tweezers, are used for particle manipulation.

Camera based detection is the prevalent technique for multiple trap optical tweezers. While the technique features higher cost and reduced spatiotemporal resolution, it excels with parallel tracking capability and being easy to implement for standard lateral displacement measurements. Going beyond standard two dimensional tracking, e.g., reaching tracking speeds at the millisecond scale in three dimensions, requires specialized camera or imaging schemes and is computationally demanding.

### 2.2.4. Trap calibration by power spectrum analysis

In force measurements, it is commonly assumed that the optical potential is approximately harmonic around the trap center. With this assumption, the restoring force $F_{trap}$ can then, for a small excursion from the bead's equilibrium position, be calculated by the Hookean equation

$$F_{trap} = -\kappa x, \tag{2.1}$$

where $x$ is the bead's time-dependent displacement from its equilibrium position, and $\kappa$ denotes the trap stiffness, i.e., the spring constant corresponding to the harmonic optical trapping potential in the x-direction. As a side note, it is important to be aware that this linear approximation breaks down for larger displacements on the order of half the particle's radius and above, resulting in a variable trap stiffness that depends on displacement and bead size [Richardson et al. 2008; Godazgar et al. 2011]. Force measurements require thus that the trap stiffness $\kappa$ is known and that the bead's position $x$ can be measured with high precision.

For optical trapping setups that employ back focal plane interferometry as position detection system, several different calibration protocols can be used to

deduce the trap stiffness $\kappa$. Most common are the hydrodynamic-drag method, the equipartition-theorem method, and the power-spectrum method [Perkins 2009]. The power spectrum analysis is discussed in more detail in the following paragraphs as this is the calibration method used in this project.

In essence, trap calibration by power spectrum analysis is based on comparing the experimental power spectrum of recorded position fluctuations of a trapped bead with the theoretically predicted power spectrum and deducing the trap and detector characteristics from this comparison. The focused optical trapping beam generates a harmonic optical potential well, in which the trapped bead fluctuates around its equilibrium position due to the interaction with the surrounding solvent, for biophysical studies typically water. The dynamics of this confined Brownian motion are well described by the Langevin equation

$$m\ddot{x}(t) + \gamma\dot{x}(t) + \kappa x(t) = F_{\text{therm}}(t), \tag{2.2}$$

where $m$ is the bead's mass, $\gamma$ the friction coefficient, and $F_{\text{therm}}(t)$ a random and time-dependent force. $F_{\text{therm}}(t)$ captures the thermal collisions with the solvent molecules, and the friction coefficient $\gamma$ is given, if far from any surfaces, by Stokes' law

$$\gamma = 3\pi\eta d, \tag{2.3}$$

with $d$ being the diameter of the particle and $\eta$ the viscosity. To a good approximation, the inertial term, $m\ddot{x}(t)$, can be neglected when the surrounding solvent is water, due to the low Reynolds number at this small length scale.

The time-dependent position $x$ of the bead can be measured using a quadrant photodiode in a back focal plane interferometry geometry, as introduced in Section 2.2.2. From the intensities $I_i$, $i = \{1, 2, 3, 4\}$, impinging on the four, clockwise labeled segments of the quadrant photodiode, the lateral displacements

can be deduced from the differential intensities

$$I_{\mathrm{x}} = (I_1 + I_2) - (I_3 + I_4), \tag{2.4}$$

$$I_{\mathrm{y}} = (I_1 + I_4) - (I_2 + I_3), \tag{2.5}$$

and the axial counterpart is related to the total intensity reaching the QPD

$$I_{\mathrm{z}} = I_1 + I_2 + I_3 + I_4. \tag{2.6}$$

Quadrant photodiodes do output voltage signals $S(t)$, requiring a conversion to metric units of distance before Equation 2.1 can be used. For small bead displacements, a regime exists where the voltage signals $S(t)$ are linearly proportional to the bead displacement $x(t)$ and conversion is simply achieved by means of a conversion factor $\beta$ according to

$$x(t) = \beta S(t). \tag{2.7}$$

Using power spectral analysis, the conversion factor $\beta$, the time-dependent bead position $x$, and the trap stiffness $\kappa$ can be determined from a single recorded time-series of the QPD voltage signals $S(t)$ of a trapped bead. To do this, the Langevin equation (Eq. 2.2) is recast into a power spectrum, describing the spatial trajectory of the bead instead in frequency space in terms of its frequency components. The power spectrum of the voltage signal $S(t)$ can be calculated as

$$P_{\mathrm{exp}}(f) = \left| \tilde{S}(f) \right|^2 / T, \tag{2.8}$$

where $T$ denotes finite measurement time and $\tilde{S}(f)$ the Fourier transform of the signal $S(t)$

$$\tilde{S}(f) = \int_{-T/2}^{T/2} S(t) e^{i 2\pi f t} dt. \tag{2.9}$$

Employing Equation 2.7, this experimental power spectrum can be rewritten as

$$P_{\text{exp}}(f) = \left|\tilde{S}(f)\right|^2 / T = \frac{1}{\beta^2}\left|\tilde{x}(f)\right|^2 / T. \tag{2.10}$$

The experimentally measured power spectra vary in consecutive measurements due to the stochastic force $F_{\text{therm}}(t)$. On the other hand, the theoretical power spectrum of the Langevin equation, $P_{theo}(f)$, can be calculated as the expectation value of power spectra obtained from experimental data

$$P_{theo}(f) = \langle P_{\text{exp}}(f)\rangle = \frac{A}{f_{\text{c}}^2 + f^2}, \tag{2.11}$$

with $f_{\text{c}}$ being the so-called corner frequency

$$f_{\text{c}} = \kappa/2\pi\gamma \tag{2.12}$$

and the constant

$$A = \frac{D}{2\pi^2\beta^2}, \tag{2.13}$$

where $D$ is the bead's diffusion constant. $D$ and $\gamma$ are connected by the Einstein equation

$$D = \frac{k_{\text{B}}\text{T}_{\text{temp}}}{\gamma}, \tag{2.14}$$

where $k_{\text{B}}$ is the Boltzmann constant and $\text{T}_{\text{temp}}$ the absolute temperature. For simplicity the equations are stated for one spatial dimension, but can be extended to three dimensions in an analog fashion.

Next, by comparing the experimentally measured power spectrum with the theoretically predicted power spectrum, using both $A$ and $f_{\text{c}}$ as fitting parameters in a Lorentzian fit, the conversion factor $\beta$ and the corner frequency $f_{\text{c}}$ can be determined. In practice, it is important to account for effects related to the measurement conditions and the experimental implementation that alter the recorded voltage signal. Especially, aliasing, existing signal processing filters in
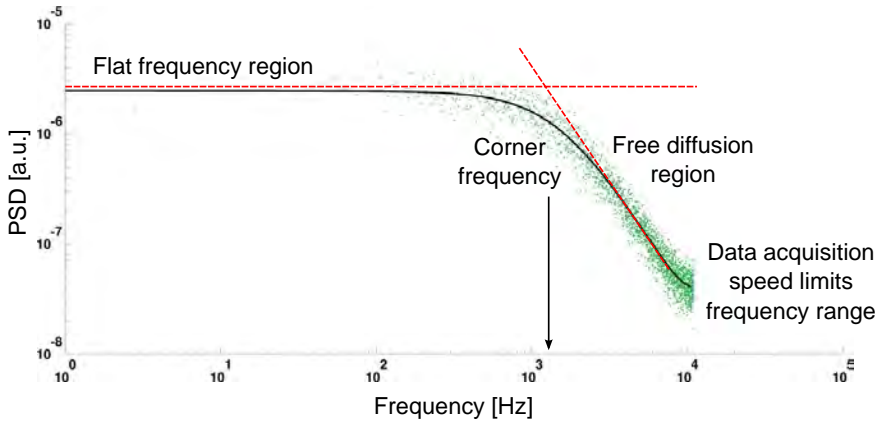
**Figure 2.7.** – **Typical power spectrum of an optically trapped bead.**
The power spectral density (PSD) describes the bead movement in terms of the
contained frequencies. Both the experimental data points (green dots) and the
corresponding Lorentzian fit (black line) are shown. Two different regions can be
identified. The high frequencies correspond to fast free diffusion in the optical
trap. While at low frequencies the bead movement is dominated by the optical
forces of the optical trap leading to a flat frequency dependency. The trap stiff-
ness determines at which frequencies the transition from restricted to diffusive
dependency takes place.

the amplifiers, surfaces in the vicinity to the optical trap, a photodiode specific
filtering effect, and optimal measurement duration for noise reduction have to
be named in this regard [Berg-Sørensen et al. 2003; Berg-Sørensen and Flyvb-
jerg 2004; Andersson et al. 2011]. Specialized, freely available software packages
have been developed that take these and other minor effects, e.g., a frequency
dependency of the friction coefficient, into account when calculating $f_c$ and $\beta$
[Tolić-Nørrelykke et al. 2004; Hansen et al. 2006].

A typical experimental power spectrum and the fitted theoretical power spec-
trum is shown in Figure 2.7. By means of Equation 2.12, the extracted corner
frequency $f_c$ can be converted into the trap stiffness at this specific laser in-
tensity. Now, both the conversion factor $\beta$ and the trap stiffness $\kappa$ are known,
which enables the calculation of the exerted optical force.

## 2.3. Experimental setups

All experiments were conducted on an optical setup that I built around an inverted Leica DM IRBE microscope, which was modified to accommodate either dual-beam optical tweezers or, alternatively, holographic optical traps. In this section, I describe the optical layouts of these setups and present the underlying design considerations. For reference, a tabulated list of the electrical and optical components can be found in the Appendix A.0.1.

### 2.3.1. Dual-beam optical tweezers generation

In the dual-beam optical tweezers implementation, shown in Figure 2.8, the two traps were generated from the same laser source, a near-infrared, 1064nm, continuous-wave laser, using beam-splitting optics. Compared to the possibility of using two separate lasers, this is often preferred since the single source guarantees that potential Poynting vector and power fluctuations influence both traps similarly, besides also having the obvious advantage of reduced cost. The laser output beam had a near Gaussian profile ($M^2 < 1.1$) and was expanded to a larger diameter, a size overfilling the back aperture of the microscope objective. The linear polarization of this Gaussian beam could be rotated by means of a half-wave plate. A subsequent polarizing beam-splitter generated two separate beams in perpendicular polarization states with variable power splitting depending on the orientation of the half-wave plate. The half-wave plate was adjusted such that the two beams had a 50:50-power ratio (Fig. 2.9). Next, relevant for beam steering purposes, both beams passed through combinations of two lenses forming 1:1-telescopes. After re-merging the beam paths using a second polarizing beam-splitter, the collimated beams were co-axially send into the back port of an inverted microscope, coupled into the microscope's beam path by a dichroic mirror, and focused by a high-NA water immersion microscope objective, thus creating two optical traps in the microscope's focal plane.
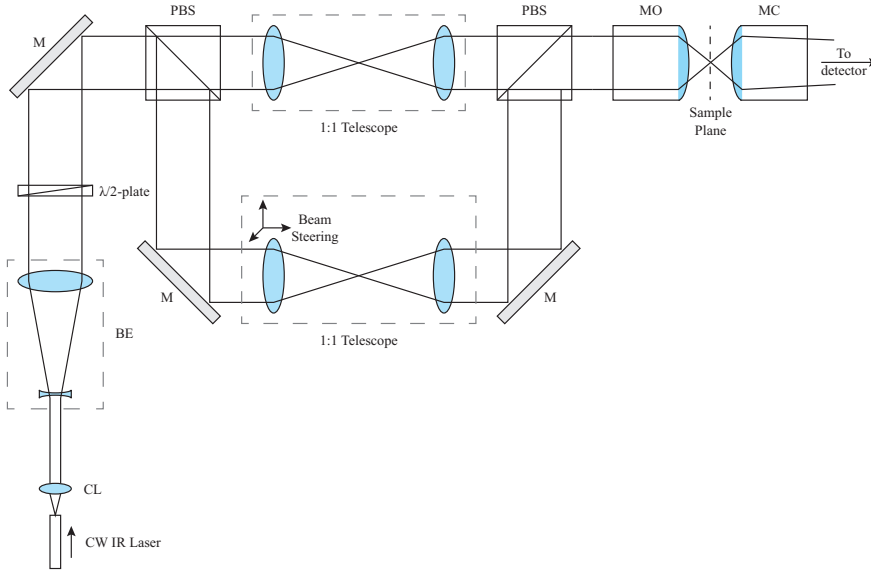
**Figure 2.8.** – **Schematic drawing of optical layout for dual-beam trap generation.** The output beam of a continuous-wave, diode-pumped solid-state (cw DPSS) laser was collimated by a collimating lens (CL) and expanded using a beam expander (BE). A half-wave plate in combination with a polarizing beam-splitter (PBS) allowed for power-control. Beam-steering capabilities were added by means of two 1:1-telescopes, where the piezo-actuated displacement of the first telescope lens allowed the 3D positioning of the optical traps in the sample volume. The microscope objective (MO) featured a high NA to provide strong focusing of the trapping beams. Light collection for subsequent position and force detection was done using a large NA microscope condenser (MC). Mirrors are marked with an M.
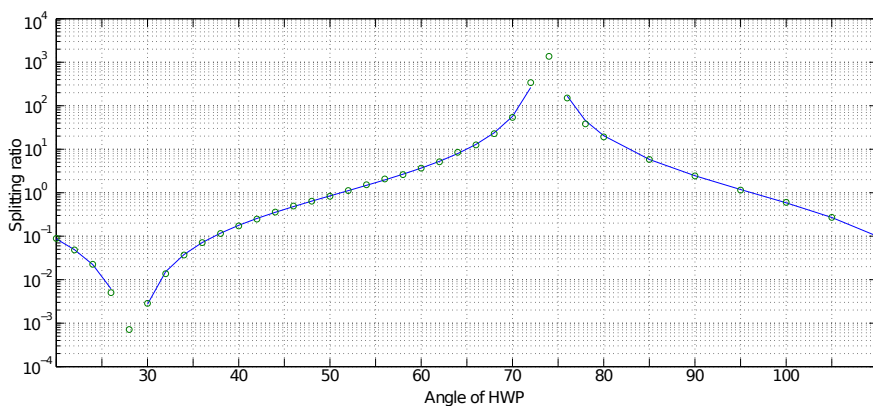
**Figure 2.9.** – **Dependency of the power splitting ratio on half-wave plate adjustment.** The splitting ratio, i.e., the power of the static trap relative to the movable trap, could be adjusted by rotation of the half-wave plate (HWP). Data points from the calibration are shown as green circles and are fitted with the dependency predicted by theory (blue line).

The objective collar was adjusted to compensate for spherical aberrations and optimize the foci for optical trapping [Reihani et al. 2011].

The first optical trap was aligned such that it was located in the center of the field of view in the sample plane. This trap will be referred to as the **static trap** or, for simplicity, **Trap 1**. For the second trap, dynamic control of the trap position was added and it is here referred to as the **movable trap**, or **Trap 2**. The beam steering of Trap 2 was achieved by mechanical, piezo-actuated translation of the first lens of the 1:1-telescope. This 'beam steering lens' was placed in a plane that was optically conjugated to the back focal plane of the microscope objective by means of the second telescope lens [Neuman and Block 2004]. In this arrangement, a lateral displacement perpendicular to the optical axis causes a tilt in the beam propagation direction, thus entering the microscope objective in an angle to the optical axis and resulting in a lateral displacement of the focal spot, i.e., the optical trap. Similarly, an axial displacement of the 'beam steering lens', parallel to the beam propagation axis, changes the divergence of the beam that enters the microscope objective and allows for control of the axial

position of the optical trap.

The power that the trapping laser delivered to the focal plane can be estimated by measuring the power that enters the entrance aperture of the microscope objective and accounting for the pronounced optical absorption of the objective in the infrared. For this measurement, I replaced the objective with an annular aperture that matched the objective's entrance aperture. Based on the assumption of an optical transmission of 60% for 1064nm (according to Leica's customer support), the power in the focal plane could be estimated from this measurement (Fig. 2.10).
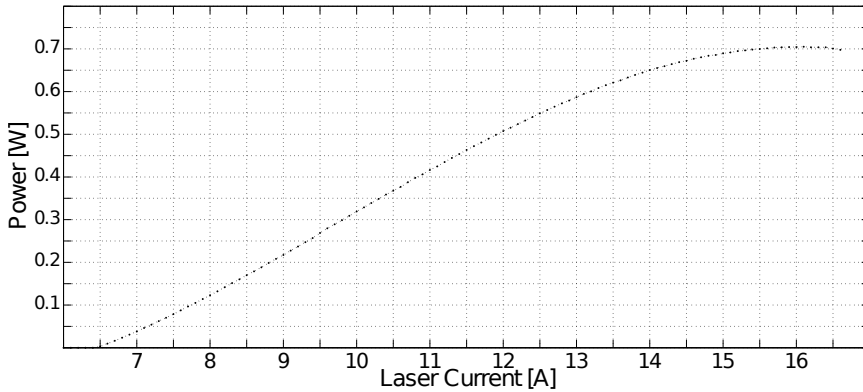


**Figure 2.10.** – **Conversion of laser diode current to laser power in the focal plane.** The plot shows the relation between current driving the diode-pumped solid-state laser and the power reaching the focal plane. Beam cutting by the microscope's entrance aperture and the low transmission coefficient for 1064 nm (60%) were taken into account in the measurement.

The beam steering layout aims at guaranteeing a constant trap stiffness at different positions in the field of view by ensuring that the transmitted power is independent of the angle of incidence into the microscope objective. However, a displacement of the trap is often still accompanied by a slight power loss [Fällman et al. 2006]. In this setup, this effect can mainly be attributed to the fact that the back focal plane of the objective does not coincide with the objective shoulder, but is actually located 17.50mm *inside* the microscope objective (correspondence with Leica's customer support), leading to a marginal clipping
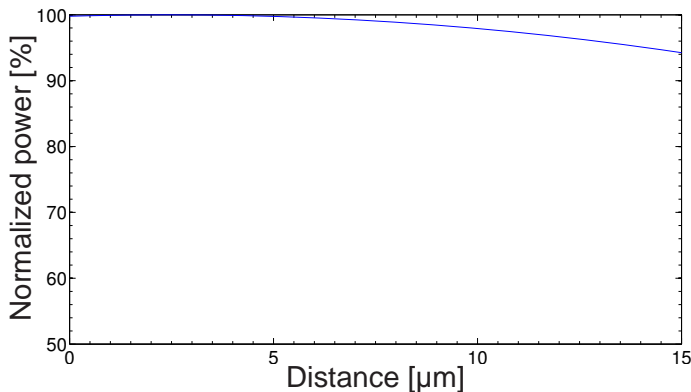
**Figure 2.11.** – **Decrease of laser power for off-centered optical trapping.**
The graph shows the position-dependent transmitted power of the movable trap,
Trap 2, which decreases with increasing distance from the center of the field of
view. For reference, the signal was normalized by the power of the static trap,
Trap 1, in the center of the field of view.

of the tilted trapping beam for off-center traps. For the positions close to the
center of the field of view, this effect is negligible. However, the power decrease
becomes more pronounced for offset positions, approaching 5% for positions far
from the center, and should thus be taken into account (Fig. 2.11).

For trapping experiments, perfusion chambers with a thickness of approxi-
mately $80\mu m$ were built by sandwiching two #1.5 cover slips on top of each other,
separated by double-sided sticky tape. These sample chambers were loaded with
a suspension of $0.96\mu m$ polystyrene beads (PS03N/9396, Bangs Laboratories)
diluted in Millipore water and sealed using vacuum grease.

## 2.3.2. Holographic optical trap generation

For holographic optical trapping experiments, the optical setup was modified in
the following way.

All laser power was directed to the static beam path (compare Fig. 2.8).
Phase modulation in the back focal plane of the microscope objective, or in a
conjugate plane to it, can be used to generate desired intensity distributions

in the objective's focal plane [Dufresne and Grier 1998]. In our setup, a phase-modulating diffractive optical element (DOE) was positioned such that it was imaged by the second telescope lens onto the back focal plane of the objective. To demonstrate the detection technique for holographic optical traps, a generic DOE was chosen imprinting a phase profile into the originally flat wavefront of the Gaussian laser that corresponded to a hexagonal arrangement of 7 traps, i.e., one central trap surrounded by a hexagon of 6 traps (Fig. 2.12).

### 2.3.3. Implementation of spatial filtering detection method

In back focal plane interferometry, a lens is used to image the interference pattern in the back focal plane of the condenser onto the quadrant photodiode [Gittes and Schmidt 1998]. In the case of multiple optical tweezers, the several scattered and unscattered signals of the individual traps overlap and interfere in the back focal plane of the condenser as this is a Fourier plane to the sample plane. Essentially, it is this signal mixing, and the corresponding complexity of disentangling these signals, that limits the use of photodiode detection for multiple traps. The beams of the optical traps overlap almost everywhere along the optical path, however, due to said relay imaging, an intermediate plane exists where all beams are spatially well separated. In this plane, it possible to isolate signals from individual traps by spatial filtering, as illustrated in Figure 2.12. This plane is located between the relay lens and the quadrant photodiode, and it is simply an image plane of the sample plane where the optical trapping is taking place; meaning that, beside blurring according to the point spread function of the imaging system in between, the same intensity distribution as in the sample plane is recreated. To implement signal selection by spatial filtering, a simple pinhole was added in this plane, representing the only modification to standard back focal plane interferometry, and positioned such that only light originating from one trap of interest was transmitted through the pinhole. The beams from
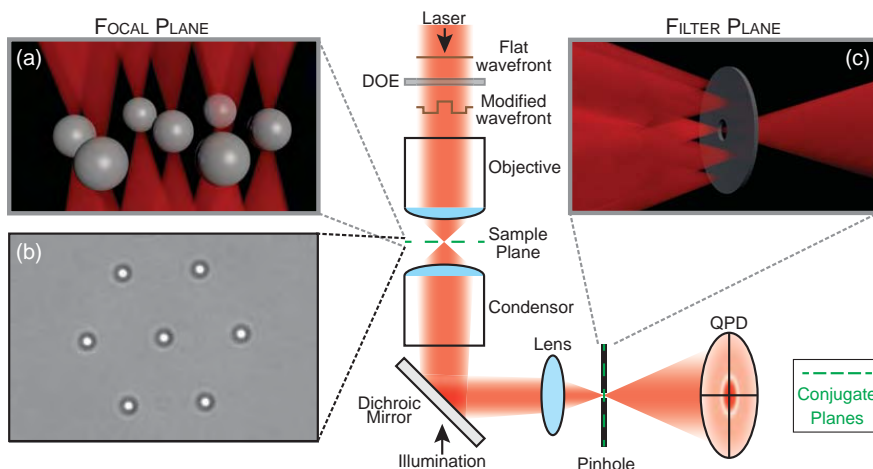
**Figure 2.12.** – **Optical layout and illustration of the spatial filtering method for the detection of multiple optical traps.** Modification of the initially flat wavefront by a diffractive optical element (DOE) was used to generate 7 optical tweezers in the focal plane of the objective (a: Visualization of trapping plane, b: Bright field image captured by camera). The imaging of the back focal plane of the condenser onto a quadrant photodiode (QPD) allows accessing an intermediate image plane of the trapping plane that can be used for spatial filtering and selection of one single trap for transmission (c: Visualization of filter plane) and subsequent photodiode based detection.

the other remaining traps were blocked and discarded by the opaque regions of the pinhole filter. The concept is similar to the idea that is at the core of confocal microscopy. A pinhole is used here to selectively collect light from a restricted volume of the sample plane and reject light from the surrounding area.

### Alignment of the pinhole

Beside the choice of the relay lens, the distance of the condenser from the sample plane has an influence on the magnification and the position of the image plane where the spatial filtering is performed. Due to the adjustable condenser position of the commercial microscope, it was necessary to reposition the condenser and realign the pinhole after exchanging sample slides. Alignment according to Köhler illumination was adopted as this offered a reliable reference, guarantee-

ing reproducible positioning of the optics, and good contrast for the bright field imaging by a video camera via the camera port. Pinholes of different sizes could be mounted and fine-positioned by means of a three-axis micropositioning stage equipped with differential drives.

Alignment of the pinhole to one specific trap of interest took approximately 5 minutes and was done using the following procedure. The summed signal from all 4 photodiode quadrants was used as a read-out of the transmitted intensity through the pinhole. Precise alignment could be achieved by moving the pinhole in a scanning fashion, adjusting the position until the transmitted intensity was maximized. This guarantees co-localization with one arbitrary trap. For multiple traps, one has to figure out with which trap the pinhole is aligned. This can be easily done by monitoring the transmitted intensity while scanning the pinhole in the filter plane, providing a two dimensional 'map' of the intensity distribution in this plane. Subsequently, the correct alignment can be verified by confirming that a Lorentzian power spectrum only appears when a bead occupies this specific trap to which the pinhole is aligned.

**Extended optical setup for multiple particle tracking**

The approach for tracking multiple particles in parallel is simple: for each additional optical trap that should be detected, a separate detection module, consisting of a pinhole and a QPD, is added. We demonstrated multiple bead tracking for three optical traps simultaneously, as this would not be possible using polarization based tracking. The further adaption to a higher number of detectable traps from here is straight-forward. For this demonstration, the detection part of the setup was extended, as shown in Figure 2.13. In practice, it has advantages to use a relay lens with a larger focal lens ($7.5cm$), as this provides a longer optical path and more space for positioning the additional optical elements. Two non-polarizing beam-splitters were inserted behind the relay lens, splitting the beam coming from the condenser into three 'daughter' beams, i.e., identical
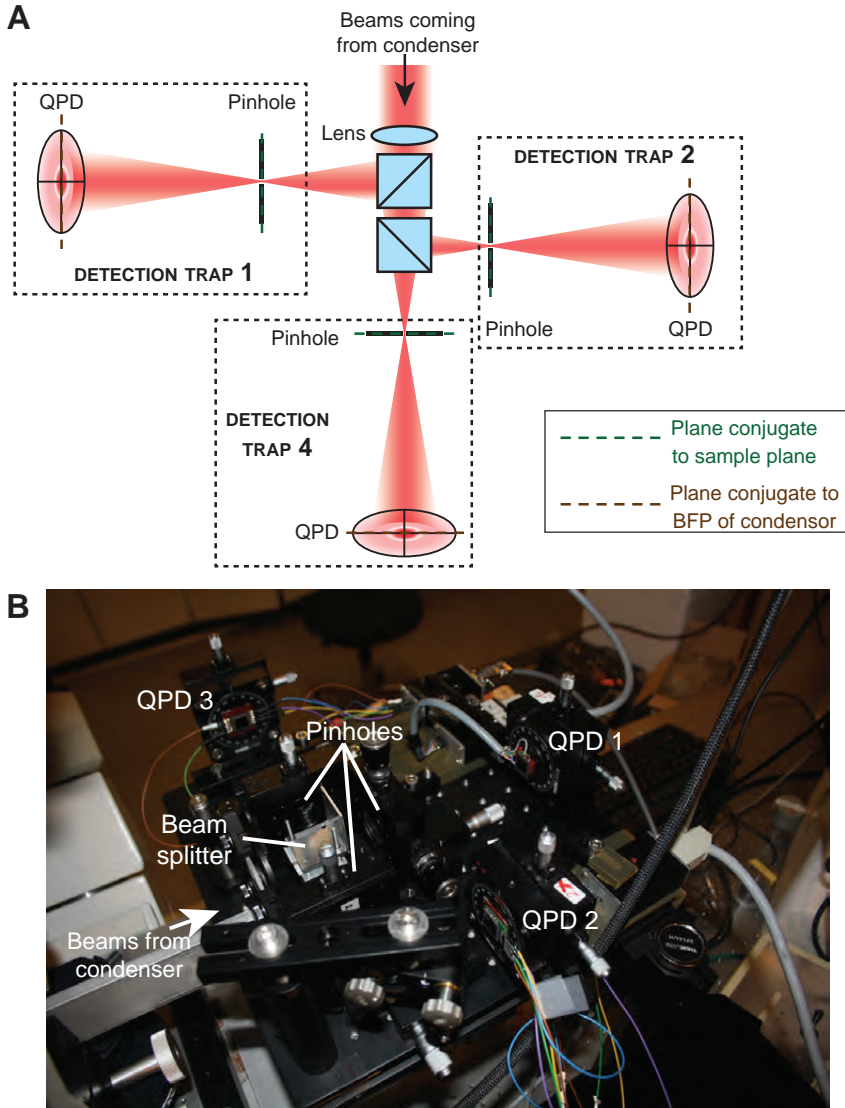
**Figure 2.13.** – **Modified setup for simultaneous tracking of multiple beads.** (a) The beam from the condenser containing the overlapping signals of all traps is duplicated using non-polarizing beam-splitters. To detect additional traps, 'detection modules', i.e., a pinhole and a QPD, are added to the optical layout. (b) Image of the detection stage. The beam enters the detection setup from the left. The three pinholes and QPDs are marked.

replicates of the beam. Next, one pinhole and one QPD were added to each of the three optical paths. Micropositioners allowed the alignment of the pinholes, respectively positioned in planes conjugate to the sample plane, with different optical traps of interest. The planes in which an image of the back focal plane of the condenser was formed were located by imaging the nearly closed condenser aperture onto the chip of a video camera, that was subsequently replaced by the QPDs.

**Data acquisition**

Digitalization of the analog QPD signals was done in the following way. As the first step, a pre-amplifier, connected to the photodiodes by shielded short cables, amplified the raw voltage signals of the individual quadrants. The total and differential signals, corresponding to the lateral and axial position traces, were calculated in an integrated electronic circuit. Next, these three analog signals were send to a second low-noise amplifier, where the signal levels were adjusted to the available voltage range of a PC-coupled National Instruments analog-to-digital converter (ADC). Care was taken to adjust the signal levels to span the full input voltage range such that binning effects are minimized. Custom-written Labview programs were used to trigger recordings of time series of these signals. The settings for these were multiple 3 second captures with a sampling rate of 22 kHz.

# 3. Evaluation of the proposed detection method

This chapter deals with the experimental demonstration of the proposed detection method and the evaluation of its efficiency. First, initial proof of principle experiments are reported that confirmed the feasibility of the detection method. This is followed by results from experiments and simulations aiming at quantifying the efficiency of the signal separation by spatial filtering.

## 3.1. Proof of principle – Calibration of a single optical trap

The first step to test the proposed detection method was to do a complete characterization of a single-beam optical trap in a setup that had a pinhole added to the standard back focal plane interferometric detection. One characteristic hallmark of back focal plane interferometry, as explained in Chapter 2.2.2, is the linear relation between the bead position and the QPD voltage signals for small displacements from the trap center. This can be validated by monitoring the QPD signals while scanning a bead that is immobilized on the glass surface of the sample chamber through the focus of the trapping beam. This way the respective QPD readings are known for all bead positions in the optical trap and the QPD signals can be correlated with real positions in metric units of meters. Notably, the linear regime is not a necessity for photodiode based detection,

it is mainly convenient as it facilitates easy conversion from voltage signals to displacements via a constant conversion factor. Bead scanning experiments of this type were conducted with $0.96\mu$m polystyrene beads and confirmed a linear range for the axial and the lateral QPD signals. A typical one-dimensional scan can be seen in Figure 3.1 a. An important aspect is that the signals and displacements in directions perpendicular to each other are not coupled – in other words, a displacement of the bead along the y-axis should only results in a change in the y-channel of the QPD and not in the x-channel. Indeed, two-dimensional conversion factor maps, as shown in Figure 3.1 b, confirmed that small variations in x had only very minor influence on the conversion factor in y-direction, as can be seen from the constant slope in the y-direction for the region around the equilibrium position.

Next, to ensure that the spatial filter did not influence the measured trap stiffness, the results from trap calibrations with and without the pinhole installed were compared. After aligning the pinhole to the optical trap, a time-series of the movement of a trapped bead was recorded. Subsequently, the pinhole was removed and a second time-series was captured. The respective corner frequencies were calculated using power spectral analysis, as introduced in Section 2.2.4. The power spectra of the time-series were fitted well with the expected Lorentzian shape predicted by theory, and the estimated corner frequencies agreed within their standard deviation, indicating that the presence of the pinhole does not have a measurable influence on the measured trap stiffness (Fig. 3.1 c).

One challenge that became obvious during these proof-of-principle measurements was the importance of a mechanically rigid positioning of the spatial filter. Long-term measurements, with data collected once every minute for 1.5 hours, showed that the measured corner frequencies remained unchanged, pointing at that pinhole drift was not an issue on this time scale. However, mechanical vibrations, causing small changes in the position of the pinhole, coupled clearly to the QPD signals and were visible at the lower frequencies in the power spec-
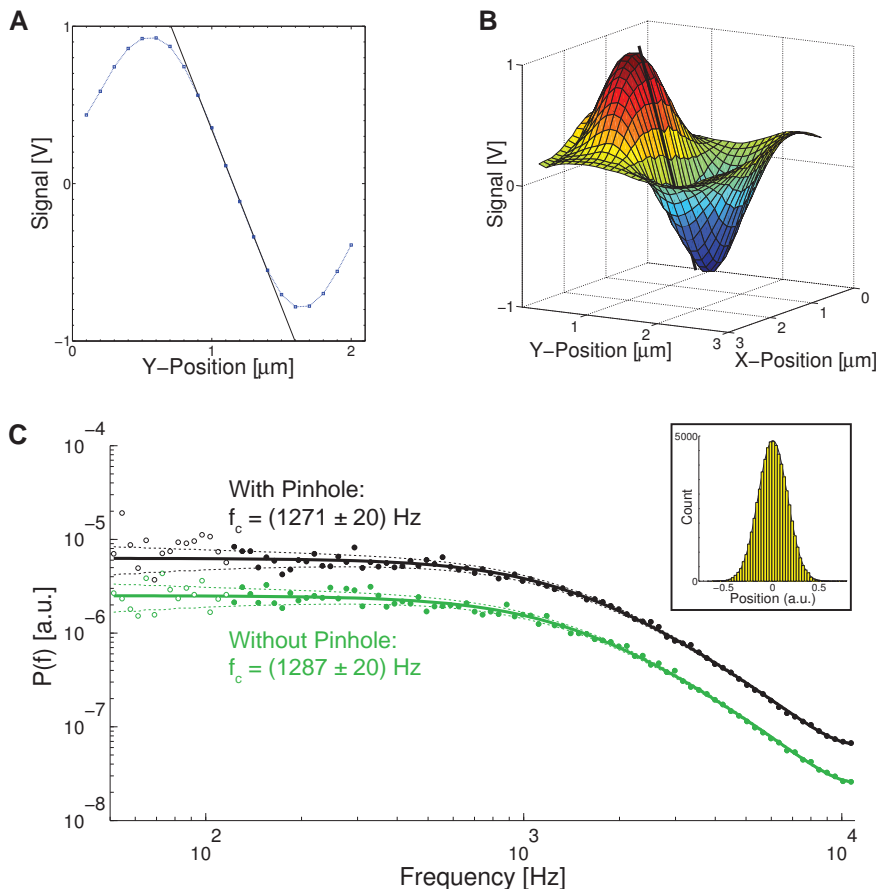
**Figure 3.1.** – **Proof-of-principle calibration of single-beam optical tweezers.** (a) Conversion from QPD signal to bead position. The graph shows the raw voltage signal of the QPD y-channel (blue dots) when scanning of an immobilized bead along the y-direction. The black line marks the linear region with a constant conversion factor. (b) Surface plot of the QPD y-signal for a two-dimensional scanning of a bead in the focal plane. The cross-section along the black line corresponds to the plot in (a). The y-signal shows only a minor dependence on x-displacements, notable by the constant slope in the y-direction in the vicinity to the equilibrium position. (c) Comparison of power spectra acquired with and without spatial filter installed. As the plots overlap very closely, a vertical offset was added to increase visibility. Solid lines are Lorentzian fits to the data, dotted lines show the ±1 standard deviation expected from theory, filled dots mark data included in the fit, open circles indicate data outside the fitting range. Inset: Gaussian fit to position histogram of time-series that was captured with the pinhole installed.

trum. This was especially pronounced for smaller pinholes. To some extend this problem could be circumvented by using a larger image magnification from the sample plane to the filter plane, which would allow for the use of larger pinholes. To reduce the influence of these mechanical vibrations on the estimated corner frequency, the fitting range for the Lorentzian function was adjusted to exclude the low frequency regime below 120 Hz.

## 3.2. Quantification of signal separation efficiency

With the aim to detect multiple traps in parallel, it was important to investigate to which extent additional traps would influence each others tracking signals. The quantity

$$\Psi = \frac{S_{\text{parasitic}}}{S_{\text{total}}} , \qquad (3.1)$$

called crosstalk, can be used as a measure for the amount of signal deterioration. Put in words, crosstalk quantifies the amount of undesirable, 'parasitic' signal $S_{\text{parasitic}}$, originating from the adjacent traps, relative to the QPD signal $S_{\text{total}}$ of one single trap of interest that one would like to record exclusively in a measurement.

The steerable dual-beam optical tweezers setup, introduced in Chapter 2.3.1, was used for these experiments, as it allowed for well controlled crosstalk measurements with variable distance between the two traps. As the signal separation builds on spatial filtering in an image plane, it is expected that the magnitude of the crosstalk will be dependent on the inter-trap distance $d$ and the pinhole size $p$ (Fig. 3.2). This influence of the inter-trap distance $d$ on crosstalk was investigated in a series of experiments, where also the pinhole diameter $p$ was changed.
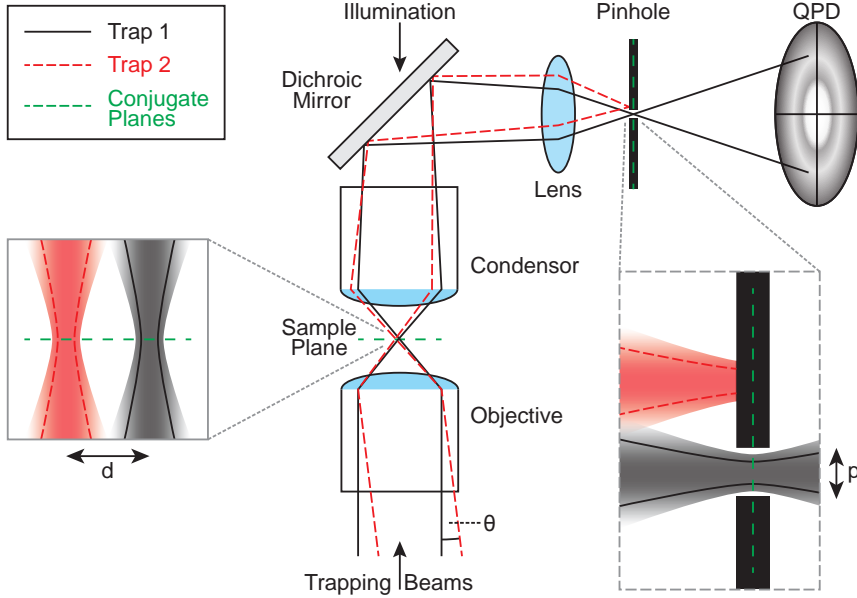
**Figure 3.2.** – **Setup for estimating the amount of parasitic signal from an adjacent trap.** The influence of an additional trap can be quantified by measuring the parasitic signal $S_{\text{parasitic}}$ originating from Trap 2 (drawn in red) that would penetrate the pinhole that is aligned for the detection of Trap 1 (drawn in black). The position of Trap 2, and thus the distance $d$ separating the two traps, can be adjusted by varying the angle of incidence $\theta$ into the objective. How much the additional trap interferes with the measurement of Trap 1 is also determined by the pinhole size $p$.

**Experimental protocol and data analysis**

First, the pinhole was aligned with the static trap (Trap 1) in the center of the field of view, representing our 'trap of interest' of which the tracking signal should be measured with as much purity as possible. The movable trap (Trap 2) was positioned in the same focal plane, overlapping with Trap 1, and could be switched on to cause a 'parasitic' signal. Doubling of the transmitted signal, when Trap 2 was active, confirmed that the location of Trap 1 and Trap 2 coincided. Next, to record the distance dependent crosstalk, the inter-trap distance $d$ between the two trap foci was continuously increased, moving Trap 2 laterally away from Trap 1, while recording the transmitted light intensities, $S_{\text{parasitic}}$ and $S_{\text{total}}$ (Fig. 3.3). Here, the integral signal from the QPD, i.e., the z-channel, served as the intensity read-out. The detector beam path was covered by an opaque hood to block ambient light, that would otherwise result in artifacts for low signal levels. The signal $S_{\text{parasitic}}$ could be measured as the intensity that was transmitted through the pinhole when Trap 1 was off and only Trap 2 was switched on. Likewise, $S_{\text{total}}$ was measured as the total intensity that penetrated the pinhole for the situation when both Trap 1 and Trap 2 were active.

Two error sources stemming from the instrumentation were compensated for prior to further data analysis. Firstly, the QPD dark current was subtracted from the measured signals. This was done by recording a time-series (3 seconds at 22kHz) with all beams switched off, before each measurement, providing the mean QPD dark current for the chosen amplification level. Secondly, it was compensated for the power loss in the trapping beam for off-center locations of Trap 2. As explained earlier in Section 2.3.1, this is caused by beam clipping at the objective entrance aperture that depends on the beam's angle of incidence. Power compensation was achieved by multiplying the measured signals with a position-dependent correction factor defined by the calibration curve that was shown in Figure 2.11. Disregarding this effect would otherwise result in an underestimation of the parasitic signal from Trap 2 for far off-center positions.
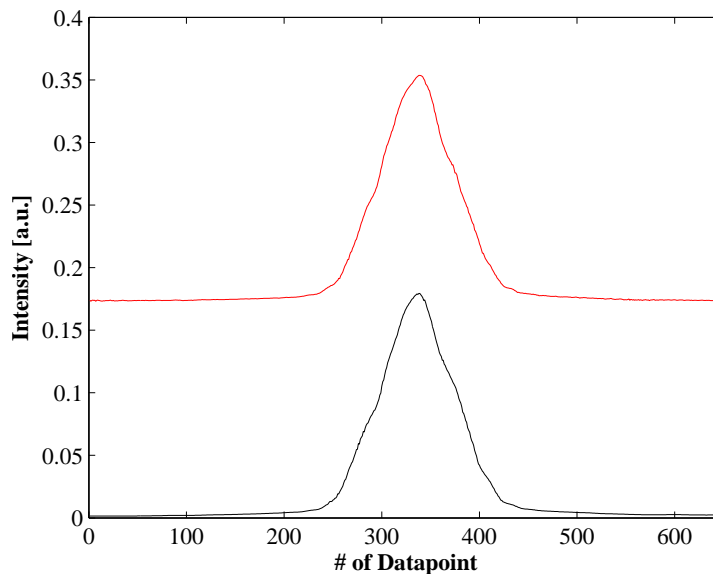
**Figure 3.3.** – **Typical raw data captured while sweeping Trap 2 over the field of view.**. $S_{\text{parasitic}}$ can be recorded when only Trap 2, i.e., the source of the parasitic signal, is switched on. To record $S_{\text{total}}$ both Trap 2 and Trap 1, i.e., the 'trap of interest', are switched on. $S_{\text{parasitic}}$ is shown in black and $S_{\text{total}}$ in red. In this example, a $50\mu$m pinhole was used and the peak transmissions are reached when Trap 2 is aligned with Trap 1 and the pinhole center, approximately at data point number 330.

**Dependency on pinhole size and inter-trap distance**

A range of pinholes sizes were evaluated in the above described way. The results of the experiments are collected in Figure 3.4, showing the dependency of the crosstalk levels on the inter-trap distance $d$ for the pinhole sizes $p = 10\mu$m, $20\mu$m, $50\mu$m, $100\mu$m, and $150\mu$m.

The results confirmed that the crosstalk $\Psi$ decreases with increasing inter-trap distance $d$. In the initial condition, for exactly overlapping trapping beams, the parasitic signal of Trap 2 amounts to half of the detected total signal. With increasing trap separation, the crosstalk $\Psi$ declined, eventually approaching zero, as suppression of the parasitic signal by the spatial filter becomes more pronounced. For smaller pinhole sizes, the decline occurred earlier, i.e., efficient suppression of the parasitic signal occurred already at shorter distances. Notably, however, the pinholes cannot be chosen arbitrarily small due to the finite spot size. For pinholes with diameters $p \leq 10\mu$m, an oscillatory behavior of $\Psi(d)$, resembling a diffraction pattern, was apparent. It is well known that focal spots features also concentric rings with low intensity apart from the central high intensity spot. Aberrations in the imaging system contribute to the intensity of these areas outside of the central focus. Hence, we presume that the oscillating $\Psi$ values are explained by the 'point-like' intensity read-out, that these very small pinholes provide.

The different efficiencies of the pinholes to block the parasitic signal can be compared by plotting the distances at which the crosstalk had fallen by 3dB, $\Gamma(d)$. Note that a 3dB decrease is synonymous with a decrease of $\Psi$ to roughly 50% of its maximum value at $d = 0$ (marked with black circles in Figure 3.4 a). This revealed a linear relation between $\Gamma$ and the pinhole diameter $p$ (Fig. 3.4 b). For diameters smaller than $20\mu$m, where oscillations of $\Psi$ were observed, the linear relation stopped to be valid. For pinholes larger than this lower limit, the linear relation can be used to estimate the level of the crosstalk for a specific distribution of optical traps in the focal plane.
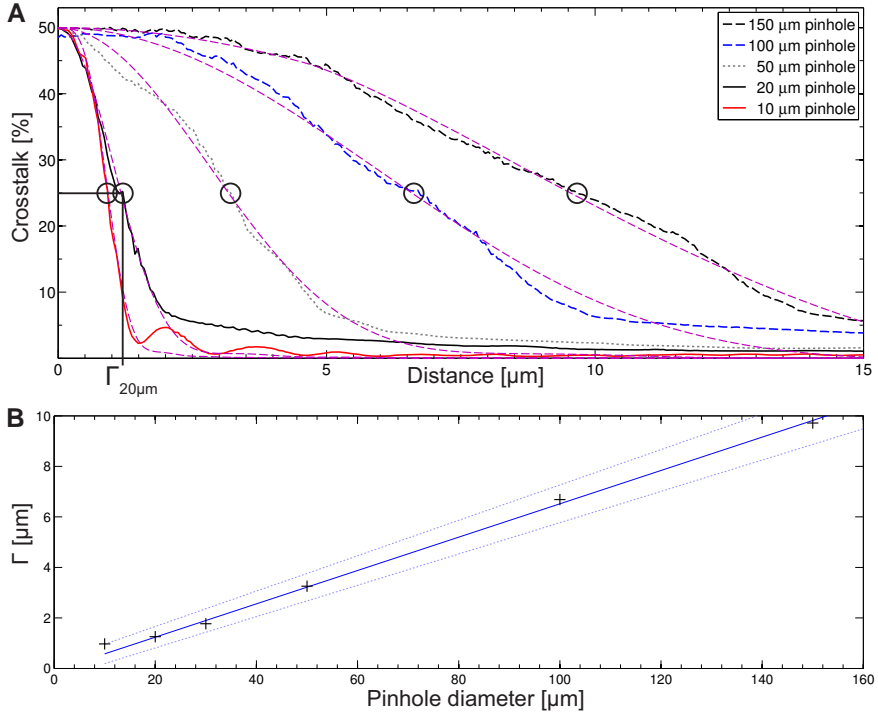
**Figure 3.4.** – **Efficiency of signal separation by spatial filtering.** (a) The crosstalk $\Psi$ is plotted against the inter-trap distance $d$ for the investigated pinhole sizes. All curves are shown without applying any kind of smoothing filter. Theoretical fits to the experimental data are drawn in dashed purple lines. For each pinhole size, the -3dB decrease distance, $\Gamma$, is marked by a black ring, and explicitly indicated for the $20\mu$m pinhole. (b) The -3dB decrease distances, $\Gamma$, are plotted as a function of pinhole diameter. The data points from $p = 20\mu$m to $150\mu$m are well fit with linear function (full line). The data point of the $10\mu$m pinhole lies just outside the 95%-confidence area of the fit, indicating that for this small pinhole the linear relation breaks down.

### 3.2.1. Simulation of crosstalk suppression

To back the experimental results, I wrote simulations to predict the crosstalk suppression by spatial filtering. The simulations are based on equations from wave optics, applied to a simplified optical system. The simplification consisted of treating the compound lenses in the optical system, i.e., the microscope objective and the condenser, as simple singlet lenses. In the experiments, the initially Gaussian beam was expanded and overfilled the aperture of the objective lens. The ratio of the beam waist and the entrance aperture of the objective is called the filling factor. This filling factor has an influence on the appearance of the focal spot in the sample plane. An approximately Gaussian-shaped focal spot with low intensity side lobes is present when the beam waist matches the aperture diameter. In the case of more pronounced overfilling, the intensity profile of the beam that enters the objective starts to become increasingly uniform with a flat intensity profile. The intensity distribution in the focal plane then starts to resemble an Airy disk, with more pronounced side lobes, as this is the Fraunhofer interference pattern generated by a plane wave at a circular aperture [Mahajan 1986]. Next, the condenser creates a magnified image of sample plane in the filter plane. To know exactly how this imaged focal spot looks like, it would be necessary to know the optical transfer function that mathematically describes this transformation. However, to a good first approximation, it should be possible to describe this focal spot with the function of an Airy disk

$$\mathcal{I}(r) = \mathcal{I}_0 \left( \frac{2\,J_1(x)}{x} \right)^2, \tag{3.2}$$

with the peak intensity $\mathcal{I}_0$ and $J_1(x)$ denoting the Bessel function of the first kind of order one, where $x$ contains both geometrical and optical parameters, i.e., $x = (2\pi/\lambda)ar$, with $a$ being the radius of the circular condenser aperture, $\lambda$ the wavelength, and $r$ the radial distance from the optical axis of the imaging system [Born and Wolf 1999].

With these simplifications, the distance dependent crosstalk can be readily calculated by computing

$$\Psi_{\text{theory}} = \mathcal{I}(r) \star g(r), \tag{3.3}$$

i.e, the 2D-convolution of the diffraction pattern $\mathcal{I}(r)$ and a two-dimensional circular boxcar function $g(r)$ defined as

$$f(x) = \begin{cases} g(r) = 1, & \text{if } r < p/2 \\ g(r) = 0, & \text{otherwise} \end{cases}$$

representing the binary spatial filtering by the pinhole.

Fitting this model to the experimentally measured curves showed that the distance dependency of the crosstalk can be well described with this simplified system (purple dashed lines in Fig. 3.4 a). Especially the initial decrease is well captured. For larger distances, however, the model clearly underestimates the crosstalk. Presumably this can be accounted to the fact that optical aberrations, which deteriorate the focal spot, are not included in this simple model. Pronounced side lobes would result in more pronounced tails of the crosstalk curves, as visible in the experimental data.

# 4. Detection of dual-beam optical tweezers with crosstalk suppression

In this chapter, I present the first application example, i.e., crosstalk elimination for experiments that use dual-beam optical tweezers. The origin of crosstalk and existing approaches to mitigate the issue are briefly reviewed. Thereafter, results from an improved setup that combines standard polarization based filtering and spatial filtering are reported.

## 4.1. Crosstalk in dual-beam optical tweezers

Dual-beam optical tweezers have been extremely successful in biophysical research. The ground-breaking investigations that have been possible thanks to this tool have deepened our understanding of the molecular world, e.g., regarding the functioning of molecular motors [Finer et al. 1994; Zhou et al. 2013], DNA-protein interaction[Sung et al. 2010], and the mechanical properties of DNA [Gross et al. 2011; Heller et al. 2013]. These intricate investigations require that the captured data is as accurate as possible, i.e., free of systematic errors. An error source that has often been overlooked is crosstalk in the detection of the two optical traps. The orthogonal polarizations of the two traps, as introduced in Section 2.1.2, are typically also the basis for separating the signals for individual

detection. In principle, a polarizing beam-splitter, or just a simple polarization filter, should allow to detect one trap exclusively and block the signal from the second one. In practice, however, a complete distinction of the two signals purely based on polarization is not possible. There are two effects that complicate the signal separation. Firstly, polarization optics have their limitations – as an example, commonly used polarizing beam splitters have an extinction ratio of 'only' 1:100 for the reflected beam, meaning that 1% of the beam is in the 'wrong' polarization state. Secondly and more problematic, the necessary high NA optics cause a partial depolarization of the trapping beams, as visible in Figure 4.1 a. This rotation of the polarization by lens and sample slide surfaces can lead to deviations in the measured forces of up to several pN [Mangeol and Bockelmann 2008]. The resulting parasitic signal, i.e., the depolarized portion of the trapping beams, reaches the wrong detector and contributes to the differential and total signal in a systematic and non-trivial way. This type of error is, for example, especially problematic when weakly correlated movements as, e.g, the hydrodynamic interactions of trapped particles are investigated [Meiners and Quake 1999].

In the literature, several techniques have been presented to achieve improved signal separation. The suggested methods vary in terms of their complexity of implementation, cost, and efficiency. The straight-forward approach is to optimize the polarization based filtering by adding additional polarizers before the quadrant photodiodes. Additional polarization optics and careful alignment of the optics allowed Atakhorrami et al. to reduce the crosstalk level to around 1.5 percent [Atakhorrami et al. 2008]. Mangeol and Bockelmann conducted an in-depth investigation of the origin of the depolarization and introduced a technique termed 'polarization rectification' [Mangeol and Bockelmann 2008]. Here, the trapping beams are sent two times through the microscope, in opposing directions, and a quarter-wave plate is used to compensate for the rotation of the polarization. This back-propagation of the beams through the microscope
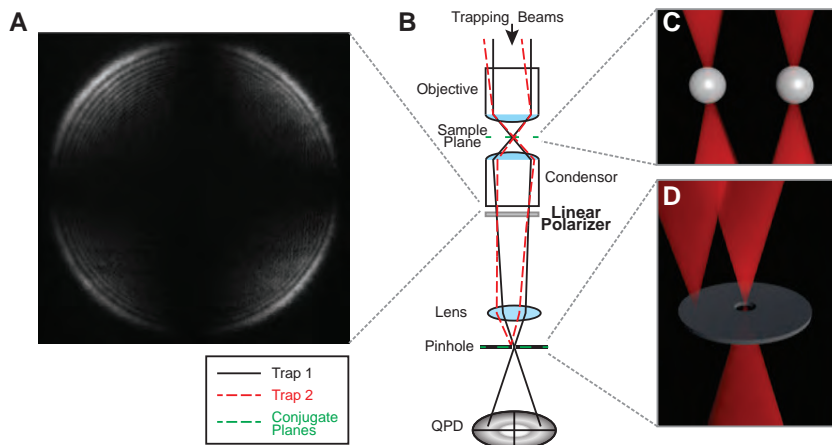
**Figure 4.1.** – **De-polarisation of the trapping beams causes crosstalk in dual-beam optical tweezers.** (a) High NA optics cause the depolarization of the trapping beams. This image shows the remaining intensity when a linear polarized beam is send through the high NA objective and condenser, and all light in the original polarization is blocked by polarizers. The remaining intensity clearly indicates a partial depolarization. Picture adapted from [Mangeol and Bockelmann 2008]. (b) For dual-beam optical tweezers polarization based filtering and signal separation by spatial filtering can be advantageously combined. In practice, this is straight-forward to implement. As shown, we simply added a linear polarizer to the detection path. (c,d) Typical geometry for single molecule force spectroscopy, where the two trapped beads as used as handles to pull on the two opposite ends of a linear molecule, and how the spatial filter selects one single trap for transmission and detection.

rectified the polarization and provided a reduction of the crosstalk levels by a factor 4; however at the expense of having to cope with additional optical traps that are generated by the back-propagating beams. Alternatively, spectral filters in combination with frequency shifting or two separate laser sources of different wavelength can be used to eliminate crosstalk [Atakhorrami et al. 2008; Mangeol and Bockelmann 2008]. A further interesting approach was presented by von Hansen et al., who demonstrated that sequential calibration of the two traps, followed by dedicated signal processing can be used to eliminate crosstalk computationally. The approach relies on auto- and cross-correlational analysis of the tracking signals and makes it possible to deduce the amount of crosstalk and compensate for it in the data analysis [von Hansen et al. 2012].

## 4.2. Crosstalk suppression by combining spatial and polarization based signal separation

The minimal crosstalk for a well-aligned detection system that relies purely on polarization based filtering is around 1.5 percent [Atakhorrami et al. 2008]. As we have seen in Chapter 3, signal separation based on spatial filtering can achieve comparable purity for trap separations of a few microns. Notably, the two methods are compatible with each other and can be combined to obtain an exceptionally high degree of crosstalk suppression. In practice, this combined signal separation technique can easily be implemented by adding both a linear polarizer, anywhere between the condenser and the quadrant photodiode, and a pinhole in the plane conjugate to the sample plane (Fig. 4.1 b). The setup was modified in this way, by placing a linear polarizer in the back focal plane of the condenser, and the resulting crosstalk suppression was quantified. In the evaluation, we followed the same experimental protocol and data analysis, as detailed previously in Section 3.2.
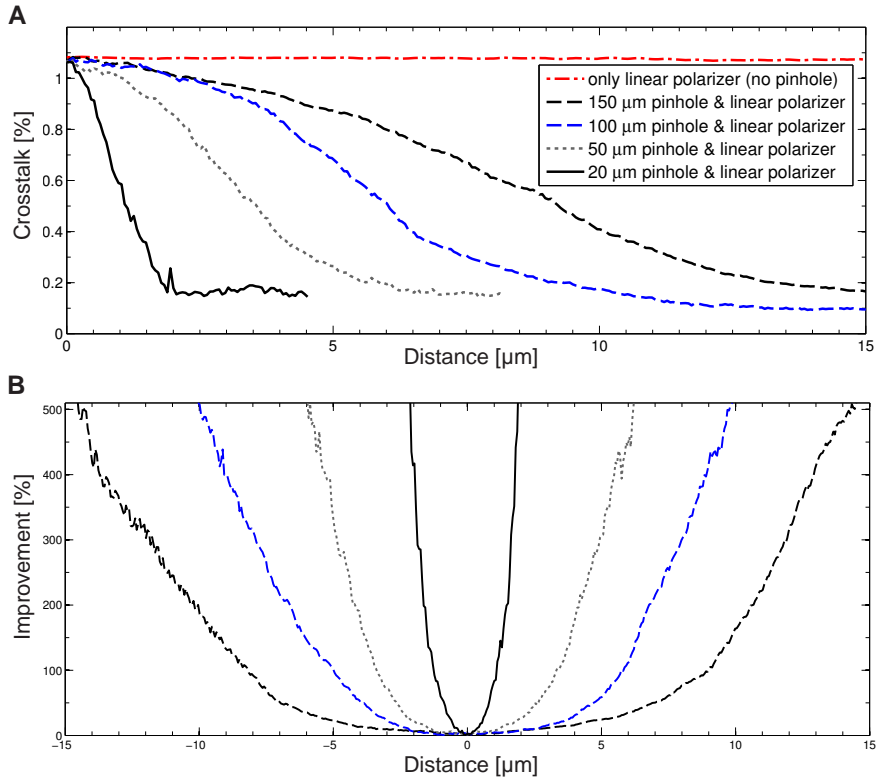
**Figure 4.2.** – **Signal separation by combined approach using spatial and polarization based filtering.** (a) Crosstalk $\Psi_{\mathrm{PH\&LP}}$ as a function of the inter-trap distance. For purely polarization based filtering, the crosstalk value is constant. With increasing inter-trap distance, the additional spatial filtering significantly lowers the crosstalk below this reference level. (b) The improvement $\Omega$ gained from combining the methods is plotted in dependence of the distance separating the traps. This plot was calculated from the data shown in (a) and the legend applies to both graphs.

The results of these experiments are summarized in Figure 4.2. As a reference level, we obtained a crosstalk level of just above 1 percent for the configuration where only the linear polarizer was installed. This is in accordance with the levels reported by Atakhorrami et al. for their setup that contained only polarization based filtering. As no pinhole was present, this value remained constant when increasing the trap separation. For the combined approach, employing both spatial and polarization based filtering, the crosstalk levels matched the reference value when the two traps coincided. With increasing trap separation, the crosstalk levels decreased with increasing trap separation, falling to levels significantly below the reference level that was achievable with polarization optics alone. Due to the very low light intensity of the parasitic signal, higher amplification factors at the signal amplifier had to be used. Consequently, both the fluctuations of the parasitic signal and photodiode's dark noise got amplified leading to a low signal-to-noise ratio for large trap separations, which can be seen as minor fluctuations at low $\Psi$ values.

To quantify the added value of the combined approach, we calculated the quantity $\Omega$

$$\Omega = \frac{\Psi_{\mathrm{LP}} - \Psi_{\mathrm{PH\&LP}}}{\Psi_{\mathrm{PH\&LP}}}, \tag{4.1}$$

which was termed 'improvement', as it quantifies to which extend the combined method reduces crosstalk compared to the standard technique. Here, $\Psi_{\mathrm{LP}}$ refers to the crosstalk value while performing polarization filtering alone and $\Psi_{\mathrm{PH\&LP}}$ to the crosstalk levels for the combined approach. As visible in Figure 4.2 b, the advantage of employing the combined method becomes significant for trap separations of a few micrometers and more. In our setup, with the choice of the optimal pinhole, crosstalk was reduced by up to a factor of five compared to the standard technique. Notably, crosstalk measurements were limited by the noise of the electronics, and not the method itself. This indicates that the crosstalk might be even lower for this combined method, enabling essentially crosstalk-free measurements. This combined signal separation technique improves the ac-

curacy of force-distance measurements that are conducted using dual-beam optical traps, e.g., single molecule force spectroscopy studies, hence guaranteeing more scientific value for the experimental efforts. The results presented in this and the previous chapter were published in an article in the journal Review of Scientific Instruments [Ott et al. 2014b].

# 5. Photodiode based detection for multiple trap optical tweezers

This chapter is concerned with the second application example, i.e., the extension of the presented detection method to simultaneously track multiple particles that are optically manipulated by multiple trap optical tweezers. First, the detection of a single trap out of larger number of holographically generated traps is demonstrated. Here, it is also shown that axial displacement detection can readily be achieved without any modification of the setup. Subsequently, results from the simultaneous tracking of multiple particles are reported. Finally, the limitations of the current setup are clarified and an outlook for future directions is given.

## 5.1. Three-dimensional detection of a single trap in multiple trap optical tweezers

As explained in detail in Section 2.2, it has proven challenging to combine back focal plane interferometry with multiple trap optical tweezers. Here, 'multiple' should be understood as signifying *more than two* traps. To verify that the spatial filtering enables the use of photodiodes, we had to choose an arbitrary, but not trivial, trapping field for our proof-of-concept experiments. We decided to use an arrangement of seven traps, positioned as in a hexagonal lattice, i.e., one central trap surrounded by six traps (Fig. 5.1). A diffractive optical element was
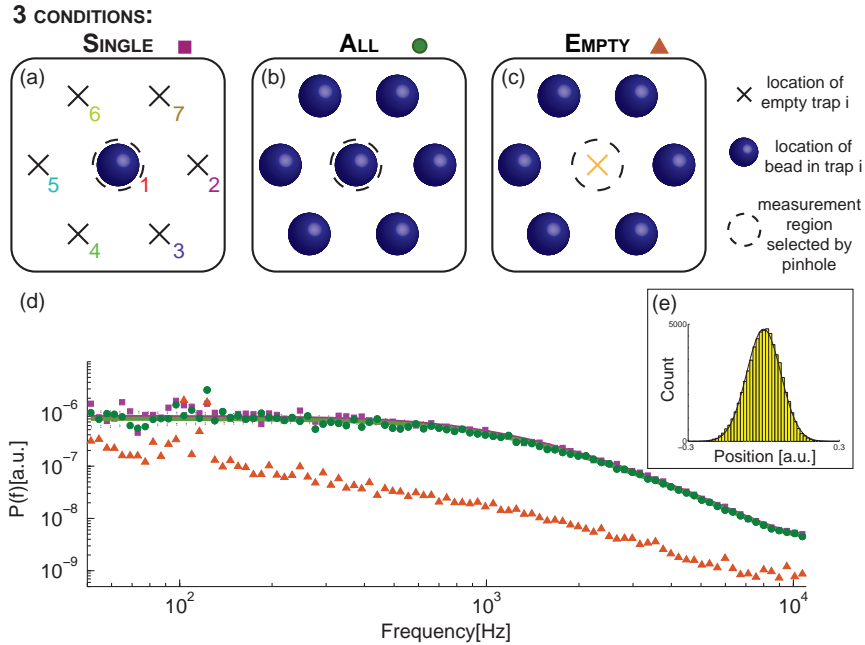
**Figure 5.1.** – **Proof-of-concept experiments with multiple trap optical tweezers.** (a)–(c) Schematic overview of the hexagonal arrangement of the 7 traps. Starting from the central trap, the traps were labeled clockwise. The three different experimental conditions are depicted. In the first configuration, only a single bead occupies the central trap; in the second, all traps contain a bead; in the third, only the central one is empty. (d) Graph showing the measured power spectra for the situations drawn in a) (purple squares), b) (green circles), and c) (orange triangles). Full lines are fits according to the theoretically expected power spectra and dashed lines show the respective uncertainty. For the first two conditions, the power spectra and the estimated corner frequencies agree within their error bars. Orange triangles show the lower magnitude signal for the empty trap in the third condition. (e) Histogram of the positions visited by a bead trapped in the central trap. A fit with the expected Gaussian distribution is overlaid as a full black line.

used to generated this trapping field in the focal plane. Notably, the traps could also have been generated by any other technique, like acoustooptical deflectors, fast scanning mirrors, or the generalized phase contrast technique. The feasibility of the detection method should not be influenced by the way the traps are generated.

In this 7-trap arrangement, neighboring traps were separated by $6.7\mu$m in the sample plane. As mentioned earlier, a relay lens with a longer focal lens was used for these experiments and, by replacing the pinhole with a camera, the distance separating two adjacent traps in this filtering plane was measured to be approximately $40\mu m$. Based on this, we selected pinholes with the diameter of $30\mu m$ and $50\mu m$ for the subsequent measurements.

In a first proof-of-principle experiment of this multiple trap setup, we chose to detect the central trap by aligning the pinhole with the location of this trap. The measured trap characteristics were compared for three configuration that differed regarding the occupancies of the traps (Figs. 5.1 a –5.1 c). In the first configuration, solely the central trap was occupied (Fig. 5.1 a); in the second configuration, all seven traps contained a bead (Fig. 5.1 b); and in the third configuration, the six surrounding traps were occupied, while the central one remained empty (Fig. 5.1 c). Comparison of the power spectra, plotted in Figure 5.1 d, showed that for the two first configurations the measured power spectra were indistinguishable by eye and also yielded the same corner frequency within the error bars. In the third configuration, the signal magnitudes of the captured power spectrum of the empty trap were orders of magnitude lower. Theoretical fits to this power spectrum failed as the characteristic Lorentzian shape was not present. Collectively, these experiments nicely illustrated that the method enabled photodiode based detection of the central trap, while the signal from the remaining surrounding traps was rejected.

Next, to further back these initial experiments, we verified several hallmarks of optical trapping and back focal plane interferometry. Firstly, the linear range
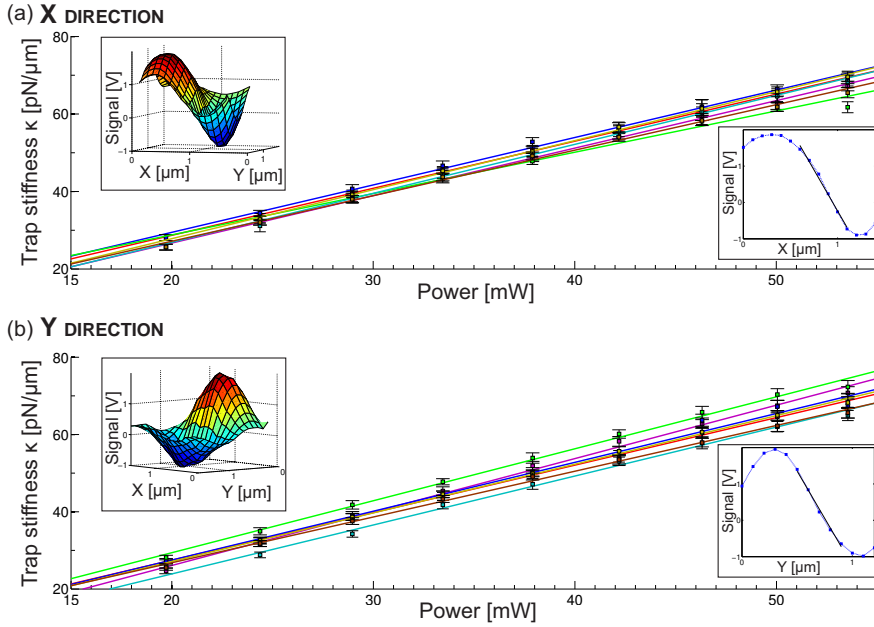
**Figure 5.2. – Dependency of trap stiffness on laser power.** (a) Trap stiffness in x-direction for the seven traps plotted against the trap's laser power in the focal plane. Each data point shows the mean of 30 measurements and is drawn with one standard deviation error bars. Ordinary least square fits (shown as full lines and color-coded according to the trap's colored numbers in Figure 5.1 a) were used to extract the linear power dependency of the trap stiffness for all 7 traps. Upper left inset: Conversion factor map obtained by two-dimensional bead scanning through the focus. The signal of QPD x-channel is plotted against the lateral x- and y-position. Lower right inset: Cross-sectional plot along the x-direction of the 2D conversion factor map shown in the first inset. (b) Same as in a), but for the y-direction.

of the QPD conversion factor was confirmed for all seven traps by bead scanning experiments. These measurements were conducted in the same fashion as detailed in Section 3.1. Representative examples are shown in the insets in Figure 5.2.

A further hallmark of optical trapping is the linear relation between the power of the trapping beam and the resulting trap stiffness. For this purpose, I collected and analyzed a total of 3780 bead trajectories. The resulting graphs are shown in Figure 5.2. Ordinary least square fits to the data confirmed the linear relation for all traps. The respective $R^2$ values were consistently higher than 0.97, indicating good agreement of the collected data and the linear model. The slopes of these linear regressions are determined by the power dependency of the trap stiffness. The analysis revealed a mean value for the seven traps of $(1.205 \pm 0.069)\frac{pN}{\mu m\ mW}$ in the x-direction and $(1.276 \pm 0.067)\frac{pN}{\mu m\ mW}$ in the y-direction. The specifications of the diffractive optical element state that the laser power of the individual traps should have a maximum relative difference of around 5%. The variation of the slopes is in accordance with this expected variation of the trap's power, and the values are comparable to other typical values published for optical tweezers [Rohrbach 2005; Lee et al. 2007b].

As mentioned earlier, photodiode based detection has the distinct advantage over camera based detection that axial detection with high spatial and temporal resolution can easily be achieved. Referring to the explanation in Section 2.2.2, the detection was optimized for axial detection by restricting the condenser aperture and no other modifications to the existing setup were necessary. As earlier for the lateral directions, the different hallmarks of optical trapping and interferometric detection were checked for this axial detection. Briefly, the linear range of the conversion factor was confirmed, the histogram of visited positions by a trapped bead yielded a Gaussian distribution, the measured power spectra were well described by the theory and displayed the expected Lorentzian shape. The results are collected in Figure 5.3. The axial trap stiffness was approximately
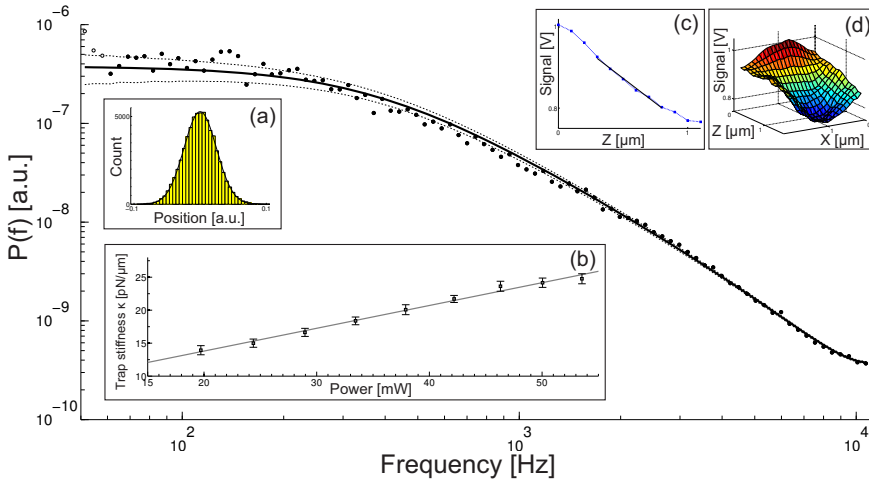
**Figure 5.3.** – **Axial detection capabilities**. The main graph shows the power spectrum of a bead trajectory in the axial direction. Data points are marked as points; the full line is an Lorentzian fit with the error margins as dashed lines. Insets: (a) Histogram of the visited axial positions. (b) Plot confirming the linear power dependency of the trap stiffness. (c) z-channel of the QPD showing a linear range for axial displacements of the bead. (d) Conversion factor map obtained by two-dimensional scanning of an immobilized bead. The total QPD siganl is plotted against the x- and z-position.

a third of the lateral counterpart; a common trap stiffness ratio for optical tweezers. The linear regression ($R^2 > 0.97$) gave a dependency of the axial trap stiffness on the delivered laser power according to $0.345\frac{pN}{\mu m\ mW}$.

## 5.2. Simultaneous detection of multiple traps

So far, the detection method was only used for the tracking of one bead at a time. However, the technique is also applicable to track multiple particles in parallel. We decided to demonstrate this simultaneous detection for three traps. This choice was motivated by two reasons; we only had three diodes and amplifiers available, and it is the smallest number of traps which can not be detected simultaneously using the standard polarization based technique. Parallelization of the detection required adding two additional detection modules – respectively consisting of a pinhole and a quadrant photodiode – to the detection path, as detailed earlier in Section 2.3.3. We arbitrary chose to monitor the Traps 1, 2 and 4, as numbered in Figure 5.1, but any other combination of three traps could have been monitored equally well. Each of the three pinholes was aligned with one of the three traps.

We performed a series of measurements for the two pinhole sizes, measuring power spectra for all possible occupancies of the three traps. All data sets were analyzed as in the previous experiments, and an overview of the calculated corner frequencies is given in Table 5.1. We started by monitoring one single bead that was trapped in either Trap 1, Trap 2, or Trap 4. For each trap, a clear Lorentzian power spectrum appeared when the respective trap was occupied, while a low non-Lorentzian noise signal was obtained for the empty traps (first row in Fig. 5.4). Of note, the corner frequencies obtained for the three traps are very similar, when the trapped bead is transferred from trap to trap between the individual measurements, as was the case for the measurement with the $30\mu m$ pinhole. Subsequently, the traps were sequentially filled, such that always two

**Table 5.1.** – **Overview of the measured corner frequencies.** The arrangement and the numbering of the traps is according to the schematics in Figure 5.4 b. The table is best read row-wise with the occupancy stated on the left. Dashes, '–', denote empty traps with non-Lorentzian power spectra. Sequentially, all possible occupancies were measured. The resulting corner frequencies are stated in Hertz as the mean of 10 measurements with one standard deviation. The upper and lower part of the table contain the results from the experiments conducted with the $30\mu$m and $50\mu$m pinhole, respectively.

| | | | Trap 1 (T1) | | Trap 2 (T2) | | Trap 4 (T4) | |
|---|---|---|---|---|---|---|---|---|
| | | | $30\mu$m pinhole | | | | | |
| occupancy | | | X | Z | X | Z | X | Z |
| T1 | - | - | 482±15 | 201±6 | - | - | - | - |
| - | T2 | - | - | - | 480±18 | 215±6 | - | - |
| - | - | T4 | - | - | - | - | 481±13 | 213±5 |
| T1 | T2 | - | 444±12 | 198±7 | 404±10 | 194±6 | - | - |
| T1 | - | T4 | 422±10 | 194±7 | - | - | 460±10 | 222±9 |
| - | T2 | T4 | - | - | 378±35 | 214±5 | 453±19 | 208±5 |
| T1 | T2 | T4 | 436±10 | 196±6 | 478±18 | 199±7 | 444±13 | 220±9 |

| | | | Trap 1 (T1) | | Trap 2 (T2) | | Trap 4 (T4) | |
|---|---|---|---|---|---|---|---|---|
| occupancy | | | X | Z | X | Z | X | Z |
| T1 | - | - | 449±12 | 195±6 | - | - | - | - |
| - | T2 | - | - | - | 433±14 | 210±9 | - | - |
| - | - | T4 | - | - | - | - | 495±27 | 235±8 |
| T1 | T2 | - | 460±8 | 184±6 | 489±11 | 208±3 | - | - |
| T1 | - | T4 | 460±12 | 187±9 | - | - | 490±17 | 228±10 |
| - | T2 | T4 | - | - | 485±10 | 224±11 | 488±14 | 236±9 |
| T1 | T2 | T4 | 463±15 | 188±4 | 473±9 | 223±6 | 490±8 | 225±9 |

$50\mu$m pinhole

**Figure 5.4. – Simultaneous detection of multiple trapped beads**. The traps were sequentially filled according to the schematics on the left. For each configuration, the corresponding lateral (purple) and axial (green) power spectra of the three traps are shown on the right. For empty traps only the noisy background is visible, while clear power spectra appeared when the traps got occupied by a bead. The pinhole diameter for these experiments was $30\mu$m.

traps contained a bead while one was empty. Again, the expected power spectra appeared when the traps were occupied (second row in Fig. 5.4). The calculated corner frequencies are in reasonable agreement, especially considering the fact that beads with potentially different bead diameters were trapped. Next, we captured power spectra with all three traps being occupied (last row in Fig. 5.4). With this measurement, we were finally able to demonstrate that it is possible to combine back focal plane interferometry and multiple trap optical tweezers and track several particles in parallel. The above reported results were published in the journal Optics Express [Ott et al. 2014a].

## 5.3. Discussion of limitations and outlook

While it is straight-forward to extend the method to the detection of more than three traps, one should keep in mind that each detected trap requires a separate detection module. Therefore, I would state that the approach is only feasible for up to around 10 detected traps, where implementation cost and space become an issue. Also, repeated beam splitting reduces the number of photons per detection module, which eventually decreases the signal-to-noise ratio.

Furthermore, I see two major short-comings of the current setup that have not been solved yet. The first aspect is that all measurements have been conducted with the optical traps being in the same focal plane. While the use of the diffractive optical element was sufficient to generate this planar trapping geometry, it did not allow us to move the traps in the axial direction. A specific strength of holographic optical traps is that optical traps can also be generated outside of the focal plane. The influence of such axially offset traps on the crosstalk levels has yet to be investigated. Interestingly, the posed problem is similar to the situation of confocal detection in confocal microscopy. Here, the challenge is likewise that light originating from planes different from the focal plane should be rejected from reaching the photodetector using a confocal pinhole. Presumably, the amount of axial crosstalk will depend on the axial distance separating the traps and the NA of the focusing objective. For investigating this axial crosstalk, it would be advantageous to build a SLM based optical trapping setup, as this is the most popular implementation of multiple beam optical traps and it would provide valuable data for the common case of axially displaced traps.

The second caveat of the current approach is that the detectable traps need to be static, i.e., the locations of the optical traps have to remain fixed. Unless a displacement of an trap is combined with a displacement of the respective detection pinhole, the trap will move out of the detection volume and the signal will be lost. Again, one of the great advantages of SLM based holographic optical tweezers is that the generated traps can be dynamically moved by continuously

updating the displayed phase-pattern. So this requirement of static traps clearly represents a limitation for the design of new experiments and the applicability of the detection method.

One straight-forward solution to this problem would be to mount the pinholes on motorized micro-positioners and continuously update their position to follow the movements of the respective traps. While this is practically possible by implementing a feedback loop that controls this relocation of the pinholes (the feedback signal could simply be the total signal intensity), it appears as a rather costly and cumbersome solution.

A more attractive solution may be the use of adaptive optical elements to enable the dynamic tracking of movable traps. Namely, spatial light modulators and micro-mirror arrays could be interesting in this regard:

Digital micro-mirror devices (DMDs) are one of the core components of modern light projectors. These DMDs consist of typically more than million small mirrors that can be individually tilted to locally redirect light. By replacing the static pinholes of the current implementation with such a micro-mirror array in the filter plane, it should be possible to selectively reflect light to a quadrant photodiode for detection. The flippable mirrors would essentially act as a dynamically controllable spatial filter. Unfortunately, these off-the-shelf components of consumer products do only allow for a binary flipping between an ON and an OFF state, corresponding to one single deflection angle. This means that the DMD could only be used to route light to one single QPD, i.e., it cannot redirect the light in several different directions to different QPDs. This would leave us with the possibility of a time-shared detection. However, in that case the time-shared optical tweezers with time-shared detection, as presented in Section 2.1.2, appear to be the better solution. On a separate note, analog-operated micro-mirror arrays are also available and allow for a continuously variable deflection tip/tilt angle. They are for example used for aberration compensation in astronomy and optical switching in fiber-optical communication. However, these

are too costly to compete with camera based tracking in terms of price.

Alternatively, one could imagine placing a spatial light modulator in the filter plane. Here, the idea would be to investigate whether pixel sub-groups, displaying phase wedges, can act as dynamically controllable pinholes to locally redirect light from individual traps to different QPDs. It would be interesting to see whether the limited number of pixels would enable an appreciable deflected beam and what other effects might occur due to the discrete nature of the pixels.

Finally, an approach could include the use of a Shack-Hartmann wavefront sensor. In the typical optical arrangement, collimated beams are impinging on the micro-lens array and are focused onto the CCD/CMOS, which is located in the back-focal-plane of the micro-lens array, i.e., at a distance of one focal length behind the micro-lens array. In our case, we would reverse this arrangement. The front-focal-plane of the micro-lens array would coincide with the filter plane, thus, leading to parallel beams leaving the micro-lenses and being detected by the camera pixels. Here, the individual micro-lenses effectively act as the spatial filters, as only light from the regions around each trap enters the adjacent micro-lens and is detected by the pixels behind. The advantage of this arrangement is that we would in fact not have imaging based detection, but interferometric detection. However, on the downside, the lens-array itself might introduce significant aberrations and the sampling speed would be limited by the typical speed of cameras.

I would like to note that these three options should be mainly be considered loose ideas and outlines of possible lines of thought. Before pursuing any of these directions further, it is advisable to carefully reconsider the viability and feasibility of these approaches. Personally, I favor the solution that uses the micro-mirror array, as it provides a good compromise between cost, performance, and the complexity of implementation.

# 6. Side projects – Optical systems design

During my PhD studies, I was involved in several other projects besides the main project discussed so far. Three of them will be summarized in this chapter. The first one is concerned with a new type of optical fiber based optical trap that enables the controlled rotation of single live cells in suspension. The major part of this work was dedicated to the question of how to propagate spatially structured light through optical fibers. The project was started during my Diploma project in the Guck research group – formerly located at the University of Cambridge, United Kingdom, now at the Dresden University of Technology, Germany – and finished recently, resulting in a publication in Nature Communications [Kreysing et al. 2014]. The second project relates to the design and the construction of an optical trapping setup that was built for investigations of nanoscale membrane transitions, which could be induced by localized heating using optically manipulated metallic nanoparticles [Andersen et al. 2014]. The third project lies within the realm of low-cost microscopy for global health and science education and was conducted during a research visit to the Prakash Lab at Stanford University. This work is ongoing and not yet published, so the description is restricted to a motivation of the project and some preliminary results.

## 6.1. Towards single cell tomography: Optically induced rotation of live cells

X-ray imaging made a huge leap forward when the technology was extended to X-ray computed tomography (X-ray CT). The key feature of X-ray CT, enabling the stunning and clinically valuable three-dimensional image reconstructions, is that several two-dimensional images are taken from different viewing angles. We were interested in providing a similar functionality for microscopic samples as, e.g., single biological cells. A variety of microscopy modalities could profit from multi-view imaging from different angles. Briefly and just to name a few applications, the optical resolution of three-dimensional microscopy can be improved towards a more isotropic point spread function [Swoger et al. 2007], mitigating the commonly reduced axial resolution of standard microscopes. Furthermore, object rotation in combination with quantitative phase microscopy enables the determination of three-dimensional refractive index distributions of living cells.

Since the microscopy instruments are much larger than the samples, it appears more feasible to rotate the sample instead of the imaging system. Optical traps are a well suited tool for this task, since they provide highly precise, non-mechanical means to manipulate small objects in liquid solutions. A specific type of optical trap, a so-called fiber based counter-propagating dual-beam trap, is a popular choice for live cell applications as it mitigates the risk of photodamage that is often a concern in optical tweezers [Guck et al. 2001]. In this type of optical trap, two optical fibers are co-axially aligned with their output ends facing each other at a short distance. Normally, both fibers carry Gaussian beams that, upon exiting the fiber, diverge into the small gap that separates the fiber ends (compare Fig. 6.1). Diverging trapping beams are advantageous since the potentially harmful high field intensities of focused beams are avoided. The two counter-propagating beams form an optical trap, since the opposing scattering forces of the beams compensate each other along the axial direction parallel
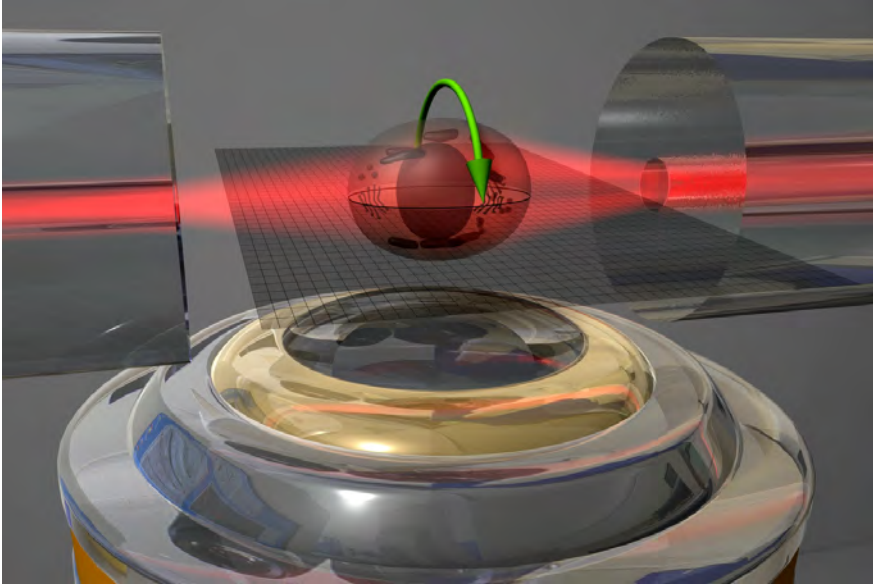
**Figure 6.1.** – **Visualization of optical fiber trap for single cell rotation.**
Two optical fibers, a single mode fiber and a few-mode fiber, are aligned coaxially
with their exit surfaces facing each other. A Gaussian beam (left) and a two-lobed
non-rotational symmetric beam (right) diverge out of the respective fibers and
form an optical trap. The non-rotational symmetric beam enforces an orientation
of trapped objects like, e.g., biological cells. Controlled rotation of the trapped
object can be achieved by rotating the two-lobed beam around its propagation
axis. Importantly, the geometry of the setup enables the rotation of the object
around an axis that is perpendicular to the optical axis of the imaging system
(here depicted by the microscope objective below the optical trap), thus allowing
for tomographic imaging. Figure adapted from [Kreysing et al. 2014].

to the fibers. In the perpendicular direction, an optical well is created by the high local field intensity. To enable sample orientation and rotation, the basic idea is to break the rotational symmetry of at least one of the trapping beams. Given a non-rotational symmetric trapping beam, trapped objects would have a preferred orientation in the optical trap. This is the case since the energy of the system is minimized when the overlap between regions of high field intensity and the sample's components with a high refractive index, e.g., a cell nucleus, is maximized. As a non-rotational symmetric trapping beam, we chose a two-lobed beam, since it resembles the low order fiber modes and thus makes the propagation of this intensity distribution along the optical fiber easier. A visualization of the described method can be seen in Figure 6.1.

The setup that was used to generate the trapping beam, the coupling into the optical fiber, and the delivery to the optical trap are shown in Figure 6.2 a. The key optical element is a spatial light modulator, which can be used to locally modify the wavefront of an incident laser beam. By placing the spatial light modulator in a Fourier plane relative to the input face of the optical fiber, arbitrary intensity distributions could be selectively launched into the fiber. Propagating spatially structured light along an optical fiber is complicated by modal dispersion, and the corresponding differences in propagation constants result in de-phasing of the individual modes during their propagation along the fiber. A few-mode fiber, supporting only the lower order fiber modes, was used to avoid launching an uncontrolled mixture of a high number of modes into the fiber. We were able to show that de-phasing can be dealt with by shortening the fiber to a specific length where the modes' phases matched again, thus allowing to recover the input that was launched into the fiber (Fig. 6.2 b). Figure 6.2 c shows representative examples of the intensities that were measured at the output end of the optical fiber. After combining the optical trapping setup with a microfluidic flow system, the capability of the setup to rotate single cells was demonstrated using two different cell types with distinct morphological
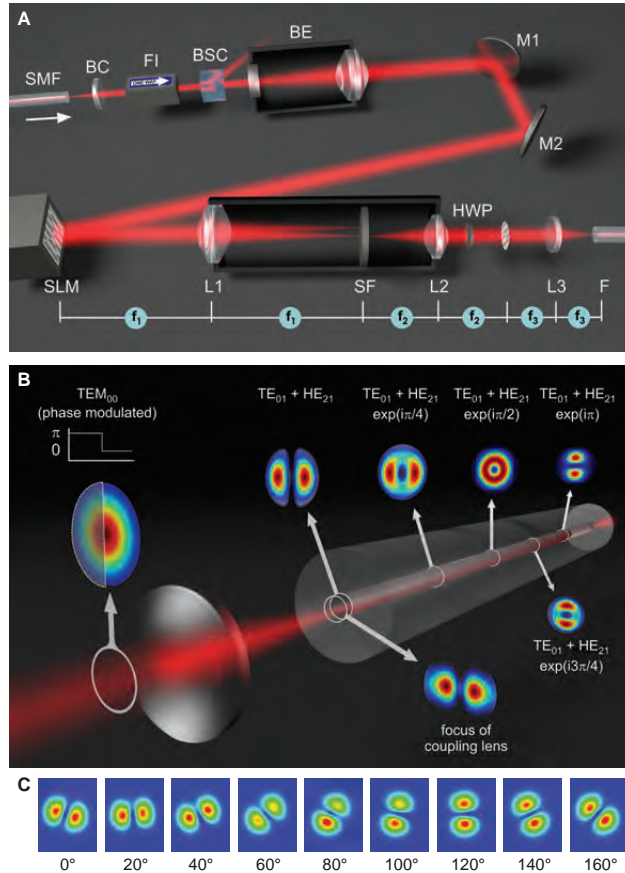
**Figure 6.2.** – **Propagation of spatially structured light through a few mode fiber.** (a) The beam shaping setup. A wavefront-modifying spatial light modulator is placed in a Fourier plane relative to the entrance face of a few mode optical fiber using a 4f-like arrangement of lenses. In this layout, control of the wavefront enables the launching of arbitrary light intensity distributions into the optical fiber. SMF: single mode fiber laser; BC: beam collimator; FI: Faraday isolator; BE: beam expander; M: mirrors; SLM: spatial light modulator; L: lenses; SF: spatial filter; HWP: half wave plate, F: fiber entrance face. (b) Transmission of a two-lobed beam through a few-mode fiber. A Gaussian beam with an imprinted $\pi$ phase-step is imaged onto the input end of a few-mode fiber. The resulting two-lobed intensity distribution couples into the fiber exciting a superposition of the modes that are supported by the few-mode fiber. Among propagation along the fiber, the excited modes de-phase due to their different propagation constants, causing a cross-sectional intensity pattern that varies along the fiber length. At specific locations the de-phasing matches an integer multiple of $2\pi$. By cutting the fiber at one of these locations, the original input intensity can be recovered. (c) Experimental results. The image series shows intensity distributions captured at the output face of the few-mode fiber. The different rotation angles of the two-lobed patterns were generated by varying the intensity distribution that is coupled into the optical fiber. Figure adapted from [Kreysing et al. 2014].
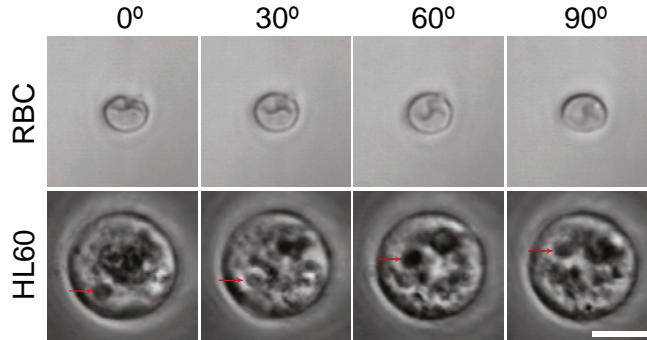
**Figure 6.3.** – **Optical rotation of single suspended cells.** Both the anisotropic intracellular structure of a cell and a non-spherical shape of a cell should lead to an orientation of the cell in the non-rotational symmetric optical trapping beam. This was demonstrated using spherical human leukemia cells (HL60) that feature a rich internal structure and non-spherical red blood cells (RBCs) with minimal internal structure. To guide the eye, red arrows point at a sub-cellular feature and follow it throughout the rotation. Figure adapted from [Kreysing et al. 2014].

features (Figure 6.3). Beside its usefulness for tomographic imaging applications in biophotonics, the controlled rotation of spatially structured light through optical fibers could be instrumental to transmit spatially encoded information for increased bandwidth in fiber based communication.

The study was conceived by Moritz Kreysing and Jochen Guck. I contributed by implementing the setup and performed the cell rotation experiments. Further aspects of this project and experimental details can be found in the publication [Kreysing et al. 2014].

## 6.2. Setup 4: Steerable dual-beam optical tweezers

In this section, I briefly describe a second optical trapping setup that was built to investigate local, temperature induced phase transitions of lipid membranes. To avoid confusion, it is important to note that this setup is a separate setup
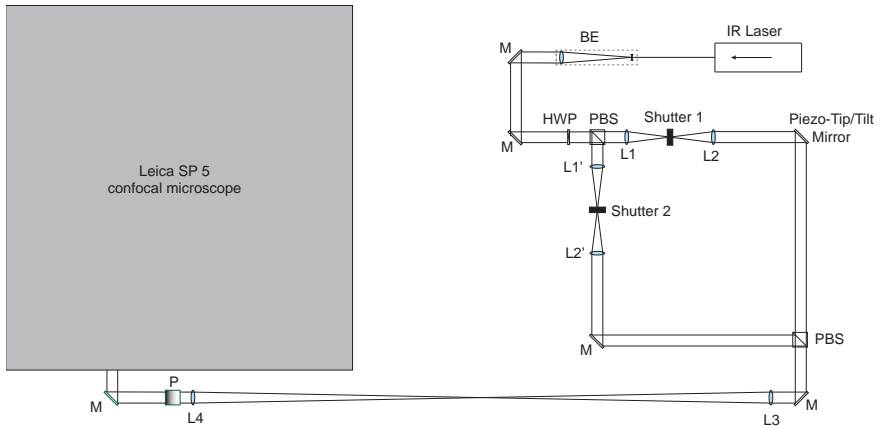
**Figure 6.4.** – **Optical layout of Setup 4.** The optical components are marked with the following abbreviations. BE: Beam expander; M: Mirrors; HWP: Half-wave plate; PBS: Polarizing beam splitter; L1 and L2: Lenses with 7.5cm focal length; L3 and L4: Lenses with 50cm focal length; P: Periscope. Two traps are generated, a movable trap and a second static trap in the center of the field of view. The power ratio of the two traps can be controlled by rotating the half wave plate. The planes of L1, L1', and the piezo-tip/tilt mirror are imaged into the back focal plane of the microscope objective of the Leica SP 5. This provides three-dimensional control for the traps' locations. The axial positions can be changed by axially moving L1 and L1' using the linear translation stages. The lateral position of the movable trap can be adjusted via a Labview program that controls the angular orientation of the piezo-tip/tilt mirror.

from the one that was used for the main PhD project. The following description of the setup intends to serve as a quick reference for group members that want to use or extend the setup.

The layout of the setup is shown in Figure 6.4. It is built around a Leica SP5 light scanning confocal microscope and uses a 1064nm CW DPSS trapping laser. The setup features two traps; one static trap that was aligned to be in the center of the field of view and a second movable trap. The optical layout is similar to the dual-beam optical trap described in Section 2.3.1, however, with certain differences regarding the beam steering and the detection. Independent control of the axial position of the two optical traps was an important design consideration for us. This is achieved by having two separate 1:1-telescopes, one for each trap,

with their first 'beam steering lens' (labeled L1 and L1' in Fig. 6.4) being imaged onto the back focal plane of the microscope objective. Linear translation of these lenses parallel to the beam propagation results in axial displacement of the optical traps. Likewise, lateral trap positioning is enabled by imaging adjustable tip-/tilt mirrors onto the back focal plane of the objective. The mirror belonging to the movable trap is piezo-actuated and can be controlled via Labview. This design, where lateral beam steering is achieved by tiltable mirrors, instead of using movable lenses, reduces optical aberrations and vignetting [Fällman et al. 2006].

On the detection side, two quadrant photodiodes are installed. The first QPD is used for tracking in the lateral directions and the second QPD for tracking in the axial direction. The sensitivity of the axial tracking can be optimized by restricting the detection angle by partially closing an iris, which is located in front of the photodiode. A linear polarizer, mounted on a rotation mount, can be used to select which of the two traps is detected. Additionally, a bandpass filter is installed in front of the QPDs to block stray light originating from the bright field illumination module of the microscope. Valuable recommendations regarding the alignment can for example be found in the following publications: [Lee et al. 2007b] and [van Mameren et al. 2011]. The Appendix contains a list of the optical components and their manufacturers.

By now, several different projects of our group are conducted on this dual-beam optical trap. Two projects, that I am involved in, are the study of *thermophoretic effects on single particles* and the investigation of the *dynamics of cellular nanoparticle uptake for applications within nanomedicine*. A specific application example from the a third, recently finished, study on the physical properties on lipid membranes is summarized in Figure 6.5. This study was conducted by other members of the group and my main contribution to this work was technical support and the implementation of the setup. Further details on this project can be found in the publication [Andersen et al. 2014].
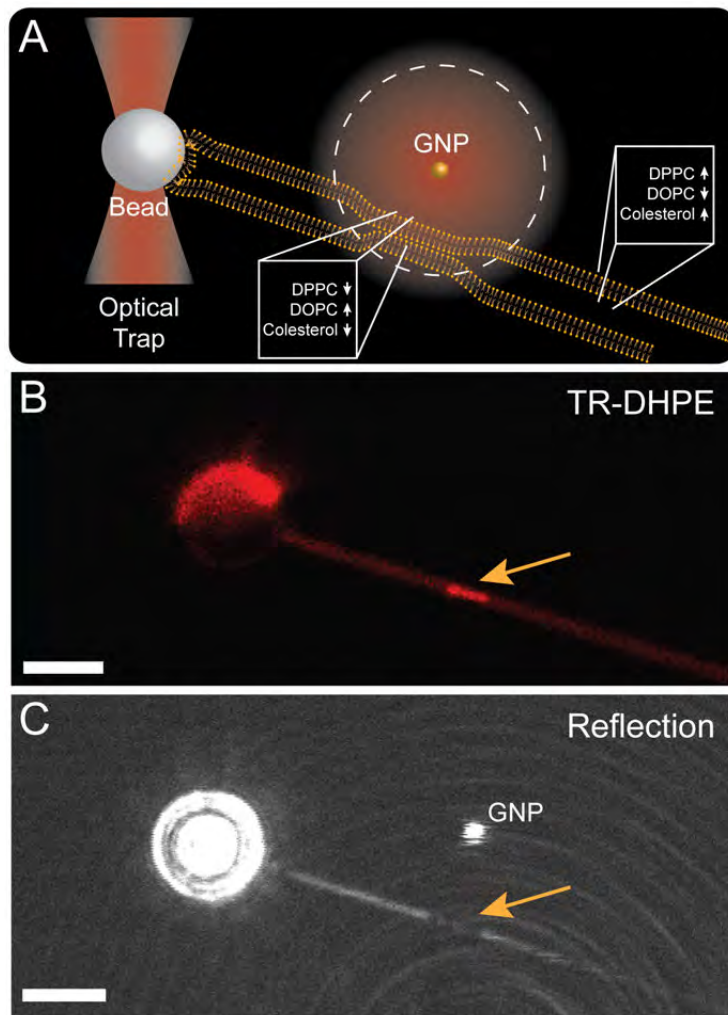
**Figure 6.5.** – **Application example for Setup 4: Heating induced phase transitions on membrane tubes.** (a) A lipid membrane with well controlled curvature can be created by pulling a membrane tube out of a giant unilaminar vesicle using a trapped polystyrene bead. Irradiated gold nanoparticles (GNP) can serve as localized heat sources due their plasmonic properties. By bringing a trapped gold nanoparticle close to the membrane tube, localized phase transitions can be induced. This geometry enables, e.g., studying the effect of membrane curvature on the phase transition temperature and the influence of multiple phases on the distribution of the contained lipids. (b) Fluorescence image showing the partitioning of a phase-sensitive dye into a region of the membrane tube that was melted by an adjacent gold nanoparticle. (c) The reflection signal of the situation in (b) shows the trapped gold nanoparticle and the polystyrene bead.

## 6.3. Foldscope

As part of the PhD program, I had the chance to visit the Prakash Lab at Stanford University, California. One of the group's research areas is 'Frugal science'. Their frugal approach to science can be understood in several different ways, and one very important aspect to point out here is that they consider scalability, in terms of cost and manufacturing, early on into a project. Frugal science aims at finding scalable solutions to democratize science and the access to scientific tools. In this context, Cybulski et al. have developed a low-cost, paper-based microscope, called Foldscope, aiming at increasing the accessibility to microscopy around the world [Cybulski et al. 2014]. The vision of providing "one microscope for every child" and affordable disease diagnostics in low resource settings (microscopy is still the gold standard for many diseases) are the driving ideas behind this project. In a pilot project, 50000 units have been shipped to people around the globe. This broad dissemination within science education and global health is possible, as the complete microscope costs less than one dollar. This low price is attained since the platform uses low-cost ball lenses as optics and folded paper to form the translation stages (Fig. 6.6).

During the research visit in the Prakash Lab, I joined this project and worked on developing improved optical layouts of the microscope. In particular, the focus of my work was to improve the different imaging modalities that were presented in the original paper by Cybulski et al.: Bright field and dark field imaging, and fluorescence microscopy. For bright field microscopy, well controlled illumination, by either critical or Köhler illumination, is important to guarantee a high image contrast and avoid image deterioration by effects like inhomogeneous illumination. To this end, I developed a simplified version of standard Köhler illumination for Foldscope, termed 'Pseudo-Köhler illumination'. The illumination module was modeled in the optical design software Zemax and subsequently implemented (Fig.6.7 b). Regarding dark field illumination, I designed a second Zemax model to improve the positioning of the dark field stop (Fig. 6.7 a).
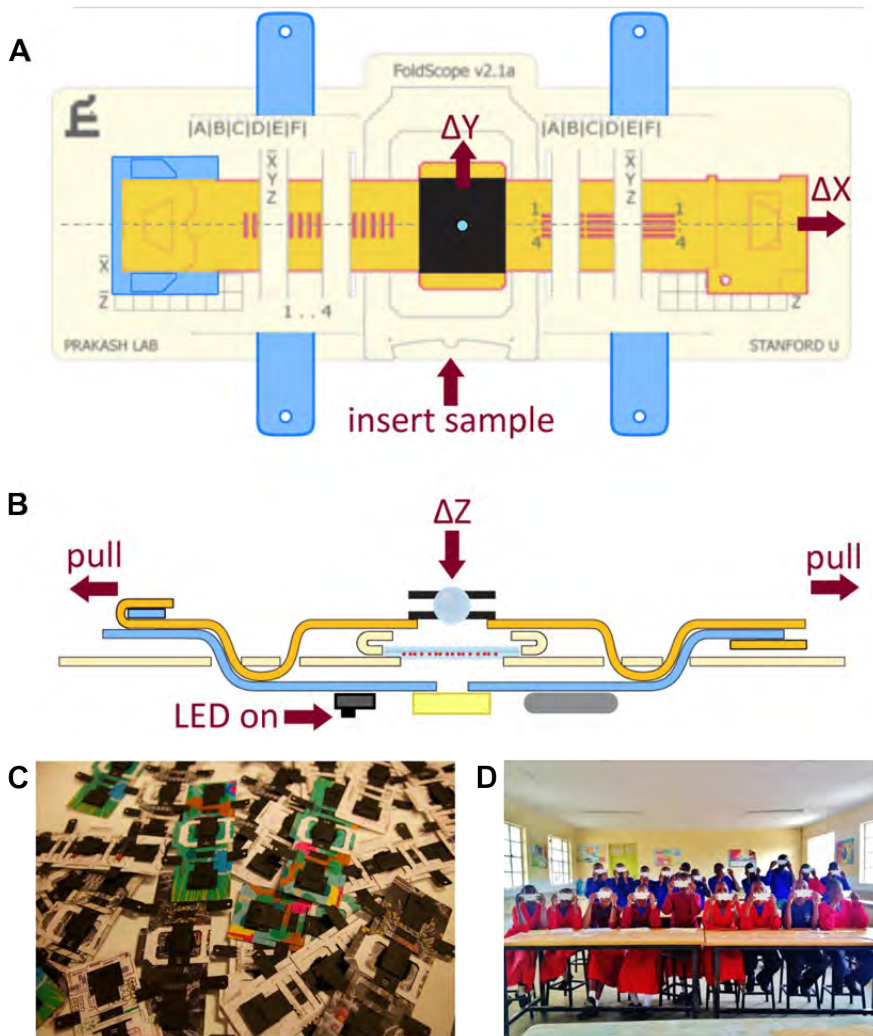
**Figure 6.6.** – **Foldscope project.** (a,b) Schematic drawing of the low-cost microscope, which can be folded from a single A4-piece of die-cut paper. The stage for XY-panning, moving the optics relative to the sample slide, is marked in blue and yellow. Focusing is based on the flexure of the folded paper and controlled by pulling the glass sphere, i.e., the objective lens, closer to the sample slide, as illustrated in the side view. (c) Picture of a pile of assembled Foldscopes that were produced using low-cost, large-scale manufacturing. (d) Foldscope is aiming at having an impact in science education and global health by increasing the accessibility to microscopes worldwide. As of today, 50000 Foldscopes have been shipped to people around the world. Figures adapted from www.foldscope.com and [Cybulski et al. 2014].
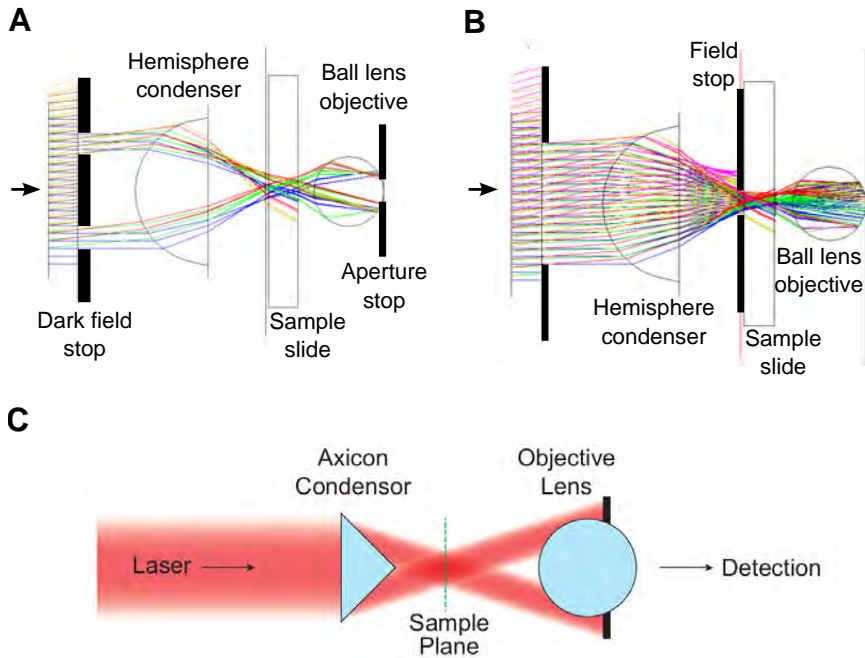
**Figure 6.7. – Optical designs for low-cost microscope.** (a) Zemax ray trac-
ing model of a dark field illumination module for Foldscope. Rays are launched
from the left. A dark field stop in the back focal plane of the half-ball condenser
lens creates a hollow illumination cone. An aperture stop restricts the numerical
aperture of the ball lens objective such that only light scattered by the sample
enters the objective. (b) Zemax model of the 'Pseudo-Köhler illumination' mod-
ule. The typical collector lens is omitted and an aperture in the proximity of the
sample plane acts as an alternative field stop. (c) Schematic of optical layout of
low-cost fluorescence microscope. The axicon provides a dark field-like illumina-
tion by creating a hollow cone of excitation light. Using simple plastic color filters
and crossed polarizers, the emitted light is selectively transmitted to the detector,
while the excitation light is blocked.

Furthermore, I contributed to the development of a disease specific fluorescence version of Foldscope. The aim is to conduct tuberculosis diagnostics using Auramine O, a fluorescent stain that displays a large Stokes shift and can be excited using low-cost Blu-Ray laser diodes. Research grade fluorescence microscopes rely on high-quality spectral filtering to separate the emitted fluorescence light from the excitation light. Unfortunately, the high price of these filters prohibits their use in a low-cost microscope. To implement fluorescence detection, we envisaged instead an optical layout that combines several low-cost filtering methods to guarantee a high signal-to-noise ratio of the fluorescence signal. Namely, the optical design contained cross-polarized, dark field illumination using an axicon and low-cost plastic color filters (Fig.6.7 c).

A general problem with using small ball lenses as microscope objectives is that resolution, which increases with smaller glass sphere radii, comes at the expense of field of view. A larger field of view is desirable, e.g., when searching for blood-borne parasites. This prompted us (Manu Prakash, Jim Cybulski and me) to investigate different means of sample purification, with the aim to reduce the sample volume that has to be imaged when, e.g., screening a patient sample for pathogens. This work lead to the development of a low-cost, portable and hand-powered centrifugation device. It is estimated to cost less than a dollar per unit and provides 4000 revolutions per minute, or 400 g in terms of g-force. Further improvements for higher rotation speeds and g-forces appear feasible. However, already now, according to our preliminary results, the device enables clinically relevant hematocrit measurements, i.e., determining the red blood cell content from a drop of blood from a fingerprick, buffy coat examination for a differential white blood cell count, and separation of blood plasma, which is valuable for rapid diagnostic tests (RDTs) in low resource settings.

# 7. Conclusion

In this PhD thesis, the possibility of combining back focal plane interferometry with multiple beam optical traps was explored. The idea of using spatial filtering in a plane conjugate to the sample plane to separate the tracking signals from different optical traps was presented and subsequently evaluated in different optical trapping setups and configurations.

Initial proof-of-principle experiments on single beam optical tweezers confirmed the feasibility of the method and showed that the insertion of a pinhole into the detection path does not have a measurable influence on the estimated trap stiffness. It was also shown that well known hallmarks of back focal plane interferometry remain valid, e.g., the linear relation between small displacements of the bead from its equilibrium position and the resulting QPD voltage signals.

The method's efficiency to suppress parasitic signals from nearby traps was quantified experimentally and backed by simulations. The experiments revealed a dependency on the distance separating the traps – the parasitic signal decreases with increasing trap separation. It was also found that there is a linear relation between the pinhole size and how efficiently the pinhole blocks parasitic signals, which enables the estimation of expectable crosstalk levels for pinhole sizes that were not measured explicitly.

It was shown that the spatial filtering based signal separation technique can be advantageously combined with polarization based filtering to eliminate crosstalk in the detection of dual-beam optical tweezers. Compared to the standard technique that relies purely on polarization, this combined technique re-

duced crosstalk levels by a factor of five, enabling essentially crosstalk-free measurements.

An extended version of the setup was built to demonstrate the possibility to interferometrically track multiple particles in parallel in holographic optical traps. First, proof-of-concept measurements were conducted detecting single traps out of a larger number of holographically generated traps. Several hallmarks of optical trapping as, e.g., the linear dependency of the trap stiffness on the applied laser power, were confirmed. Here, it was also shown that the method enables the use of photodiodes for axial tracking. Next, results on the simultaneous tracking of multiple beads in holographic optical tweezers were reported. In summary, these results confirmed that the proposed method indeed enables photodiode based detection by back focal plane interferometry for multiple trap optical tweezers.

Finally, the current implementation of the method was scrutinized and its limitations clarified. The main drawback is seen in the requirement of static traps, and several methods to enable the tracking of movable traps were proposed. Employing adaptive optical elements for dynamic and programmable spatial filtering appears as the most promising solution for further improvements of the reported method.

# References

T. Andersen, A. Bahadori, D. Ott, A. Kyrsting, S. N. S. Reihani, and P. M. Bendix. Nanoscale phase behavior on flat and curved membranes. *Nanotechnology*, 25(50): 505101, 2014.

M. Andersson, F. Czerwinski, and L. B. Oddershede. Optimizing active and passive calibration of optical tweezers. *Journal of Optics*, 13(4):044020, 2011.

A. Ashkin. Acceleration and trapping of particles by radiation pressure. *Physical Review Letters*, 24(4):156–159, 1970.

A. Ashkin. Optical trapping and manipulation of neutral particles using lasers. *Proceedings of the National Academy of Sciences of the United States of America*, 94 (10):4853–4860, 1997.

A. Ashkin. History of Optical Trapping and Manipulation of Small-Neutral Particle, Atoms, and Molecules. *IEEE Journal on Selected Topics in Quantum Electronics*, 6(6):841–856, 2000.

A. Ashkin, J. M. Dziedzic, J. E. Bjorkholm, and S. Chu. Observation of a single-beam gradient force optical trap for dielectric particles. *Optics Letters*, 11(5):288, 1986.

M. Atakhorrami, K. M. Addas, and C. F. Schmidt. Twin optical traps for two-particle cross-correlation measurements: eliminating cross-talk. *Review of Scientific Instruments*, 79(4):043103, 2008.

K. Berg-Sørensen and H. Flyvbjerg. Power spectrum analysis for optical tweezers. *Review of Scientific Instruments*, 75(3):594, 2004.

# References

K. Berg-Sørensen, L. Oddershede, E.-L. Florin, and H. Flyvbjerg. Unintended filtering in a typical photodiode detection system for optical tweezers. *Journal of Applied Physics*, 93(6):3167, 2003.

M. Born and E. Wolf. *Principles of Optics: Electromagnetic Theory of Propagation, Interference and Diffraction of Light.* Cambridge University Press, Cambridge, UK, 1999. ISBN 0521784492.

R. Bowman, G. Gibson, and M. Padgett. Particle tracking stereomicroscopy in optical tweezers: Control of trap shape. *Optics Express*, 18(11):11785–90, 2010.

R. W. Bowman and M. J. Padgett. Optical trapping and binding. *Reports on Progress in Physics*, 76(2):026401, 2013.

F. Cheong, B. Sun, R. Dreyfus, J. Amato-Grill, K. Xiao, L. Dixon, and D. G. Grier. Flow visualization and flow cytometry with holographic video microscopy. *Optics Express*, 17(15):13071—-79, 2009.

F. Cheong, B. Krishnatreya, and D. Grier. Strategies for three-dimensional particle tracking with holographic video microscopy. *Optics Express*, 18(13):13563–13573, 2010.

D. B. Conkey, R. P. Trivedi, S. R. P. Pavani, I. I. Smalyukh, and R. Piestun. Three-dimensional parallel particle manipulation and tracking by integrating holographic optical tweezers and engineered point spread functions. *Optics Express*, 19(5):3835–42, 2011.

J. Cybulski, J. Clements, and M. Prakash. Foldscope: Origami-based paper microscope. *PLOS ONE*, 2014.

R. T. Dame, M. C. Noom, and G. J. L. Wuite. Bacterial chromatin organization by H-NS protein unravelled using dual DNA manipulation. *Nature*, 444(7117):387–90, 2006.

K. Dholakia and P. Reece. Optical micromanipulation takes hold. *Nano Today*, 1(1): 18–27, 2006.

K. Dholakia, P. Reece, and M. Gu. Optical micromanipulation. *Chemical Society Reviews*, 37(1):42–55, 2008.

R. Di Leonardo, S. Keen, J. Leach, C. Saunter, G. Love, G. Ruocco, and M. Padgett. Eigenmodes of a hydrodynamically coupled micron-size multiple-particle ring. *Physical Review E*, 76(6):061402, 2007.

J. K. Dreyer, K. Berg-Sørensen, and L. Oddershede. Improved axial position detection in optical tweezers measurements. *Applied Optics*, 43(10):1991–5, 2004.

E. R. Dufresne and D. G. Grier. Optical tweezer arrays and optical substrates created with diffractive optics. *Review of Scientific Instruments*, 69(5):1974, 1998.

E. Fällman and O. Axner. Design for fully steerable dual-trap optical tweezers. *Applied Optics*, 36(10):2107–13, 1997.

E. Fällman, M. Andersson, and O. Axner. Techniques for moveable traps: the influence of aberration in optical tweezers. *Proceedings of SPIE*, 6008:E881–E881, 2006.

A. Farré, F. Marsà, and M. Montes-Usategui. Optimized back-focal-plane interferometry directly measures forces of optically trapped particles. *Optics Express*, 20(11): 12270–91, 2012.

J. Finer, R. Simmons, and J. Spudich. Single myosin molecule mechanics: piconewton forces and nanometre steps. *Nature*, 368:113–119, 1994.

L. Friedrich and A. Rohrbach. Tuning the detection sensitivity: a model for axial backfocal plane interferometric tracking. *Optics Letters*, 37(11):2109–11, 2012.

G. M. Gibson, J. Leach, S. Keen, A. J. Wright, and M. J. Padgett. Measuring the accuracy of particle position and force in optical tweezers using high-speed video microscopy. *Optics Express*, 16(19):14561—-70, 2008.

F. Gittes and C. F. Schmidt. Interference model for back-focal-plane displacement detection in optical tweezers. *Optics Letters*, 23(1):7–9, 1998.

T. Godazgar, R. Shokri, and S. N. S. Reihani. Potential mapping of optical tweezers. *Optics Letters*, 36(16):3284–6, 2011.

# References

D. G. Grier and Y. Roichman. Holographic optical trapping. *Applied Optics*, 45(5): 880–7, 2006.

P. Gross, N. Laurens, L. B. Oddershede, U. Bockelmann, E. J. G. Peterman, and G. J. L. Wuite. Quantifying how DNA stretches, melts and changes twist under tension. *Nature Physics*, 7(9):731–736, 2011.

J. Guck, R. Ananthakrishnan, H. Mahmood, T. J. Moon, C. C. Cunningham, and J. Käs. The optical stretcher: a novel laser tool to micromanipulate cells. *Biophysical Journal*, 81(2):767–84, 2001.

W. H. Guilford, J. A. Tournas, D. Dascalu, and D. S. Watson. Creating multiple time-shared laser traps with simultaneous displacement detection using digital signal processing hardware. *Analytical Biochemistry*, 326(2):153–66, 2004.

P. M. Hansen, I. M. Tolić-Nørrelykke, H. Flyvbjerg, and K. Berg-Sørensen. tweezercalib 2.0: Faster version of MatLab package for precise calibration of optical tweezers. *Computer Physics Communications*, 174(6):518–520, 2006.

R. F. Hay, G. M. Gibson, M. P. Lee, M. J. Padgett, and D. B. Phillips. Four-directional stereo-microscopy for 3D particle tracking with real-time error evaluation. *Optics Express*, 22(15):18662—-18667, 2014.

I. Heller, G. Sitters, O. D. Broekmans, G. Farge, C. Menges, W. Wende, S. W. Hell, E. J. G. Peterman, and G. J. L. Wuite. STED nanoscopy combined with optical tweezers reveals protein dynamics on densely covered DNA. *Nature Methods*, 10(9): 910–6, 2013.

R. Huang, I. Chavez, K. M. Taute, B. Lukić, S. Jeney, M. G. Raizen, and E.-L. Florin. Direct observation of the full transition from ballistic to diffusive Brownian motion in a liquid. *Nature Physics*, 7(7):576–580, 2011.

A. Huhle, D. Klaue, H. Brutzer, P. Daldrop, S. Joo, O. Otto, U. F. Keyser, and R. Seidel. Camera-based three-dimensional real-time particle tracking at kHz rates and Ångström accuracy. *Nature Communications*, 6:5885, 2015.

J. H. G. Huisstede, K. O. Van der Werf, M. L. Bennink, and V. Subramaniam. Force detection in optical tweezers using backscattered light. *Optics Express*, 13(4):378–386, 2005.

S. Keen, J. Leach, G. Gibson, and M. J. Padgett. Comparison of a high-speed camera and a quadrant detector for measuring displacements in optical tweezers. *Journal of Optics A: Pure and Applied Optics*, 9(8):264—-266, 2007.

M. Kreysing, D. Ott, M. J. Schmidberger, O. Otto, M. Schürmann, E. Martín-Badosa, G. Whyte, and J. Guck. Dynamic operation of optical fibres beyond the single-mode regime facilitates the orientation of biological cells. *Nature Communications*, 5:5481, 2014.

S. Lee, Y. Roichman, G. Yi, S.-h. Kim, S.-M. Yang, A. van Blaaderen, P. van Oostrum, and D. G. Grier. Characterizing and tracking single colloidal particles with video holographic microscopy. *Optics Express*, 15(26):18275–18282, 2007a.

W. M. Lee, P. J. Reece, R. F. Marchington, N. K. Metzger, and K. Dholakia. Construction and calibration of an optical trap on a fluorescence optical microscope. *Nature Protocols*, 2(12):3226–38, 2007b.

V. N. Mahajan. Uniform versus Gaussian beams: a comparison of the effects of diffraction, obscuration, and aberrations. *Journal of the Optical Society of America A*, 3 (4):470, 1986.

P. Mangeol and U. Bockelmann. Interference and crosstalk in double optical tweezers using a single laser source. *Review of Scientific Instruments*, 79(8):083103, 2008.

F. Marsà, A. Farré, E. Martín-Badosa, and M. Montes-Usategui. Holographic optical tweezers combined with back-focal-plane displacement detection. *Optics Express*, 21(25):30282—-30294, 2013.

J.-C. Meiners and S. R. Quake. Direct Measurement of Hydrodynamic Cross Correlations between Two Particles in an External Potential. *Physical Review Letters*, 82 (10):2211–2214, 1999.

# References

J. R. Moffitt, Y. R. Chemla, S. B. Smith, and C. Bustamante. Recent advances in optical tweezers. *Annual Review of Biochemistry*, 77:205–28, 2008.

K. C. Neuman and S. M. Block. Optical trapping. *Review of Scientific Instruments*, 75(9):2787–809, 2004.

M. Noom, B. V. D. Broek, J. van Mameren, and G. J. L. Wuite. Visualizing single DNA-bound proteins using DNA as a scanning probe. *Nature Methods*, 4(12):1031–1036, 2007.

D. Ott, S. Nader, S. Reihani, and L. B. Oddershede. Simultaneous three-dimensional tracking of individual signals from multi-trap optical tweezers using fast and accurate photodiode detection. *Optics Express*, 22(19):23661, 2014a.

D. Ott, S. N. S. Reihani, and L. B. Oddershede. Crosstalk elimination in the detection of dual-beam optical tweezers by spatial filtering. *Review of Scientific Instruments*, 85(May):053108, 2014b.

O. Otto, F. Czerwinski, J. L. Gornall, G. Stober, L. B. Oddershede, R. Seidel, and U. F. Keyser. Real-time particle tracking at 10,000 fps using optical fiber illumination. *Optics Express*, 18(22):22722–33, 2010.

C. Pacoret and S. Régnier. Invited Article: A review of haptic optical tweezers for an interactive microworld exploration. *Review of Scientific Instruments*, 84(8):081301, 2013.

M. Padgett and R. Di Leonardo. Holographic optical tweezers and their relevance to lab on chip devices. *Lab on a Chip*, 11(7):1196–1205, 2011.

T. Perkins. Optical traps for single molecule biophysics: a primer. *Laser & Photonics Review*, 3(1-2):203–220, 2009.

A. Pralle, M. Prummer, E. L. Florin, E. H. Stelzer, and J. K. Hörber. Three-dimensional high-resolution particle tracking for optical tweezers by forward scattered light. *Microscopy Research and Technique*, 44(5):378–86, 1999.

S. N. S. Reihani, S. A. Mir, A. C. Richardson, and L. B. Oddershede. Significant improvement of optical traps by tuning standard water immersion objectives. *Journal of Optics*, 13(10):105301, 2011.

A. C. Richardson, S. N. S. Reihani, and L. B. Oddershede. Non-harmonic potential of a single beam optical trap. *Optics Express*, 16(20):15709–15717, 2008.

A. Rohrbach. Stiffness of Optical Traps: Quantitative Agreement between Experiment and Electromagnetic Theory. *Physical Review Letters*, 95(16):168102, 2005.

D. Ruh, B. Tränkle, and A. Rohrbach. Fast parallel interferometric 3D tracking of numerous optically trapped particles and their hydrodynamic interaction. *Optics Express*, 19(22):21627–42, 2011.

C. Schmitz, J. Spatz, and J. Curtis. High-precision steering of multiple holographic optical traps. *Optics Express*, 13(21):8678–85, 2005.

D. J. Stevenson, F. Gunn-Moore, and K. Dholakia. Light forces the pace: optical manipulation for biophotonics. *Journal of Biomedical Optics*, 15(4):041503, 2012.

J. Sung, S. Sivaramakrishnan, A. R. Dunn, and J. A. Spudich. *Methods in Enzymology: Single-molecule dual-beam optical trap analysis of protein structure and function*, volume 475. Elsevier, 2010.

K. Svoboda and S. M. Block. Biological applications of optical forces. *Annual Review of Biophysics and Biomolecular Structure*, 23:247–85, 1994.

J. Swoger, P. Verveer, K. Greger, J. Huisken, and E. H. K. Stelzer. Multi-view image fusion improves resolution in three-dimensional microscopy. *Optics Express*, 15(13): 8029–42, 2007.

I. M. Tolić-Nørrelykke, K. Berg-Sørensen, and H. Flyvbjerg. MatLab program for precision calibration of optical tweezers. *Computer Physics Communications*, 159 (3):225–240, 2004.

M. Towrie, S. W. Botchway, A. Clark, E. Freeman, R. Halsall, A. W. Parker, M. Prydderch, R. Turchetta, A. D. Ward, and M. R. Pollard. Dynamic position and force

measurement for multiple optically trapped particles using a high-speed active pixel sensor. *Review of Scientific Instruments*, 80(10):103704, 2009.

A. van der Horst and N. R. Forde. Calibration of dynamic holographic optical tweezers for force measurements on biomaterials. *Optics Express*, 16(25):20987–1003, 2008.

J. van Mameren, G. J. L. Wuite, and I. Heller. Introduction to optical tweezers: background, system designs, and commercial solutions. *Methods in molecular biology*, 783:1–20, 2011.

K. Visscher, S. Gross, and S. Block. Construction of multiple-beam optical traps with nanometer-resolution position sensing. *IEEE Journal of Selected Topics in Quantum Electronics*, 2(4):1066–1076, 1996.

Y. von Hansen, A. Mehlich, B. Pelz, M. Rief, and R. R. Netz. Auto- and cross-power spectral analysis of dual trap optical tweezer experiments using Bayesian inference. *Review of Scientific Instruments*, 83(9):095116, 2012.

J. Zhou, V. Schweikhard, and S. M. Block. Single-molecule studies of RNAPII elongation. *Biochimica et Biophysica Acta*, 1829(1):29–38, 2013.

# A. Appendix

The content of the Appendix is mainly intended as a reference for students in the 'Optical Tweezers Group'.

## A.0.1. List of equipment

Within the period of my PhD studies, two new optical setups were implemented in the lab. In the group, they are referred to as 'Setup 1' and 'Setup 4'. For reference and to make possible future modifications to the setup easier, I have prepared an overview table listing the components that were used for building these two setups (Table A.1).

## A.0.2. Labview program for bead scanning experiments

I used the common 'bead scanning' technique to figure out how displacements of a trapped bead are reflected in changes of the quadrant photodiode's voltage signals. Here, the QPD signals are recorded while an immobilized bead is scanned through the focus. This provides a 'conversion factor map' that allows to calculate the absolute position of the trapped object from the measured voltage signals. I have written a Labview program to automate this specific type of measurement. The program can be found on the PC of Setup 1, and a screenshot of the Labview control panel can be seen in Figure A.1. The immobilized bead should be brought into the same plane where a trapped bead has its equilibrium position. Practically, this is difficult to guarantee, so the program is written to capture two-dimensional scans in several planes. A control loop moves the stage

**Table A.1.** – **Tabulated list of equipment.** The table lists the manufacturer and the product number of the most important optical and electrical components that were used for building the two setups. Setup 1 refers to the dual-beam optical trapping setup that was used for the spatial filtering experiments. Setup 4 refers to the dual-beam optical trap that was integrated into the Leica confocal microscopy system and enabled the tube pulling experiments.

| Item | | | |
|---|---|---|---|
| Product | Manufacturer | Product number | used in setup |
| 1064 nm CW Nd:YVO$_4$ laser | Spectra Physics | J20I-BL-106C-02 | 1 & 4 |
| Inverted microscope | Leica | DM IRBE | 1 |
| Confocal microscope | Leica | SP 5 | 4 |
| 1.2 NA water immersion objective | Leica | HcxPlApo Wcorr CS | 1 & 4 |
| 1.4 NA oil immersion condenser | Leica | S1 551004 | 4 |
| Piezo-actuated sample stage | Physik Instrumente | P-517.3CL | 1 |
| Piezo-actuated sample tage | Mad City Labs | Nano-LPS100 | 4 |
| Translation stages for pinhole | Thorlabs | ST1XY-D | 1 |
| Si-PIN quadrant photodiodes | Hamamatsu | S5981 | 1 & 4 |
| Amplifiers | built in-house | – | 1 & 4 |
| Analog-to-digital-converter | National Instruments | NI PCI-MIO-16E-4 | 1 & 4 |
| Linear actuator (beam steering) | Newport | Pico 9066-X-P-M | 1 |
| Diffractive optical element | HOLO/OR LTD. | MS-231-I-Y-A | 1 |
| Piezo-actuated tip-tilt mirror | Mad City Labs | Nano-MTA2x | 4 |
| 1:1-telescope lenses | Thorlabs | LA1050-C | 1 |
| Relay lens | Thorlabs | LBF254-075 | 1 & 4 |
| Non-polarizing beam-splitter | Thorlabs | BS011 / BS014 | 1 & 4 |
| Shutters | built in-house | – | 1 & 4 |
| 0.96$\mu$m polystyrene beads | Bangs Laboratories | PS03N/9396 | 1 & 4 |
| Beam expander | CASIX Inc. | LBE0201-1064 | 4 |
| Half-wave plate | CASIX Inc. | WPZ1225-L/2-1064 | 4 |
| Neutral-density filter | Thorlabs | NE NIR02 / NIR10 | 4 |
| 1:1-telescope lenses | Thorlabs | LA1145-C / LA1380-C | 4 |
| IR mirrors | Thorlabs | BB1-E03 | 1 & 4 |
| Polarizing beam-splitter | Thorlabs | PBS253 | 1 & 4 |
| Dichroic mirrors | Chroma | T700dcspxru | 1& 4 |
| Linear polarizer | Thorlabs | LPNIR100 | 1 & 4 |
| Bandpass filter | Thorlabs | FL1064-10 | 4 |
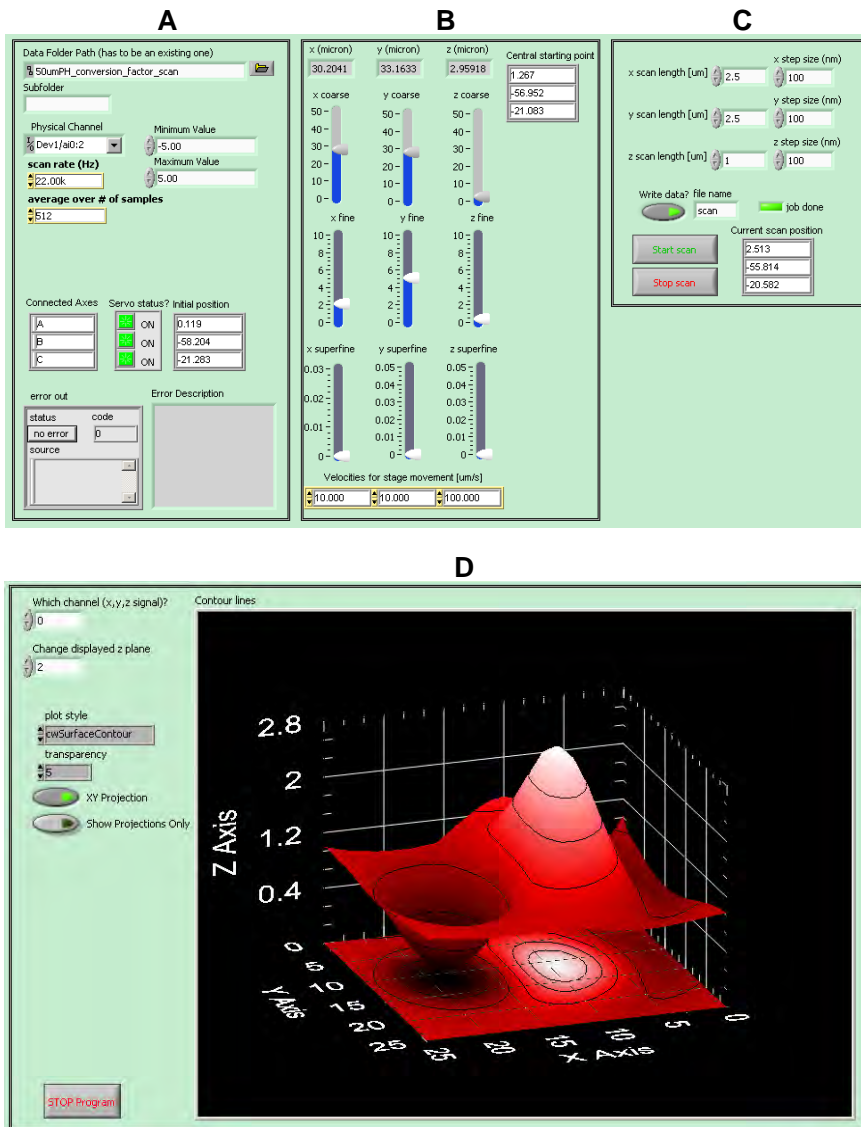
**Figure A.1.** – **Bead scanning experiments.** Screenshot of the Labview program that features four panels with the following content: (A) Control of data acquisition parameters. (B) Adjustment of zero-position to align the immobilized bead with the trap center. (C) Control of scanning volume and sampling density. (D) Preview window showing the measured conversion factor map.
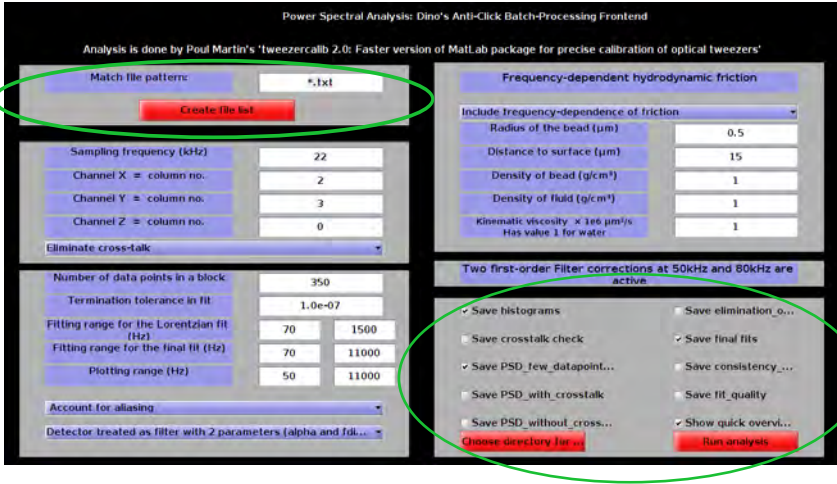
**Figure A.2.** – **Batch processing for power spectral analysis.** Graphical user interface with the modified input possibilities marked in green. At the top left, the 'read' directory and the 'file-search pattern' are defined. At the bottom right, it can be selected which plots should be calculated and saved.

in incremental steps in the XY-plane and subsequently in the z-direction, acquiring a 'stack' of two dimensional scans. A plot on the Labview front panel previews the obtained conversion factor map by a surface fit to the captured data points. The data is saved in a tab separated text file and send to Matlab for further analysis.

## A.0.3. Matlab program for batch processing of power spectral analysis

In the course of the project, I had to analyze several thousand bead trajectories using power spectral analysis. To get this task done more efficiently, I wrote a Matlab program for batch processing of the trap calibration analysis. The program provides a front-end for the trap calibration that is done by Poul Martin Bendix's power spectral analysis program [Hansen et al. 2006]. The graphical user interface is shown in Figure A.2. The user first choses a 'read' directory, i.e., where the data files that should be analyzed are located, and can additionally

define a 'file-search pattern', such that only files that match this pattern are included in the analysis. Next, one can select which kind of data and plots should be saved, and a 'write' directory has to be defined, i.e., the destination where the results should be saved. After these parameters are defined, all time series that match the file-search pattern are analyzed sequentially. The results are sorted into different sub-folders in the 'write' directory. Likewise, the results, e.g., the estimated corner frequency, and the experimental conditions as, e.g., the power of the trapping laser, get written into an Matlab array of the dataset class, making further statistical analysis easy.

# Publications

# Crosstalk elimination in the detection of dual-beam optical tweezers by spatial filtering

Dino Ott,[1] S. Nader S. Reihani,[2] and Lene B. Oddershede[1,a)]

[1]*Niels Bohr Institute (NBI), University of Copenhagen, Blegdamsvej 17, DK-2100 Copenhagen, Denmark*
[2]*Department of Physics, Sharif University of Technology, 11369-9161 Tehran, Iran*

In dual-beam optical tweezers, the accuracy of position and force measurements is often compromised by crosstalk between the two detected signals, this crosstalk leading to systematic and significant errors on the measured forces and distances. This is true both for dual-beam optical traps where the splitting of the two traps is done by polarization optics and for dual optical traps constructed by other methods, e.g., holographic tweezers. If the two traps are orthogonally polarized, most often crosstalk is minimized by inserting polarization optics in front of the detector; however, this method is not perfect because of the de-polarization of the trapping beam introduced by the required high numerical aperture optics. Here we present a simple and easy-to-implement method to efficiently eliminate crosstalk. The method is based on spatial filtering by simply inserting a pinhole at the correct position and is highly compatible with standard back focal plane photodiode based detection of position and force. Our spatial filtering method reduces crosstalk up to five times better than polarization filtering alone. The effectiveness is dependent on pinhole size and distance between the traps and is here quantified experimentally and reproduced by theoretical modeling. The method here proposed will improve the accuracy of force-distance measurements, e.g., of single molecules, performed by dual-beam optical traps and hence give much more scientific value for the experimental efforts. © *2014 AIP Publishing LLC*. [http://dx.doi.org/10.1063/1.4878261]

## I. INTRODUCTION

Dual-beam optical traps have been successfully used to investigate, e.g., the mechanical properties of DNA,[1,2] DNA protein association,[3] and the mechanical action of molecular motors.[4,5] For these subtle and technically advanced investigations, it is of utmost importance that as much information as possible is retrieved from the data and that data are as accurate as possible, i.e., without systematic errors. Dual optical traps can be constructed in different ways, e.g., by holographic means,[6] but the most common way is to insert a polarizing beam splitter in the path and hence create two traps with orthogonal polarizations from a single laser source. This is convenient as it is easy, low-cost, and facilitates independent control of the two individual traps.[7,8] Also, it is an advantage that the two traps come from a single laser source and hence have similar Poynting vector and power fluctuations.

In "single beam" optical traps, it is common and convenient to use the trapping laser beam also for detection of the positions visited by the trapped particle by detecting the forward and un-scattered light by a photodiode placed in the back focal plane. Through proper calibration, one can deduce the forces acting on the trapped particle.[9] Force- and distance-detection by photodiodes have significant advantages compared to camera based detection; the detection rates can be significantly higher, thus revealing very fast dynamics, and the acquisition and subsequent data analysis is significantly faster than image-based detection. A similar method is often applied to detect the position of trapped particles in dual

traps with orthogonal polarization. In this case, a polarizing beam splitter, or a polarization filter, is placed in front of the photodiode, thus, in principle, allowing only the signal from one trap to impinge on a particular photodiode. However, a complete separation purely based on polarization optics is not possible: First, polarization optics are not perfect; when using polarizing beam splitters the reflected beam often still contains 1% of the "wrong" polarization. Second and even more problematic, a partial depolarization of the trapping beams occurs due to the high numerical aperture (NA) optics required for obtaining three-dimensional trapping by a single laser beam.[10] This incomplete separation of the signals consequently leads to so-called crosstalk, a parasitic signal originating from the other trap when measuring one specific trap of interest. Depolarization due to high-NA optics, which can reach up to 10% of the integrated focal intensity,[11] should be taken seriously as it can represent a severe source of error[12] resulting in a deviation in the measured force magnitude of up to several pN.[10] The parasitic signal changes the voltage signal of a given quadrant or pixel and enters the differential signal used for lateral detection in a non-trivial and systematic manner. As the axial position is normally measured as the total power impinging on the photodiode, the axial positions and forces will be systematically overestimated. These errors are, of course, problematic both while measuring, e.g., physical properties of molecular motors[13] or weak hydrodynamic interactions between trapped particles.[14]

Since crosstalk presents a serious problem to acquisition, several means for signal separation have been presented. These include fast sequential detection of time-multiplexed optical traps,[15] polarization rectification by beam back propagation through the focusing objective,[10] and advanced

---
a)Author to whom correspondence should be addressed. Electronic mail: oddershede@nbi.dk

signal processing.[16] As a simple, low cost, and efficient alternative to the previously published techniques, we here present a method to perform crosstalk suppression by spatial filtering. The method simply consists of inserting a pinhole in a position that allows only the signal originating from the trap of interest to propagate to the photodiode detector. This new method reduces crosstalk to less than 0.2%, thus performing five times better than standard polarization filtering alone.

## II. PRESENTATION OF THE SPATIAL FILTERING METHOD

In typical interferometric detection schemes, the signal is imaged by a lens onto a plane conjugate to the back focal plane (BFP).[9] This is because space constraints typically do no allow placement of the photodiode directly at the BFP. Therefore, an intermediate plane exists, which is conjugate to the focal plane of the microscope objective, i.e., to the sample plane where the trapping is performed. The trapping beams overlap along most of the optical path. In this intermediate plane, however, the beams are well separated spatially, and filtering is done simply by inserting a pinhole here, as sketched in Figure 1. If the foci of the trapping beams are separated in the sample plane, they will also be separated in this conjugate plane. By accurately positioning the pinhole at the focus of the beam of interest (grey trap in Figure 1, from now on referred to as Trap 1), only this beam will be transmitted to the detection photodiode. The other beam (henceforth denoted Trap 2) will be efficiently obstructed, and crosstalk will be eliminated. The experimental setup is further detailed in Sec. IV.
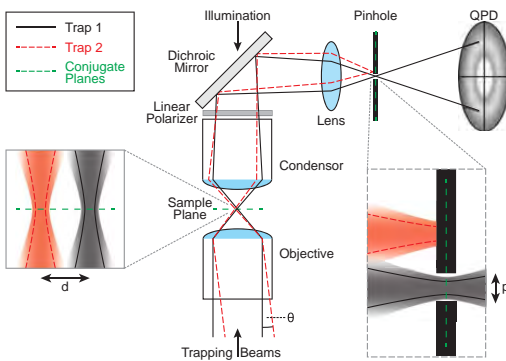


FIG. 1. Illustration of the spatial filtering method. Two independent traps are created in the sample plane by two trapping beams in orthogonal polarization states. Trap 2 enters the objective at an angle $\theta$, which translates to a lateral distance $d$ between the foci. The transmitted light is collected by the microscope condenser. A lens images the back focal plane of the condenser onto a quadrant photodiode for detection of the position of the trapped particle. Blocking the laser beam of Trap 2 by a pinhole with diameter p, located in a plane conjugate to the sample plane, allows for the transmission of Trap 1 to the detector and effectively suppresses crosstalk from Trap 2. Optionally, crosstalk can be further minimized by adding a linear polarizer in front of the QPD.

## III. RESULTS

### A. Influence of spatial filtering on optical trapping and detection

To ensure that the proposed crosstalk elimination method does not influence the optical trapping and position detection capabilities, a full analysis of the trap characteristics was conducted for a single-beam optical trap with the pinhole installed. For each translational direction, there exists a conversion factor, which allows for conversion from the arbitrary voltage readout from the quadrant photodiode (QPD) to absolute lengths. The exact definition and calculation of the conversion factor is detailed in Sec. IV. It is of great convenience in photodiode-based detection of optically trapped objects if this conversion factor is constant across the interval of data acquisition. To check for this, an experiment was performed where a bead, immobilized on a glass surface, was scanned by a piezo stage through the focus in three dimensions. The relation between the voltage readout from the QPD and the actual position in one of the lateral directions, $y$, is shown in Figure 2(a). Clearly, there is a large linear range, signifying a constant conversion factor. This was true for all three translational directions. The $y$-conversion factor should be relatively constant upon small variations in $x$, and Figure 2(b) confirms that this is indeed the case.

For small particle excursions, an optical trap based on a Gaussian intensity profile exerts an approximately harmonic force, $F = -\kappa x$, on the trapped particle, where $\kappa$ denotes the trap stiffness and $x$ is the deviation from the equilibrium position. As detailed in Sec. IV, the dynamics of the trapped particle obeys the Langevin equation, and the power spectrum of the time series is well fitted by a Lorentzian function, from which the so-called corner frequency, $f_c$ $= \kappa/2\pi\gamma$, can be found. Here, $\gamma$ denotes the friction coefficient of the bead in the solution, which can be estimated from Stokes' law if far from any surfaces. To ensure that the spatially filtered Trap 1 retained the "normal" trapping behavior, time series of the positions visited by a bead in Trap 1 were analyzed while Trap 2 was blocked before entering the microscope. The inset of Figure 2(c) shows that the position histogram is well fitted by a Gaussian distribution, hence, the spatially filtered Trap 1 still exerts a harmonic force. Also, experiments with and without the pinhole installed in the optical path were done, to ensure that the insertion of the pinhole leaves the measured corner frequency of Trap 1 unaltered. The result is shown in Figure 2(c), where the two data sets are artificially displaced from each other in the vertical direction. Within the error bars (one standard deviation), $f_c$, and hence also $\kappa$, are unaffected by the presence of the pinhole.

### B. Quantification of crosstalk suppression

As a measure of crosstalk, we use the quantity

$$\Psi = \frac{S_{\text{parasitic}}}{S_{\text{total}}}, \tag{1}$$

where the signals $S_{\text{parasitic}}$ and $S_{\text{total}}$ denote the parasitic signal and the total signal, respectively. In practice, $S_{\text{parasitic}}$ was measured as the signal that penetrated the pinhole (aligned at Trap
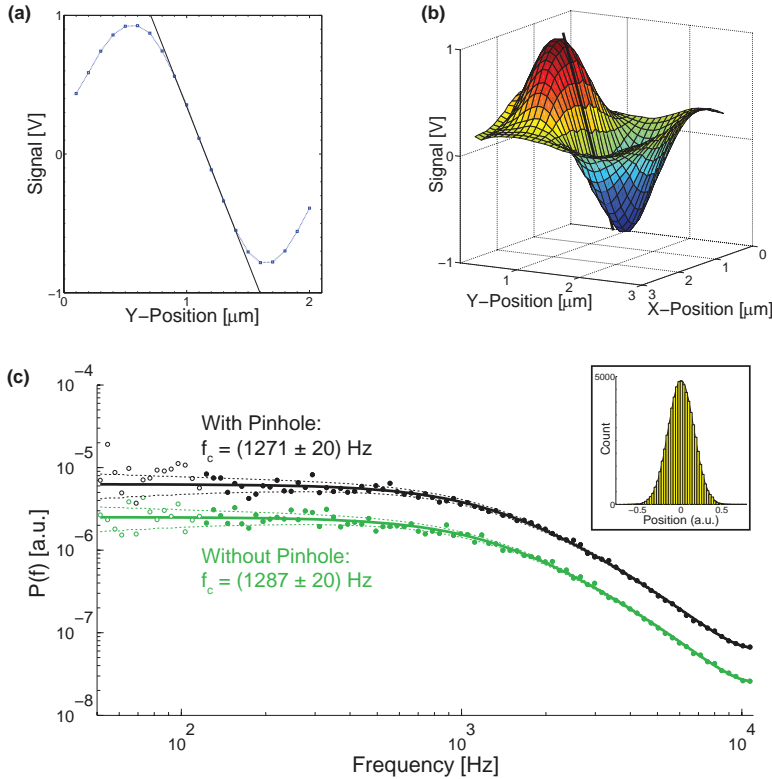
FIG. 2. Influence of pinhole insertion on optical trapping in Trap 1 and photodiode based detection. (a) The raw y-voltage signal from the photodiode as a function of lateral motion of the bead within the trap. The linear region verifies a substantial region with a constant conversion factor. (b) The raw y-signal from the photodiode as a function of movement in both lateral directions. The y-signal shows a linear dependence on the bead's y-displacement from its equilibrium position and only a minor dependency on its displacement along the x-axis. The full line corresponds to graph A. (c) Comparison of power spectra of the time series originating from Trap 1 with and without the pinhole inserted. For visibility, the two plots have been arbitrarily displaced in the vertical direction. The solid line denotes a fit to thedata utilizing a Lorentzian function, as detailed in Sec. IV, using the program from Ref. 17. The dotted lines indicate the ±1 standard deviation expected from theory, filled dots mark data included in the fit, open circles indicate data outside the fitting range. Inset: Histogram of the positions visited by the trapped particle, full line is a Gaussian fit.

1) while Trap 1 was off and Trap 2 was on. Similarly, $S_{total}$ was measured as the signal that penetrated the pinhole while both Trap 1 and Trap 2 were on. In other words, this measure of crosstalk quantifies the contribution of the parasitic signal from Trap 2 to the total measured signal in a dual-trap experiment where both traps are on and where the aim is to measure exclusively the signal originating from Trap 1. The signals were recorded while varying the distance $d$ between the traps. This was done by keeping Trap 1 at a constant position in the center of the field of view (FOV), co-centering the pinhole with Trap 1 for maximum transmission, and subsequently stepwise moving the focus of Trap 2 to the distance $d$. The signal measured is the total intensity reaching the QPD, $I_{QPD} = I_1 + I_2 + I_3 + I_4$, which is the sum of the intensities, $I_i, i = \{1, 2, 3, 4\}$, detected by each of the four individual quadrants.

We investigated the influence of the trap separation $d$ on crosstalk for a range of pinhole diameters, $p = 5 \mu m$,

10 $\mu$m, 20 $\mu$m, 30 $\mu$m, 50 $\mu$m, 100 $\mu$m, and 150 $\mu$m. The result is plotted in Figure 3(a), which shows crosstalk ($\Psi$) as a function of distance between the traps, $d$, for different pinhole diameters. As expected, a maximal crosstalk of 50 % is obtained when the beams overlap perfectly ($d = 0$), as both beams pass through the pinhole and Trap 2 contributes with 50% to the total signal. With increasing $d$ the crosstalk, $\Psi$, decreases (Fig. 3(a)) and goes towards zero for large $d$. The smaller the pinhole diameter, the more rapid and effective is the crosstalk suppression. To quantify the crosstalk suppression for varying pinhole sizes, we compared the distances $\Gamma$, where the crosstalk $\Psi$ had fallen by 3dB, i.e., by 50%, relative to its maximum value at $d = 0$. Figure 3(b) shows $\Gamma$ as a function of $p$ and indicates a linear relation between $\Gamma$ and the pinhole diameter for diameters larger than 20 $\mu$m. This linear relation can be used to choose the optimal pinhole size for a certain experimental design. At $p \leq 10 \mu$m, an oscillatory behavior of $\Psi(d)$ is observed. This probably originates from
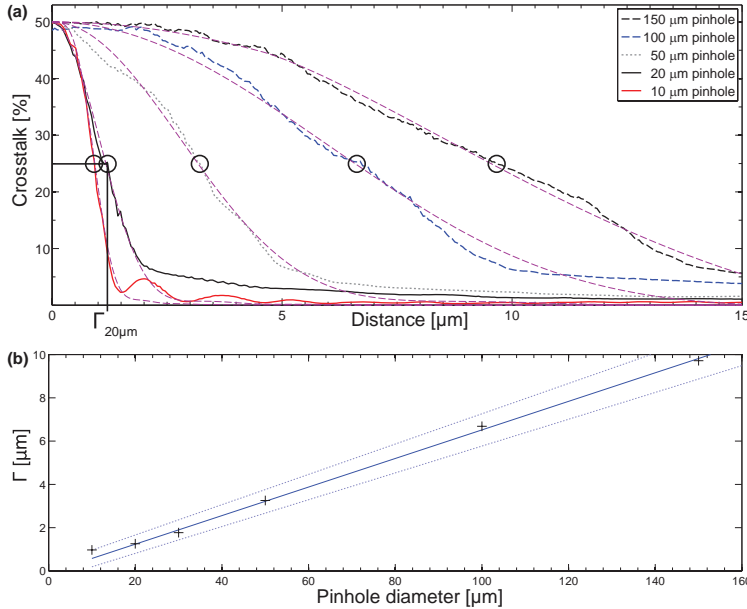
FIG. 3.   Crosstalk suppression by spatial filtering. (a) Crosstalk $\Psi$ as a function of distance $d$ for varying pinhole size. All curves are raw data, no smoothing filter was applied. The dashed purple lines are theoretical fits to the experimental data. The 3dB decrease distance, $\Gamma$, is shown as a black ring for each pinhole size and explicitly marked for $p = 20$ $\mu$m. (b) 3dB decrease distance, $\Gamma$, as a function of pinhole diameter, $p$. The full line shows a linear fit to the data points from $p = 20$ $\mu$m to 150 $\mu$m, the dotted lines denote the 95%-confidence area of the fit. The data point of the 10 $\mu$m pinhole is located just outside the 95%-confidence area, indicating that for this small pinhole the linear relation does not hold.

diffraction effects and sets a lower limit for the usable pinhole size.

## C. Theoretical prediction of crosstalk suppression by spatial filtering

To support the experimental findings, we theoretically modeled the crosstalk suppression by spatial filtering. We modeled the spatial filtering process using a wave optics approach. The optical system was simplified by modeling the lens compounds of both the objective and the condenser as single lenses. The expanded Gaussian-shaped trapping beam entering the objective lens is focused down to a diffraction limited spot. The shape of this focal spot is influenced by the overfilling ratio, i.e., the ratio between the $\frac{1}{e^2}$-beam diameter and the front aperture of the objective. When the $\frac{1}{e^2}$-beam diameter matches the aperture diameter, the focal spot is approximately Gaussian-shaped with side lobes of very low intensity. With larger overfilling ratios, the incident intensity profile becomes more uniform and the side lobes in the focal intensity distribution become more pronounced. In other words, the intensity distribution becomes more Airy disk-like, as this is the interference pattern caused by Fraunhofer diffraction of a plane wave with a flat intensity profile at a circular aperture.[18]

The focal spot in the sample plane is magnified and imaged into the pinhole plane. This transformation is dictated by

the point spread function of the imaging optics, resulting in an intensity distribution resembling that of an Airy disk, which mathematically can be described as

$$\mathcal{I}(r) = \mathcal{I}_0 \left( \frac{2\,J_1(x)}{x} \right)^2, \qquad (2)$$

with the peak intensity $\mathcal{I}_0$ and $J_1(x)$ denoting the Bessel function of the first kind of order one, where $x$ contains both geometrical and optical parameters, i.e., $x = (2\pi/\lambda)ar$, with $a$ being the radius of the circular condenser aperture, $\lambda$ the wavelength, and $r$ the radial distance from the optical axis measured in the plane of the diffraction pattern.[19]

Now, the ($d$ dependent) transmission of the parasitic signal, $\Psi_{\text{theory}}$, can be estimated by computing the 2D-convolution

$$\Psi_{\text{theory}} = \mathcal{I}(r) \star g(r) \qquad (3)$$

of the diffraction pattern $\mathcal{I}(r)$ and a two-dimensional circular boxcar function $g(r)$, defined by $g(r < p/2) = 1$ and $g(r > p/2) = 0$, representing the pinhole, which is located in this plane. Two-parameter fits, accounting for the shape of the Airy disk and the pinhole diameter, to the experimentally measured curves are shown in Figure 3(a) (purple dashed lines). The crosstalk, as a function of trap separation distance, is well described by the model; in particular, the initial flat region and the decrease fit quite well. However, the model underestimates the tails of the distribution. This is probably
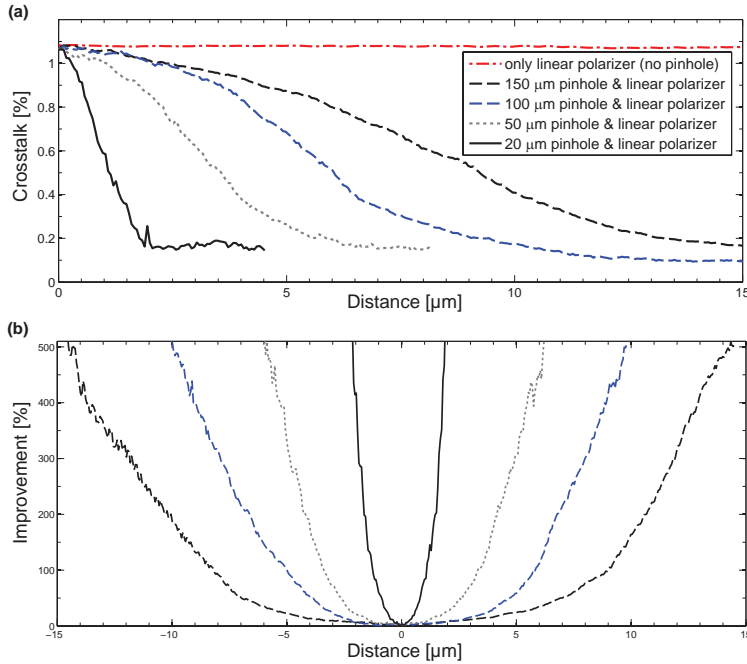
FIG. 4. Combining spatial and polarization filtering for efficient crosstalk suppression. (a) Crosstalk as a function of trap separation distance, $d$. If only the polarization filtering is performed (dot-dash red line), the crosstalk level is independent of $d$. Adding also the spatial filtering improves the crosstalk suppression down to a level of 0.2 percent for sufficient trap separation. (b) Crosstalk suppression improvement, $\Omega$, by employing both spatial and polarization filtering compared to employing polarization filtering alone. The improvement was calculated for the data shown in (a) and the legends are the same.

because in the experiments there are inherent aberrations that are not included in the theory and which give rise to more pronounced side lobes.

## D. Crosstalk suppression by combining spatial and polarization filtering

The most common way to suppress crosstalk in dual-beam orthogonally polarized optical traps is by inserting polarization optics in front of the photodiode detector and the minimal crosstalk for a well aligned, purely polarization-based filtering is on the order of 1 to 1.5%.[11] The efficiency of polarization filtering alone is comparable to that of spatial filtering alone. To obtain an exceptionally high degree of crosstalk suppression, the two methods should be combined, which is straightforward in practice. Here we quantify the crosstalk suppression by such a combination of spatial and polarization filtering. For the experimental measurements of combining spatial and polarization filtering a linear polarizer (extinction ratio $>1 : 10^7$, Thorlabs LPNIR100) was placed in the BFP of the condenser (see Fig. 1).

In accordance with Ref. 11, we obtained a crosstalk level of 1.1% when employing only a linear polarizer and no pinhole for filtering (dot-dashed red line in Figure 4(a)). As expected, this value did not depend on the distance $d$ separating the traps. After inserting the pinhole, the crosstalk decreased with increasing trap separation, $d$, dropping to a value significantly below the level achievable with the polarization optics alone (Fig. 4(a)). Combining spatial filtering with polarization filtering provides crosstalk levels below 0.2% for sufficient trap separation $d$. Notably, at this very low level of crosstalk, we are limited by electronics noise, not by the pinhole method.

To compare the crosstalk while performing only linear polarization filtering ($\Psi_{LP}$) to the crosstalk while performing both pinhole based spatial filtering and linear polarization filtering ($\Psi_{PH\&LP}$), we calculated the improvement, $\Omega$:

$$\Omega = \frac{\Psi_{LP} - \Psi_{PH\ and\ LP}}{\Psi_{PH\ and\ LP}}, \qquad (4)$$

as a function of trap separation distance $d$. The result is plotted in Figure 4(b), which shows that the advantage of employing also the spatial filtering increases as the trap separation distance increases. Also, it shows that at trap separations of more than 2 $\mu$m, the crosstalk can be reduced by a factor five by spatial filtering with correct pinhole size.

## IV. METHODS

### A. Optics

The experiments were carried out on a modified inverted microscope (Leica DM IRBE), into which dual-beam

optical tweezers were implemented. The two optical traps, of equal power, were created by splitting a laser beam (1064 nm CW Nd:YVO$_4$ laser, Spectra Physics J20I-BL-106C-02) into two separate beams, by means of a half-wave-plate followed by a polarizing beam splitter. In the optical path of Trap 2, there was a 1:1-telescope allowing for steering Trap 2: the first lens of the telescope, the "beam steering lens," was imaged onto the BFP of the objective by the second telescope lens. A LabView-controlled, piezo-actuated linear translation stage (Newport Picomotor, 9066-X-P-M) allowed for precise lateral displacement of this beam steering lens, thus causing a change in the angle of incidence $\theta$ into the objective, which then led to a lateral displacement of Trap 2 in the focal plane.[8] Besides allowing for position control, this layout guaranteed minimal clipping of the beam by the objective entrance aperture when translating the optical trap. The two expanded Gaussian-shaped laser beams with orthogonal polarization states were focused by a high-NA water immersion objective (63X, NA=1.2, Leica HCX PL APO W CORR CS), thus creating the optical trap. An oil immersion condenser (NA = 1.4, Leica S1 551004) collected the transmitted light, whose back focal plane was imaged onto a QPD (Si-PIN photodiode, Hamamatsu S5981).

The sample chamber was made by sandwiching two #1.5 glass cover slips on top of each other using double-sided sticky tape, to form a water-filled perfusion chamber, approximately 80 $\mu$m in thickness. All trapping experiments were performed far from any surfaces. The mean diameter of the particles was 0.96 $\mu$m (PS03N/9396, Bangs Laboratories).

### B. Alignment of pinhole

The pinhole was mounted on actuators with differential drives (Thorlabs ST1XY-D) that allowed for precise three-dimensional translation. An initial coarse positioning of the pinhole, in the plane conjugate to the focal plane, was followed by an iterative positioning process, in which the position was fine-adjusted to maximize the transmitted intensity. The correct alignment of the pinhole with the trap of interest, i.e., Trap 1, could be verified by monitoring the signal while switching Trap 1 on and off or while scanning Trap 2 through the field of view.

### C. Calibration

To deduce forces and distances from optical trapping, it is a necessity to perform a calibration. We calibrated the trap through monitoring the thermal fluctuations of the particle within the trap.[9] The bead fluctuates in the harmonic potential of the optical trap, and its dynamics is well described by the Langevin equation

$$m\ddot{x}(t) + \gamma\dot{x}(t) + \kappa x(t) = F_{\text{therm}}(t), \qquad (5)$$

with $x$ being the time-dependent position of the bead, $m$ the bead's mass, $\gamma$ the friction coefficient given by Stokes' law: $\gamma = 3\pi\eta d$ ($d$ being the diameter of the particle and $\eta$ the viscosity) if far from any surfaces, and $\kappa$ the spring constant characterizing the optical trapping potential. $F_{\text{therm}}(t)$ is a ran-

dom and time-dependent force due to stochastic thermal collisions with the solvent. As the trapping is conducted in water, inertia is negligible compared to any of the other terms and the inertial term, $m\ddot{x}(t)$, can safely be neglected.

The position of the bead in the trap was measured by a quadrant photodiode (QPD). The QDP has four photodiodes arranged as quadrants: the difference signals provide the lateral positions of the bead, and the sum of all four signals is proportional to the axial movement of the bead.[23] The raw output from the QPD ($S(t)$) is in volts and needs to be converted into metric units for absolute distance determination ($x(t)$). In a certain range, $S(t)$ and $x(t)$ are linearly proportional and a conversion factor, $\beta$, can be determined:

$$x(t) = \beta S(t). \qquad (6)$$

The power spectrum of the voltage signal, $S(t)$, obtained in a measurement with finite measurement time $T$, can be found as

$$P_{\text{exp}}(f) = |\tilde{S}(f)|^2 / T. \qquad (7)$$

Here, $\tilde{S}(f)$ denotes the Fourier transform of the signal $S(t)$

$$\tilde{S}(f) = \int_{-T/2}^{T/2} S(t)e^{i2\pi ft}dt. \qquad (8)$$

Using Eq. (6), the power spectrum of the experimental data can be written as

$$P_{\text{exp}}(f) = \left|\tilde{S}(f)\right|^2 / T = \frac{1}{\beta^2}|\tilde{x}(f)|^2 / T. \qquad (9)$$

The theoretical power spectrum of the Langevin equation, $P(f)$, is the expectation value of the experimental power spectrum:

$$P(f) = \langle P_{\text{exp}}(f)\rangle = \frac{A}{f_c^2 + f^2}, \qquad (10)$$

where $f_c$ is the so-called corner frequency, $f_c = \kappa/2\pi\gamma$, and $A = \frac{D}{2\pi^2\beta^2}$, with $D$ being the diffusion constant of the bead. D is connected to $\gamma$ via the Einstein equation

$$D = \frac{k_B T}{\gamma}, \qquad (11)$$

where $T$ is the absolute temperature and $k_B$ the Boltzmann constant. A different numerical factor can appear in the equation for $A$, depending on whether one considers the one-sided or the two-sided power spectral density in the analysis. The above stated formula for $A$ is for the two-sided PSD.

The corner frequency $f_c$ and the conversion factor $\beta$ can now be determined by fitting the theoretically expected PSD to the experimental data regarding $A$ and $f_c$ as the fitting parameters. In the simplest case of calibrating an optical trap, this would mean a simple Lorentzian fit. However, in practice the photodiode has a pronounced filtering effect[24] that needs to be taken into account in the fitting procedure. We used the program from Ref. 17, which takes this filtering effect as well as aliasing and other minor effects into account. Finally, $\kappa$ can be extracted from $f_c$ (as $f_c = \kappa/2\pi\gamma$) which concludes the calibration.
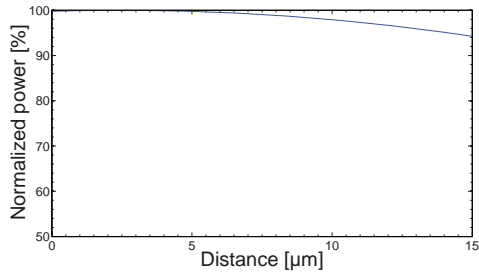
FIG. 5. Calibration curve quantifying the change of power of Trap 2 as a function of distance between Trap 1 and Trap 2. Not taking this power loss into account would lead to an underestimation of the crosstalk.

### D. Data analysis

Time series of 3 s of the positions visited by the bead in the trap were recorded at 22 kHz and used for calibration. Based on Allan variance analysis, this is the optimal length and acquisition frequency for the current setup.[25] Low frequency mechanical vibrations of the pinhole were omitted by excluding low frequency components below 120 Hz in the fit. Prior to the crosstalk analysis, we subtracted the QPD dark current from the measured integral QPD signal. This was measured prior to each experiment for the chosen analog preamplification of the QPD voltage signal. Also, we compensated for the slight power loss (less than 5%) that occurs when Trap 2 is moved away from the center of the field of view. This power loss is caused by the fact that the BFP of the objective does not coincide with the objective shoulder but is actually located inside the objective (17.50 mm), thus leading to a marginal cutting of the impinging beam when being tilted to move the trap laterally in the focal plane. Disregarding this effect would result in an underestimation of the crosstalk when moving towards to the margins of the field of view. To determine this power loss, we measured the transmitted power as a function of the position of Trap 2. The resulting calibration curve is shown in Figure 5.

### V. CONCLUSION

Crosstalk elimination is critical for high precision measurements involving the detection of several laser beams, as it gives rise to the detection of a parasitic signal that adds a systematic error to the readout and hence compromises the accuracy of experiments. This is of specific interest for dual-beam optical traps, were the forces and distances of a trapped object are read off using photodiode detectors. We present a method based on spatial filtering for efficient elimination of crosstalk. The method simply consists of inserting a pinhole in a plane conjugate to the focal plane. This spatial filtering does not alter the forces and distances measured from a single trap, and the linear range between displacement and readout from the photodiode detector is preserved. Both direct experimental measurements and theoretical modeling confirmed that the spatial filtering effec-

tively minimizes crosstalk; the larger the trap-trap distance, the larger the suppression. We provide tools for selecting the proper pinhole size for a certain acceptable crosstalk level. If the two traps have orthogonal linear polarization, spatial filtering alone is approximately as efficient as polarization filtering, which is commonly used. However, if the two methods are combined, which in practice is very easy, then the crosstalk is extremely efficiently suppressed; in fact, the combined method gives a factor five improvement compared to the standard linear polarization filtering alone. The spatial filtering technique can readily be adapted to other implementations of optical traps than just dual-beam optical traps. In principle, the method can easily be extended to detect the signal from any spatially separated arrangement of multiple optical traps, for instance holographic optical tweezers (HOTs).[6,20] Normally, the detection of forces and displacement of objects in multiple optical traps is done by means of a camera, because it has been difficult to separate the signals from the multiple laser beams using photodiodes. With this spatial filtering, it should be possible to separate the signal from each trap and detect it individually with a photodiode, which has distinct advantages over camera detection, e.g., higher temporal and spatial resolution[21,22] as well as easier data analysis. Hence, we believe the presented signal filtering scheme will prove quite useful for future more accurate optical tweezers experiments.

[1]P. Gross, N. Laurens, L. B. Oddershede, U. Bockelmann, E. J. G. Peterman, and G. J. L. Wuite, Nat. Phys. **7**, 731 (2011).
[2]I. Heller, G. Sitters, O. D. Broekmans, G. Farge, C. Menges, W. Wende, S. W. Hell, E. J. G. Peterman, and G. J. L. Wuite, Nat. Methods **10**, 910 (2013).
[3]J. Sung, S. Sivaramakrishnan, A. R. Dunn, and J. A. Spudich, *Methods in Enzymology*, 1st ed. (Elsevier Inc., 2010), Vol. 475, pp. 321–75.
[4]J. T. Finer, R. M. Simmons, and J. A. Spudich, Nature (London) **368**, 113 (1994).
[5]J. Zhou, V. Schweikhard, and S. M. Block, Biochim. Biophys. Acta **1829**, 29 (2013).
[6]J. E. Curtis, B. A. Koss, and D. G. Grier, Opt. Commun. **207**, 169 (2002).
[7]K. Visscher, S. P. Gross, and S. M. Block, IEEE J. Sel. Top. Quantum Electron. **2**, 1066 (1996).
[8]K. C. Neuman and S. M. Block, Rev. Sci. Instrum. **75**, 2787 (2004).
[9]F. Gittes and C. F. Schmidt, Opt. Lett. **23**, 7 (1998).
[10]P. Mangeol and U. Bockelmann, Rev. Sci. Instrum. **79**, 083103 (2008).
[11]M. Atakhorrami, K. M. Addas, and C. F. Schmidt, Rev. Sci. Instrum. **79**, 043103 (2008).
[12]K. Bahlmann and S. W. Hell, Appl. Phys. Lett. **77**, 612 (2000).
[13]J. R. Moffitt, Y. R. Chemla, D. Izhaky, and C. Bustamante, Proc. Natl. Acad. Sci. U.S.A. **103**, 9006 (2006).
[14]J.-C. Meiners and S. R. Quake, Phys. Rev. Lett. **82**, 2211 (1999).
[15]D. Ruh, B. Tränkle, and A. Rohrbach, Opt. Express **19**, 21627 (2011).
[16]Y. von Hansen, A. Mehlich, B. Pelz, M. Rief, and R. R. Netz, Rev. Sci. Instrum. **83**, 095116 (2012).
[17]P. M. Hansen, I. M. Tolić-Nørrelykke, H. Flyvbjerg, and K. Berg-Sørensen, Comput. Phys. Commun. **174**, 518 (2006).

[18] V. N. Mahajan, J. Opt. Soc. Am. A **3**, 470 (1986).

[19] M. Born and E. Wolf, *Principles of Optics: Electromagnetic Theory of Propagation, Interference and Diffraction of Light* (Cambridge University Press, Cambridge, 1999).

[20] K. Dholakia and T. Čižmár, Nat. Photon. **5**, 335 (2011).

[21] S. Keen, J. Leach, G. Gibson, and M. J. Padgett, J. Opt. A: Pure Appl. Opt. **9**, S264 (2007).

[22] C. Pacoret and S. Régnier, Rev. Sci. Instrum. **84**, 081301 (2013).

[23] A. Pralle, M. Prummer, E.-L. Florin, E. H. K. Stelzer, and J. K. H. Hörber, Microsc. Res. Tech. **44**, 378 (1999).

[24] K. Berg-Sørensen, L. Oddershede, E.-L. Florin, and H. Flyvbjerg, J. Appl. Phys. **93**, 3167 (2003).

[25] F. Czerwinski, A. C. Richardson, and L. B. Oddershede, Opt. Express **17**, 13255 (2009).

# Simultaneous three-dimensional tracking of individual signals from multi-trap optical tweezers using fast and accurate photodiode detection

**Dino Ott,[1] S. Nader S. Reihani,[1,2] and Lene B. Oddershede[1,*]**

[1]*Niels Bohr Institute (NBI), University of Copenhagen, Blegdamsvej 17, DK-2100 Copenhagen, Denmark*
[2]*Physics Department, Sharif University of Technology, 11365-9161 Tehran, Iran*
[*]*oddershede@nbi.dk*

**Abstract:** Multiple-beam optical traps facilitate advanced trapping geometries and exciting discoveries. However, the increased manipulation capabilities come at the price of more challenging position and force detection. Due to unrivaled bandwidth and resolution, photodiode based detection is preferred over camera based detection in most single/dual-beam optical traps assays. However, it has not been trivial to implement photodiode based detection for multiple-beam optical traps. Here, we present a simple and efficient method based on spatial filtering for parallel photodiode detection of multiple traps. The technique enables fast and accurate 3D force and distance detection of multiple objects simultaneously manipulated by multiple-beam optical tweezers.

---

### References and links

1. R. T. Dame, M. C. Noom, and G. J. L. Wuite, "Bacterial chromatin organization by H-NS protein unravelled using dual DNA manipulation," Nature **444**, 387–390 (2006).
2. M. Noom, B. V. D. Broek, J. van Mameren, and G. J. L. Wuite, "Visualizing single DNA-bound proteins using DNA as a scanning probe," Nat. Methods **4**, 1031–1036 (2007).
3. H. Kress, J.-G. Park, C. O. Mejean, J. D. Forster, J. Park, S. S. Walse, Y. Zhang, D. Wu, O. D. Weiner, T. M. Fahmy, and E. R. Dufresne, "Cell stimulation with optically manipulated microsources," Nat. Methods **6**, 905–909 (2009).
4. M. Polin, D. Grier, and S. Quake, "Anomalous vibrational dispersion in holographically trapped colloidal arrays," Phys. Rev. Lett. **96**, 088101 (2006).
5. M. Padgett and R. Di Leonardo, "Holographic optical tweezers and their relevance to lab on chip devices," Lab Chip **11**, 1196–1205 (2011).
6. T. Čižmár, M. Mazilu, and K. Dholakia, "In situ wavefront correction and its application to micromanipulation," Nature Photon. **4**, 388–394 (2010).
7. J. Liesener, M. Reicherter, T. Haist, and H. J. Tiziani, "Multi-functional optical tweezers using computer-generated holograms," Opt. Commun. **185**, 77–82 (2000).
8. E. R. Dufresne, G. C. Spalding, M. T. Dearing, S. A. Sheets, and D. G. Grier, "Computer-generated holographic optical tweezer arrays," Rev. Sci. Instrum. **72**, 1810 (2001).
9. J. Curtis, B. Koss, and D. Grier, "Dynamic holographic optical tweezers," Opt. Commun. **207**, 169–175 (2002).
10. C. Schmitz, J. Spatz, and J. Curtis, "High-precision steering of multiple holographic optical traps," Opt. Express **13**, 8678–8685 (2005).

---

11. K. C. Neuman and S. M. Block, "Optical trapping," Rev. Sci. Instrum. **75**, 2787–2809 (2004).
12. K. Visscher, S. Gross, and S. Block, "Construction of multiple-beam optical traps with nanometer-resolution position sensing," IEEE J. Sel. Top. Quant. Electron. **2**, 1066–1076 (1996).
13. F. Gittes and C. F. Schmidt, "Interference model for back-focal-plane displacement detection in optical tweezers," Opt. Lett. **23**, 7–9 (1998).
14. A. Pralle, M. Prummer, E. L. Florin, E. H. Stelzer, and J. K. Hörber, "Three-dimensional high-resolution particle tracking for optical tweezers by forward scattered light," Microsc. Res. Tech. **44**, 378–386 (1999).
15. S. Keen, J. Leach, G. Gibson, and M. J. Padgett, "Comparison of a high-speed camera and a quadrant detector for measuring displacements in optical tweezers," J. Opt. A: Pure Appl. Opt. **9**, 264–266 (2007).
16. J. R. Moffitt, Y. R. Chemla, S. B. Smith, and C. Bustamante, "Recent advances in optical tweezers," Annu. Rev. Biochem. **77**, 205–228 (2008).
17. C. Pacoret and S. Régnier, "Invited article: a review of haptic optical tweezers for an interactive microworld exploration," Rev. Sci. Instrum. **84**, 081301 (2013).
18. R. Bowman, G. Gibson, and M. Padgett, "Particle tracking stereomicroscopy in optical tweezers: control of trap shape," Opt. Express **18**, 11785–11790 (2010).
19. R. F. Hay, G. M. Gibson, M. P. Lee, M. J. Padgett, and D. B. Phillips, "Four-directional stereo-microscopy for 3D particle tracking with real-time error evaluation," Opt. Express **22**, 18662–18667 (2014).
20. D. B. Conkey, R. P. Trivedi, S. R. P. Pavani, I. I. Smalyukh, and R. Piestun, "Three-dimensional parallel particle manipulation and tracking by integrating holographic optical tweezers and engineered point spread functions," Opt. Express **19**, 3835–3842 (2011).
21. S. Lee, Y. Roichman, G. Yi, S.-H. Kim, S.-M. Yang, A. van Blaaderen, P. van Oostrum, and D. G. Grier, "Characterizing and tracking single colloidal particles with video holographic microscopy," Opt. Express **15**, 18275–18282 (2007).
22. F. Cheong, B. Sun, R. Dreyfus, J. Amato-Grill, K. Xiao, L. Dixon, and D. G. Grier, "Flow visualization and flow cytometry with holographic video microscopy," Opt. Express **17**, 13071–13079 (2009).
23. F. Cheong, B. Krishnatreya, and D. Grier, "Strategies for three-dimensional particle tracking with holographic video microscopy," Opt. Express **18**, 13563–13573 (2010).
24. L. Miccio, P. Memmolo, F. Merola, S. Fusco, V. Embrione, A. Paciello, M. Ventre, P. A. Netti, and P. Ferraro, "Particle tracking by full-field complex wavefront subtraction in digital holography microscopy," Lab Chip **14**, 1129–1134 (2014).
25. R. Di Leonardo, S. Keen, J. Leach, C. Saunter, G. Love, G. Ruocco, and M. Padgett, "Eigenmodes of a hydrodynamically coupled micron-size multiple-particle ring," Phys. Rev. E **76**, 061402 (2007).
26. G. M. Gibson, J. Leach, S. Keen, A. J. Wright, and M. J. Padgett, "Measuring the accuracy of particle position and force in optical tweezers using high-speed video microscopy," Opt. Express **16**, 14561–14570 (2008).
27. M. Towrie, S. W. Botchway, A. Clark, E. Freeman, R. Halsall, A. W. Parker, M. Prydderch, R. Turchetta, A. D. Ward, and M. R. Pollard, "Dynamic position and force measurement for multiple optically trapped particles using a high-speed active pixel sensor," Rev. Sci. Instrum. **80**, 103704 (2009).
28. O. Otto, F. Czerwinski, J. L. Gornall, G. Stober, L. B. Oddershede, R. Seidel, and U. F. Keyser, "Real-time particle tracking at 10,000 fps using optical fiber illumination," Opt. Express **18**, 22722–22733 (2010).
29. R. Huang, I. Chavez, K. M. Taute, B. Lukić, S. Jeney, M. G. Raizen, and E.-L. Florin, "Direct observation of the full transition from ballistic to diffusive Brownian motion in a liquid," Nature Phys. **7**, 576–580 (2011).
30. F. Marsà, A. Farré, E. Martín-Badosa, and M. Montes-Usategui, "Holographic optical tweezers combined with back-focal-plane displacement detection," Opt. Express **21**, 30282–30294 (2013).
31. W. H. Guilford, J. A. Tournas, D. Dascalu, and D. S. Watson, "Creating multiple time-shared laser traps with simultaneous displacement detection using digital signal processing hardware," Anal. Biochem. **326**, 153–166 (2004).
32. D. Ruh, B. Tränkle, and A. Rohrbach, "Fast parallel interferometric 3D tracking of numerous optically trapped particles and their hydrodynamic interaction," Opt. Express **19**, 21627–21642 (2011).
33. D. Ott, S. N. S. Reihani, L. B. Oddershede, "Crosstalk elimination in the detection of dual-beam optical tweezers by spatial filtering," Rev. Sci. Instrum. **85**, 053108 (2014).
34. E. R. Dufresne and D. G. Grier, "Optical tweezer arrays and optical substrates created with diffractive optics," Rev. Sci. Instrum. **69**, 1974 (1998).
35. P. M. Hansen, I. M. Tolić-Nørrelykke, H. Flyvbjerg, and K. Berg-Sørensen, "tweezercalib 2.0: faster version of MatLab package for precise calibration of optical tweezers," Comput. Phys. Commun. **174**, 518–520 (2006).
36. K. Berg-Sørensen, L. Oddershede, E.-L. Florin, and H. Flyvbjerg, "Unintended filtering in a typical photodiode detection system for optical tweezers," J. Appl. Phys. **93**, 3167 (2003).
37. A. Rohrbach, "Stiffness of optical traps: quantitative agreement between experiment and electromagnetic theory," Phys. Rev. Lett. **95**, 168102 (2005).
38. W. M. Lee, P. J. Reece, R. F. Marchington, N. K. Metzger, and K. Dholakia, "Construction and calibration of an optical trap on a fluorescence optical microscope," Nat. Protoc. **2**, 3226–3238 (2007).
39. J. K. Dreyer, K. Berg-Sørensen, and L. Oddershede, "Improved axial position detection in optical tweezers measurements," Appl. Opt. **43**, 1991–1995 (2004).

40. R. L. Eriksen, P. C. Mogensen, and J. Glückstad, "Multiple-beam optical tweezers generated by the generalized phase-contrast method," Opt. Lett. **27**, 267–269 (2002).

## 1. Introduction

Multiple trap optical tweezers have been instrumental in exciting studies of, e.g., chromatin organization by DNA-structuring proteins [1, 2], the role of cell polarisation in chemotaxis [3], and many-body dynamics of hydrodynamical coupled particles [4], also they have a high potential for lab-on-a-chip devices [5]. Boosted by the rapid advances of holographic light shaping techniques within the fields of imaging and optical fiber communication [6], significant progress has been made to dynamically generate advanced optical trapping landscapes [7–10] and holographic optical tweezers (HOTs) are one of the most common techniques for creating multiple traps. Beside the possibility to manipulate and actively perturb a system of interest with extrinsic forces, the ability to precisely measure the response of the investigated system like, e.g., a living cell reacting to external mechanical stimuli, is of utmost interest, as it allows for quantitative investigations of the underlying (bio-)physical mechanisms at play. However, the development of suitable detection methods, to accurately measure forces and displacements of multiple trapped particles, has proven quite challenging.

For force and distance detection in optical traps, the two prevalent detection schemes are camera or photodiode based [11]. Interferometric photodiode based detection is typically used for single or dual traps due to its unrivaled spatial and temporal resolution [12]; this method allows for extraction of displacements and forces at bandwidths of hundreds of kHz with subnanometer and piconewton accuracy in all three dimensions [13, 14]. The method's incompatibility with the detection of multiple traps presents a major drawback, though, and has limited its use in conjunction with holographic optical tweezers.

Therefore, camera-based detection has been widely used for multiple tweezers. However, in comparison to photodiode detection, this implies reduced spatial and temporal resolution, offline data processing, higher costs and limited axial detection capability. On the positive side, camera based detection easily allows for monitoring many particles in parallel [15–17]. To improve the axial detection capabilities of multi-trap camera based imaging, stereoscopic imaging [18,19] and point spread function engineering [20] have been presented. Furthermore, holographic particle tracking methods [21–24], relying on analyzing recorded interference patterns, created under coherent illumination, have been demonstrated to achieve nanometer-scale resolution in both the lateral and axial directions. However, the downside of all these techniques is a low temporal resolution and a rather challenging and computationally demanding data analysis [5]. The speed of camera detection is ultimately limited by the number of detected photons per recorded image, resulting in a low signal-to-noise ratio for high frame rates. Pushing the boundaries by sophisticated "smart cameras" with integrated image processing [25–27] and by specialized high radiance illumination [28], camera-based solutions can reach frame rates of tens of kHz which is comparable to the performance of standard QPD detection. However, photodiodes can operate at significantly higher bandwidths, as used, e.g., for measuring Brownian particle movement with a stunning bandwidth of 75 MHz [29].

Photodiode-based detection for multiple-beam optical traps is a worthwhile challenge as it opens the door to ultra-fast and precise force and distance measurements by multiple tweezers [16,30]. To this end, one solution has been to create one of the multiple traps with a polarization that is orthogonal to the polarization of the additional traps; the signal from the 'orthogonal trap' can then be separated out using polarization optics and used for individual interferometric detection. However, the two available polarization states set a limitation on the maximal number of interferometrically detectable traps using this method [1, 2, 30]. An alternative method is to use a time-shared QPD detection [31, 32], i.e., a sequential trap detection, which trades a

lowered sample rate for additional detectable traps.

Here, we present and demonstrate a new detection method for multi-beam optical tweezers which enables simultaneous, fast and accurate detection of multiple optical traps by photodiodes. The method is low-cost and easy to implement in existing setups. It is based on spatial filtering and, as shown for dual traps [33], allows to exclusively detect the signal from any individual trap of interest. The signal separation is achieved by selective light transmission using a pinhole positioned in a plane optically conjugate to the sample plane, where the trapping is performed. We show how to use this principle of spatial filtering in a simple, yet powerful, manner to perform parallel position and force measurements of multiple beads using photodiodes placed in the back-focal-plane of holographic optical tweezers. For each individual trap, we confirm that hallmarks of optical trapping as, e.g., the linear QPD detection range and the linear power dependency of the trap stiffness, remain valid.

## 2.   Principle of signal separation

Interferometric detection schemes are based on capturing the interference pattern, created by the coherent superposition of un-scattered and forward-scattered light by the trapped object, using position sensing devices, e.g., quadrant photodiodes. Typically, the photodiodes are not positioned precisely at the back-focal-plane of the light-collecting condenser, instead, for optimal performance, one or multiple relay lenses are used for creating a scaled image of the interference pattern that fills the active region of the photodiode. Due to this additional imaging, an intermediate plane exists, which is optically conjugated with the sample plane. This can be advantageously exploited for signal selection, as illustrated in Fig. 1. In this conjugate plane, an image of the sample plane is formed, which is a replication of the optical traps in the sample plane, modified according to the optical transfer function of the lenses in-between. Accurately positioning a pinhole in this plane allows for the selective transmission of a chosen trap of interest for subsequent individual interferometric detection. For dual-beam optical traps, it was shown that a similar spatial filtering rejects the signal from the adjacent trap and crosstalk levels of less than 5% could routinely be achieved (although, dependent, e.g., on pinhole size); combining spatial filtering with polarisation-based filtering provided crosstalk levels less than 0.2% for dual traps with orthogonal polarization [33].

## 3.   Experiment

### 3.1.   Optical setup

Holographic optical tweezers were implemented through the back port of an inverted microscope (Leica DM IRBE), the setup is sketched in Fig. 1. An expanded Gaussian-shaped laser beam (1064nm CW Nd:YVO$_4$ laser, Spectra Physics J20I-BL-106C-02), with an initially flat wavefront profile, was phase-modulated by a diffractive optical element (HOLO/OR LTD., MS-231-I-Y-A). The plane of the diffractive optical element was optically conjugated with the back-focal-plane of the objective using a 1:1-telescope, to ensure an effective conversion of the phase-modulation to the intensity distribution in the focal plane of the objective (63X, NA=1.2, water immersion, Leica HCX PL APO W CORR CS) [34]. Two #1.5 glass cover slips, sandwiched on top of each other and separated by double sided sticky tape, formed a perfusion sample chamber, 80$\mu$m in thickness. The chamber contained polystyrene beads with a mean diameter of 0.96$\mu$m (PS03N/9396, Bangs Laboratories), dispersed in Millipore water. All trapping experiments were conducted with the trapping plane far from any surfaces, i.e., 15$\mu$m above the bottom of the chamber. An oil immersion condenser (NA = 1.4, Leica S1 551004), opposing the microscope objective, was used for light collection. The back-focal-plane of the condenser was imaged onto a QPD (Si-PIN photodiode, Hamamatsu S5981) using a relay lens
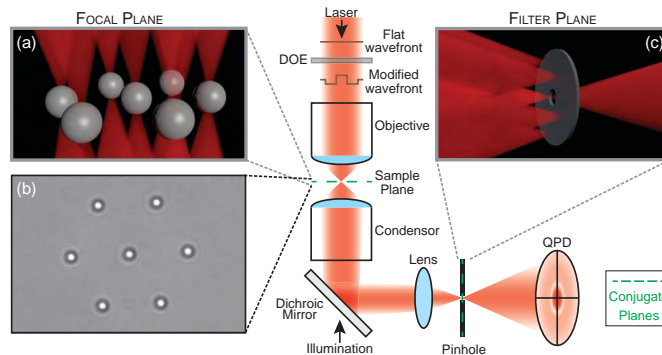
Fig. 1. Illustration of the detection method. A diffractive optical element (DOE) is used to modify the wavefront of the trapping beam to holographically generate a complex trapping landscape in the sample plane, e.g., a hexagonal arrangement of seven optical traps. By means of a relay lens, the back-focal-plane of the condenser is imaged onto a quadrant photodiode (QPD). A pinhole, placed in the intermediate plane, which is optically conjugate to the sample plane, selects a single trap for transmission and detection. Inset a: Visualization of trapping geometry in the sample plane. Inset b: Top view captured by camera, bead diameter = 1 $\mu$m. Inset c: Visualization of spatial filtering in the conjugate plane.

with a focal length of 5$cm$.

To track a single particle at a time we added a pinhole (diameter 15$\mu m$, Thorlabs P15S) in the optical plane where an image of the sample was formed. Micro-positioning (Thorlabs, ST1XY-D) of the pinhole allowed for precise alignment of the pinhole with a specific trap of interest. The signal from the photodiode was digitized using an A/D card after amplification by a low-noise amplifier. The total signal of all four quadrants on the QPD was used as a read-out of the transmitted intensity while aligning the pinhole. Good alignment could be achieved by maximizing the transmitted signal and verifying that a Lorentzian power spectrum could be measured when a bead was trapped in the trap of interest. This optimization process took 5 minutes to do 'by hand', however, this part of the experimentation could be optimized by a feedback mechanism between the read-out on the photodiode and an automatized positioning of the pinhole.

To track multiple (i.e., more than two, here proven for three) particles simultaneously, we split the laser beam into three beams keeping the polarization of the original laser beam in each of the multiple daughter-beams. This was done by inserting two beam splitters (10$mm$, Thorlabs) after the relay lens. In each of the multiple optical paths we added a pinhole in the optical plane conjugate to the sample plane. Each pinhole was mounted on a separate micro-positioner (Thorlabs, ST1XY-D). This allowed for precise alignment of the pinholes with each of the traps of interest. The optimal pinhole size and the required precision in pinhole position depend on the magnification produced by the relay lens. For the multi-particle tracking measurement we used a relay lens with focal length of 7.5$cm$, which magnified the waist of each trap and, most importantly, provided a larger space for positioning of the optical elements. In our case, the inter-trap distance between two adjacent traps in the 7-trap system was measured to be $\sim 40\mu m$ in the image plane. Therefore, we used pinholes with diameters of 30$\mu m$ and 50$\mu m$. The light

passing through each of the pinholes was collected with a separate photodiode, all photodiodes being similar to the one described above, and the signals from each of the traps were treated in parallel.

Trap calibration via power spectral analysis was done as previously described [33] using a freely available Matlab program [35], that also includes corrections for the significant filtering effect of the photodiode [36], aliasing and other minor effects. Briefly, the 1D dynamics of a trapped bead, undergoing confined Brownian motion in a harmonic optical potential, can be described by the Langevin equation

$$m\ddot{x}(t) + \gamma\dot{x}(t) + \kappa x(t) = F_{\text{therm}}(t), \tag{1}$$

where $x$ denotes the bead's time-dependent position, $m$ its mass and $\gamma$ its friction coefficient given by Stokes' law. The random and time-dependent force term $F_{\text{therm}}(t)$ accounts for the stochastic thermal collisions with the solvent molecules, and the strength of the harmonic optical trapping potential, $F_{trap} = \kappa x$, is characterized by the spring constant $\kappa$. The dynamics in the other two translational directions are equivalent to that described above, however, each with a different $\kappa$. The Langevin equation can be recast into a power spectrum, describing the bead's motion in the optical trap in terms of its frequency components. The sampled power spectra will vary from experiment to experiment due to the stochastic character of $F_{\text{therm}}(t)$. However, the theoretically predicted power spectrum of the Langevin equation, $P(f)$, which is simply the expectation value of the experimental power spectrum, $P_{\text{exp}}(f)$, can be expressed as

$$P(f) = \left\langle P_{\text{exp}}(f) \right\rangle = \frac{A}{f_{\text{c}}^2 + f^2}. \tag{2}$$

Here, $f_c$ is the corner frequency which is defined as $\kappa = 2\pi\gamma f_{\text{c}}$ and $A$ is a constant that carries information about the conversion of the recorded QPD voltage signal to bead displacements in metric units, see details in [33].

### 3.2. Experimental results

A diffractive optical element created seven optical traps arranged as in a hexagonal lattice, i.e., one central trap was surrounded by a hexagon of traps. The distance between neighboring traps (see Fig. 1(b)) was measured to be $6.7\mu$m in the sample.

To examine the performance of the spatial filtering detection method in a multi-trap system, we selected the central trap by positioning the pinhole so that only the light from the central trap was passed onto the photodiode and all other traps were blocked. As illustrated in Figs. 2(a)–2(c), we compared the trap characteristics obtained in three configurations: Fig. 2(a) The situation, when only the trap of interest contained a trapped bead; Fig. 2(b) the situation, when all seven traps contained trapped beads; and Fig. 2(c) the situation, when the surrounding six traps contained beads, while the trap of interest was left empty. By comparing the power spectra from the situations of Figs. 2(a) and 2(b), shown by purple squares and green circles, respectively, in Fig. 2(d), it is clear that the two situations yield power spectra that are indistinguishable by eye. The full lines in Fig. 2(d) show the fit of a Lorentzian power spectrum to the data. These fits returned corner frequencies, $f_c$, that, within the error bars, were identical for situations of Figs. 2(a) and 2(b). Also, both of these situations yielded power spectra distinctly different from that of an empty central trap (shown with orange triangles in Fig. 2(d)), which had a signal that was orders of magnitude lower. Hence, the method allows for individual detection of the trap of interest and efficiently rejects the signal from the remaining traps.

The desired information is knowledge of the distances travelled by the bead and the forces exerted on the bead by the trap. Therefore, an important step is the determination of the conversion factor, which mediates conversion from the measured QPD signals in volts to distance
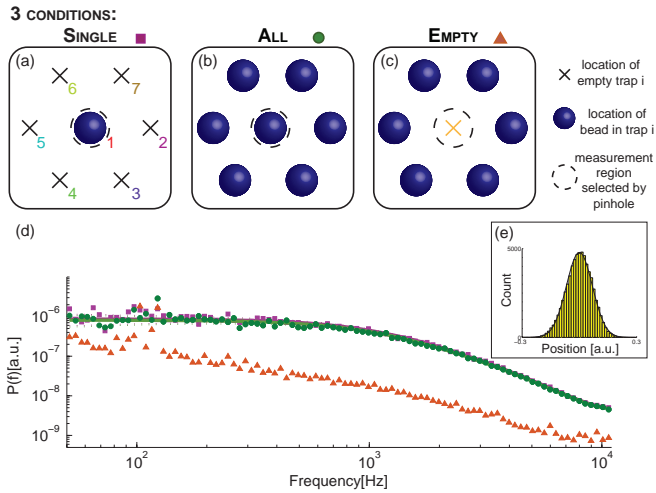
Fig. 2. Examination of spatial filtering in a multi-trap setup. a)–c) Illustrations of the three different experimental conditions, the pinhole allows light from the central trap to be passed on to the photodiode. d) Overlay of the measured power spectra for the situations shown in a) (purple squares), b) (green circles), and c) (orange triangles). Solid lines are fits to the experimental data for situations a) (purple) and b) (green) using the calibration program from Ref. [35] (the fitting range was 120Hz to 11kHz). Within the error bars (dashed lines) the two fitted power spectra overlap. The signal levels of an empty trap of interest (orange triangles) are orders of magnitude lower than for a full trap of interest. e) Position histogram of a trapped particle overlayed by a fit based on the theoretically expected Gaussian distribution.

measured in metric units. For easy conversion, it is convenient if one utilized a range where there is a linear relation between the QPD voltage signal and the actual distance travelled by the bead. This relation can be investigated by recording the QPD signals while scanning a bead that is immobilized on a cover slip through the focal region of the optical trap. The insets of Figs. 3(a) and 3(b) show that, also with the pinhole inserted, there does exist a wide range with a linear relation between the QPD voltage signal and the distance travelled by the bead (right insets) and that the linear detection in one lateral direction, in a certain region, is essentially independent on the other lateral direction (left insets). Knowledge of the conversion factors in all three dimensions thus allows for extraction of $x$, $y$ and $z$ in metric units.

A linear relation between the power of the trapping beam and the trap stiffness, $\kappa$ is a hallmark of optical trapping. Figures 3(a) and 3(b) show $\kappa$ as a function of laser power in the trap in the lateral $x$ and $y$ directions, respectively. The graphs show the result of a total of 3780 recorded and analyzed bead trajectories and confirm the expected linear dependency of $\kappa$ versus power for all seven traps. With knowledge of $x$ (or $y$) and the corresponding $\kappa$, the force exerted on the particle can be found and the calibration is complete.
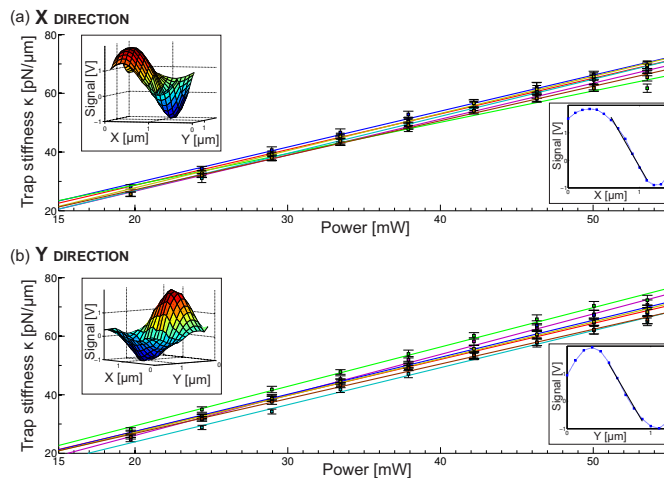
Fig. 3. Lateral force and displacement detection. a) The main graph shows the linear dependency of the trap stiffness versus laser power in the *x*-direction for all seven traps, the mean and one standard deviation of the measurements (N=30 per data point) are drawn in black. Full lines (color-coding according to Fig. 2(a)) are linear ordinary least square fits ($R^2 > 0.97$) to the data originating from each trap. The abscissa values denote the power of a single trap in the focal plane. Lower right inset: QPD voltage signal as a function of distance travelled by the bead in the *x*-direction. Upper left inset: Two-dimensional conversion factor scan, showing the dependency of the QPD voltage signal as function of both the *x*- and *y*-directions. b) Same as a), but for the Y-direction.

According to the DOE manufacturer, the total laser power reaching the focal plane is distributed equally between the seven focal points, with a total efficiency of 77% and a relative difference of maximal 5%. The power dependency of the spring constants, i.e., the slopes in Fig. 3, of the seven traps were measured to be $(1.205 \pm 0.069)\frac{\text{pN}}{\mu\text{m mW}}$ for the x-direction and $(1.276 \pm 0.067)\frac{\text{pN}}{\mu\text{m mW}}$ for the y-direction which is in fine agreement with typical values, e.g., from traps based on a single laser beam [37, 38].

As it is sometimes necessary to be able to perform quantitative measurements of force and distance in the axial direction, we also demonstrated the applicability of the method in the axial direction. The setup was still as shown as in Fig. 1 and, by restricting the aperture of the condenser, we optimized the dependency of the summed signal of the four QPD quadrants on the axial position of the trapped bead [39]. In this way, power spectra of the axial motion of the trapped beads were obtained. As shown in Fig. 4, even with the pinhole inserted, the axial direction yielded a linear relation between the QPD voltage signal and the distance travelled by the bead, the positions visited by the trapped bead yielded a Gaussian distribution, and the power spectrum had the expected Lorentzian shape. The axial spring constant, $\kappa_z$, was approximately 1/3 of the lateral spring constants, as is typical for optical traps. In our experiment, all traps had their focus in the same axial plane as they were created by a diffractive optical element. If, however, the axial foci of the traps were axially displaced from each other, as possible, e.g., by using the generalized phase contrast method [40], it might be important to perform a
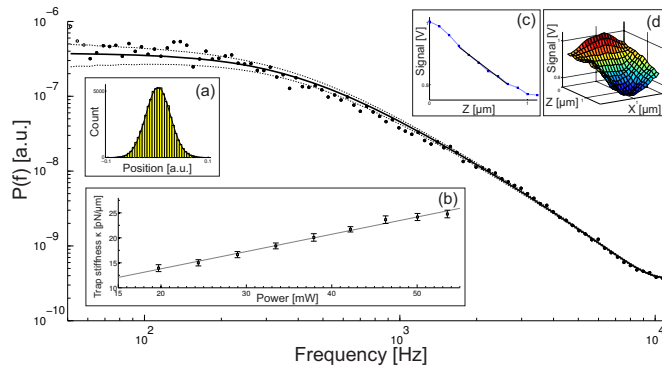
Fig. 4. Axial detection. The main graph shows the experimental axial power spectrum fitted by a Lorentzian function. Insets: a) Histogram of the axial displacement of a trapped bead. b) The axial spring constant as a function of laser power in the trap. The linear fit ($R^2 >$ 0.97) has a slope of $0.345 \frac{pN}{\mu m\,mW}$. c) The total QPD signal as a function of the bead's axial displacement. d) Two-dimensional scan of the total QPD signal for XZ-displacement. As expected, around the equilibrium position, the total signal depends mainly on the axial position, while being nearly insensitive to lateral displacement in *x*-direction.

spatial filtering also in the axial direction. The problem with axial trap displacements is that if one trap, say the central one, is displaced upstream of the optical path (compared to the rest of the traps) there is a chance that some of the marginal rays of the central trap reach the other focal spots and give rise to a significant amount of crosstalk. This effect gives a maximum of the advisable axial distance between traps while employing axial photodiode detection, even if spatial filtering is performed. This maximum advisable distance depends on the NA of the converging optics and on the inter-trap distance. The lower the NA and the larger the inter-trap distance, the longer the advisable axial separation. In our case, if we would have been able to axially displace our traps, we estimate that the advisable axial separation distance would have been $\sim 10\mu m$.

Above we demonstrated the applicability of the spatial filtering method to detect a single trap of multiple-beam optical tweezers. However, the method is equally applicable to detect multiple particles within a multiple-beam optical trap simultaneously. To demonstrate photodiode detection of multiple (more than two) traps of arbitrary polarization, we performed a series of experiments where we simultaneously monitored three traps (the number of traps was only limited by the number of available photodiodes and low-noise amplifiers). We arbitrarily chose to monitor traps number 1, 2, and 4 (the numbering of the traps is visible in Fig. 2(a)), but any of the traps could have been chosen. As detailed under 'Optical setup' (Section 3.1) and visualized in Fig. 5(a), we used two beamsplitters to make three copies of the laser beams after the relay lens, inserted three pinholes, one for each beam (in a plane conjugate to the sample plane), and imaged each beam on one photodiode. In the experiments, we first tracked an individual bead that was trapped by either trap 1, trap 2, or trap 4. Figure 5(b) (first row) shows the corresponding power spectra measured in the three traps and Table 1 gives the corresponding lateral and axial corner frequencies for pinhole sizes of 30µm and 50µm, respectively. The two lateral directions were very similar, therefore only the *x* direction is given in the table. These results show a clear Lorentzian power spectrum of the occupied trap and a non-Lorentzian noisy
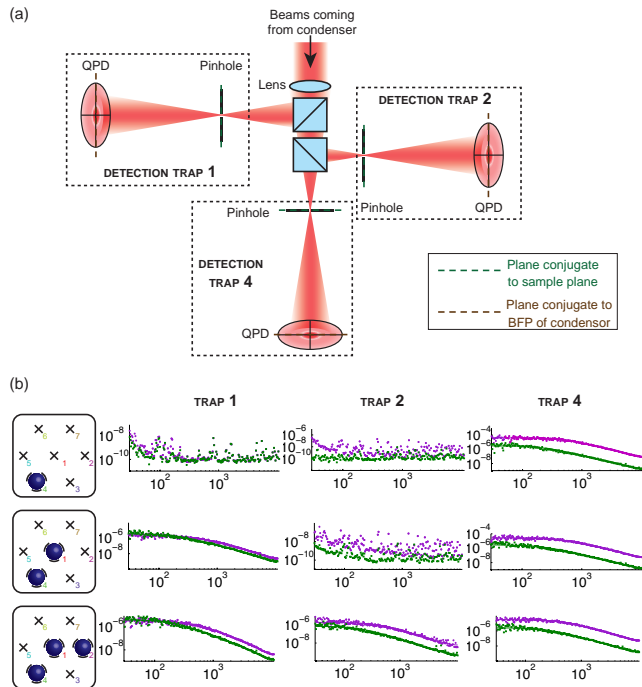
Fig. 5. Simultaneous detection of multiple beads occupying multiple traps. a) Schematic of how the detection part of the setup was modified in order to track three trapped beads simultaneously using photodiodes. b) The left schematics show the occupancy of the traps during each of the three types of measurements. The right graphs show corresponding lateral (purple) and axial (green) power spectra. For these experiments the pinhole diameter was $30\mu$m.

Table 1. The measured corner frequencies from multiple traps detected simultaneously. The traps are numbered and filled as shown in Fig. 5(b). Experiments were done using pinholes with diameters of either 30$\mu$m (upper part of table) or 50$\mu$m (lower part of table). Each number denotes the average of 10 measurements and the error is given as one standard deviation. A '-' denotes that the trap was empty and the power spectrum non-Lorentzian.

| | | | 30$\mu$m pinhole | | | | | |
| --- | --- | --- | --- | --- | --- | --- | --- | --- |
| | | | Trap 1 (T1) | | Trap 2 (T2) | | Trap 4 (T4) | |
| occupancy | | | X | Z | X | Z | X | Z |
| T1 | - | - | 482±15 | 201±6 | - | - | - | - |
| - | T2 | - | - | - | 480±18 | 215±6 | - | - |
| - | - | T4 | - | - | - | - | 481±13 | 213±5 |
| T1 | T2 | - | 444±12 | 198±7 | 404±10 | 194±6 | - | - |
| T1 | - | T4 | 422±10 | 194±7 | - | - | 460±10 | 222±9 |
| - | T2 | T4 | - | - | 378±35 | 214±5 | 453±19 | 208±5 |
| T1 | T2 | T4 | 436±10 | 196±6 | 478±18 | 199±7 | 444±13 | 220±9 |
| | | | 50$\mu$m pinhole | | | | | |
| | | | Trap 1 (T1) | | Trap 2 (T2) | | Trap 4 (T4) | |
| occupancy | | | X | Z | X | Z | X | Z |
| T1 | - | - | 449±12 | 195±6 | - | - | - | - |
| - | T2 | - | - | - | 433±14 | 210±9 | - | - |
| - | - | T4 | - | - | - | - | 495±27 | 235±8 |
| T1 | T2 | - | 460±8 | 184±6 | 489±11 | 208±3 | - | - |
| T1 | - | T4 | 460±12 | 187±9 | - | - | 490±17 | 228±10 |
| - | T2 | T4 | - | - | 485±10 | 224±11 | 488±14 | 236±9 |
| T1 | T2 | T4 | 463±15 | 188±4 | 473±9 | 223±6 | 490±8 | 225±9 |

low signal from the empty traps, as expected, thus confirming a separation of the signals. The obtained corner frequencies are quite similar for all three traps, which is to be expected as the power was distributed evenly between them and exactly the same bead was transferred from one trap to another. Second, we performed experiments with two traps occupied, the corresponding results are shown in the second row of Fig. 5(b) and in Table 1. Again, the power spectra look as expected and the corner frequencies are in good agreement, especially considering the fact that these were different beads (with individual diameters). Third, we performed an experiment with all three traps occupied simultaneously, the results are shown in the last row of Fig. 5(b) and in Table 1. Again, all power spectra were as expected and the corner frequencies were in good agreement, thus demonstrating the ability to use a photodiode to successfully track multiple particles in a multiple beam optical trap simultaneously.

Two pinhole sizes were employed in the simultaneous tracking of multiple beads, 30$\mu$m and 50$\mu$m. Judging from Table 1, these two pinhole sizes yielded quite similar results and both work fine for spatial filtering in the setup depicted in Fig. 5(a). Based on the results of Ref. [33], however, the smaller pinhole probably suppresses crosstalk slightly more efficient than the larger.

It is straightforward to extend this method to a larger number of traps. For this, one should simply split the beam into more daughter-beams and use one pinhole and one photodiode for each trap. It might be an advantage to use a relay lens with a larger focal length, as this would

provide a larger physical space for the necessary optical elements and it would employ a larger distance between the traps in the filtering plane, thus allowing for the use of a larger pinhole and lowering the precision requirements during pinhole adjustments.

## 4. Conclusion

This novel spatial filtering technique allows for fast and precise photodiode based back-focal-plane detection of multiple-beam optical tweezers that are formed, e.g., by holographic techniques [9] or by generalized phase-contrast [40]. Spatial filtering enables a separation of signals originating from different traps and we verified its capability of detecting three-dimensional position and force. Using this method, the usual hallmarks of optical trapping, e.g., a linear relation between photodiode signal and distance travelled and a linear relation between the spring constant and the laser power, were confirmed. The technique is here demonstrated for tracking up to three beads simultaneously in lateral and axial directions. The separation of the signals is independent of the polarization of the laser beam and can easily be extended up to a large number of beads with the only practical limitation being the number of photodiodes available. If the detection technique would be highly parallelized, splitting the beam many times would result in a decreased signal-to-noise ratio and thus comes at the cost of reduced accuracy. The method here presented will allow multiple-tweezers based high-bandwidth investigations, e.g., of interactions of trapped networks of particles [25, 29] and will improve single molecule experiments that involve tracking of multiple tracers [1, 2].

# Dynamic operation of optical fibres beyond the single-mode regime facilitates the orientation of biological cells

Moritz Kreysing[1,2,*], Dino Ott[1,3,*], Michael J. Schmidberger[1,4,5,*], Oliver Otto[1,6], Mirjam Schürmann[6], Estela Martín-Badosa[7], Graeme Whyte[1,5] & Jochen Guck[1,6]

The classical purpose of optical fibres is delivery of either optical power, as for welding, or temporal information, as for telecommunication. Maximum performance in both cases is provided by the use of single-mode optical fibres. However, transmitting spatial information, which necessitates higher-order modes, is difficult because their dispersion relation leads to dephasing and a deterioration of the intensity distribution with propagation distance. Here we consciously exploit the fundamental cause of the beam deterioration—the dispersion relation of the underlying vectorial electromagnetic modes—by their selective excitation using adaptive optics. This allows us to produce output beams of high modal purity, which are well defined in three dimensions. The output beam distribution is even robust against significant bending of the fibre. The utility of this approach is exemplified by the controlled rotational manipulation of live cells in a dual-beam fibre-optical trap integrated into a modular lab-on-chip system.

[1] Cavendish Laboratory, Department of Physics, University of Cambridge, Cambridge CB3 0HE, UK. [2] Max Planck Institute of Molecular Cell Biology and Genetics, Dresden 01307, Germany. [3] Niels Bohr Institute, University of Copenhagen, Copenhagen 2100, Denmark. [4] Max Planck Institute for the Science of Light, 91058 Erlangen, Germany. [5] Department of Physics, Friedrich-Alexander-Universität Erlangen-Nürnberg, 91052 Erlangen, Germany. [6] Biotechnology Center, Technische Universität Dresden, 01307 Dresden, Germany. [7] Department of Applied Physics and Optics, Universitat de Barcelona, 08028 Barcelona, Spain. * These authors contributed equally to this work. Correspondence and requests for materials should be addressed to M.K. (email: kreysing@mpi-cbg.de).

1

When an arbitrary light field enters an optical fibre, its propagation is most conveniently described on the basis of shape-invariant eigenfunctions of the propagation operator. The intensity distribution at any point along the fibre can then be obtained as the coherent sum of the initial modal fields multiplied by a complex phase factor. Because of non-trivial intermodal dispersion relations in optical fibres the dephasing between different modes leads to altered interference conditions giving rise to periodic changes of the intensity distributions even along an unperturbed fibre[1] (Fig. 1a).

An often used, simplified description regards fibre modes as having a linear polarization, which can be variable in amplitude and sign, but not in orientation across the wavefront[2]. In-plane field amplitudes of these linearly polarized (LP) modes possess a scalar, orbital structure with radial and angular quantum numbers. This approximation is sufficient to explain the sudden occurrence of higher-order fibre modes with increasing fibre core diameter or refractive index step between core and cladding. Such an LP mode description has recently been used to measure and invert an empirical transmission operator between the two ends of a static multimode fibre[3]. LP modes, however, fail to predict the actual evolution of intensity profiles inside optical fibres. The reason for this rests in the violation of cylindrical fibre symmetry by these simplified wave functions (Fig. 1b left-hand side). Taking into account the symmetry of the problem requires a rigorous vectorial treatment of the wave equation in cylindrical coordinates. The solution, vectorial fibre modes (Fig. 1b right-hand side), are primarily classified by radial and angular quantum numbers as well. In addition, however, a spin quantum number is introduced, which describes the aligned or anti-aligned rotation of the polarization vector with the angular position on the wavefront. This photon spin gives rise to a splitting of propagation constants into a fine structure, which explains the decay of LP modes after half the beating length (for example, $l_{beat} \approx 36$ cm for a Nufern 780HP fibre), which is on the order of $10^5$–$10^6$ wavelengths[1] (Fig. 1a, see also Methods). One ultimate result of this oscillatory mode dephasing is the practical difficulty in passing spatial information through optical fibres in a well-controlled way.
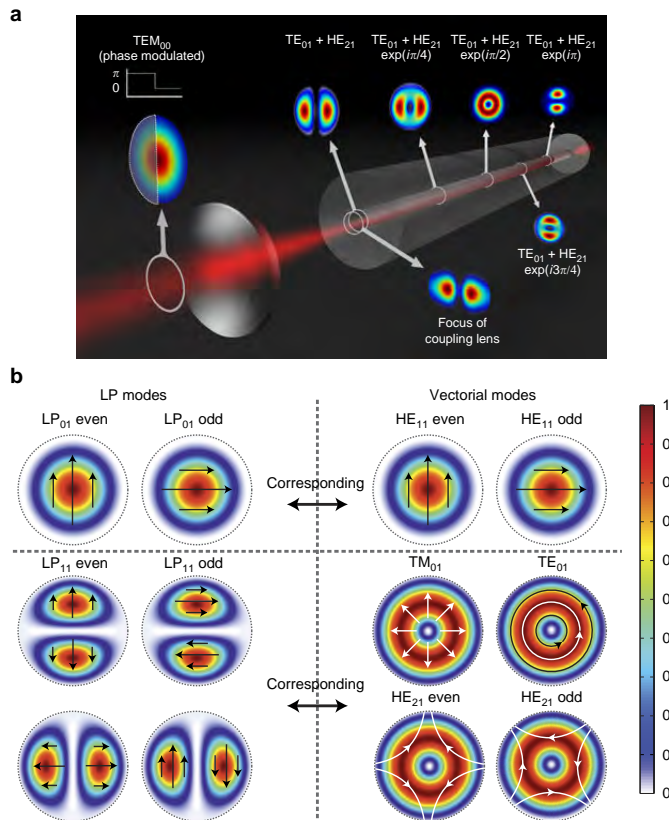


**Figure 1 | Illustration of the vectorial nature of fibre modes and its impact on mode dephasing.** (**a**) A phase-modulated Gaussian intensity distribution (first from left) is imaged onto the fibre end and couples to a combination of the $TM_{01}$ and $HE_{21}$ vectorial fibre modes. This combination then experiences intermodal dephasing, which leads to a periodic image deterioration with propagation along the fibre. For example, the intermodal beating length for mixtures of the $TM_{01}$ and $HE_{21}$ modes upon propagation in a Nufern 780HP fibre is ~36 cm when operated at 633 nm. (**b**) Each of the scalar LP modes on the left side (the first two are shown) are linear superpositions of appropriate pairs of the vectorial fibre modes (right side). Small black and white arrows indicate polarizations. Colour scale indicates field intensities (in arbitrary units).

Recently, much progress has been made towards this goal by successfully applying adaptive optics methods, developed for aberration correction and scattering compensation[4,5], to the shaping of the output beam of multimode fibres[3,6–12] and photonic crystal fibres[13]. For this purpose, output responses to arbitrary sets of input fields (typically delta-peaks at the fibre entrance) have been probed experimentally, allowing for the construction of a transmission operator. This kind of careful empirical characterization of static multimode fibres allows both through-fibre imaging of microscale beads and their optical manipulation when located on a planar surface[7,10]. However, the lack of orthonormality between the many modes propagating in such 50-μm core fibres imposes practical limitations on achievable output fields, especially when trying to generate high-quality coherent fields that depend on the simultaneous excitation of adjacent fibre modes[7]. Although there is no fundamental reason why output beams of high modal quality should not be transmittable through multimode fibres, in practice this has been reported as very susceptible to noise, resulting in undesired interference effects in the generated fields.

Approaches, which define the output beams behind multimode fibres, need to suppress these unwanted interference effects between output modes either using iterative algorithms (mainly Gerchberg-Saxton type)[7] or time-sharing, of which the latter finds a sensible application in the imaging through multimode optical fibres[11]. In all cases, however, the use of true multimode fibres requires the fibres to be kept static to avoid modal mixing, which limits the practical applicability.

Here we use a complementary approach for transmitting spatial information through optical fibres that results in well-defined, non-trivial beams propagating nearly diffraction-limited in three dimensions (3D). The approach, which in general has been demonstrated previously[1,3], explicitly exploits the symmetry relation between the first few vectorial fibre modes, each of them being invariant under propagation. This allows for the selective excitation of pairs of vectorial modes that differ only regarding their spin quantum number and that are in phase periodically along the fibre (compare Fig. 1a). The beams emanating from the fibre end are near diffraction-limited and of LP mode type. Because their complex amplitude distribution closely resembles higher-order Laguerre–Gaussian beams, which are shape-invariant under free-space propagation[14], the generated beams are highly suited for applications where the precise definition of light distribution in 3D is desired, such as in optical trapping. In addition, the use of a few-mode fibre renders the few selected modes largely robust against fibre bending, which adds an important practical dimension to this approach. We demonstrate its utility by using the beams generated for the controlled rotation of single biological cells in a fibre-based dual-beam laser trap incorporated into a lab-on-chip system. This could find far-reaching applications in the area of single-cell tomography, but also in general for the robust transmission of spatial information through optical fibres.

## Results

**Experimental realization.** To excite individual modes experimentally (compare Fig. 2), either a 633-nm or a 1,072-nm single-mode laser beam, depending on the fibre used (see Methods), was expanded to a diameter of 8 mm to exploit the full resolution of the phase-only spatial light modulator (SLM; X10468-07, Hamamatsu, Japan), off which it was then reflected. A phase preserving telescope in 4*f*-configuration (best-form lenses L2 and L3, Thorlabs, UK) was used to project the spatially filtered and demagnified image of the field distribution into the back-focal plane of an aspheric coupling lens. Minor residual aberrations

of the laser beam at this critical point were quantified with a Shack–Hartman wavefront sensor and pre-compensated with the SLM (see Methods and Supplementary Fig. 1). Precision coupling was likewise achieved by SLM scanning of the laser beam over the well-prepared fibre core (see Methods and Supplementary Fig. 2) in two orthogonal directions and by fitting the coupling ratio with an appropriate model function (see Methods and Supplementary Fig. 3). Lateral alignment precision better than 15 nm was maintained for >30 min (see Supplementary Fig. 3). Appropriate fibre lengths for particular pairs of vectorial fibre modes were chosen (see Methods for choice and stability).

**Mode rotation through few-mode fibre.** Imprinting symmetry-selective binary phase patterns on the SLM-diffracted wavefront prior to fibre coupling, previously suggested by von Hoyningen-Huene *et al.*[1], yielded the specific emission of LP-like intensity beams from the far fibre end-face (Fig. 3). Because these beams
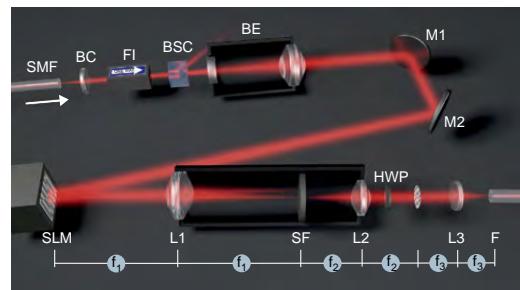


**Figure 2 | Schematic of the experimental setup.** A laser beam (either HeNe laser, $\lambda = 633$ nm, or Ytterbium-doped fibre laser, $\lambda = 1,072$ nm) passes through a beam collimator (BC), Faraday isolator (FI) and beam-splitting cube (BSC), and is then expanded in a beam-expander (BE) to cover the entire active area of the spatial light modulator (SLM). A phase profile, appropriate to excite the desired modes, is then imprinted onto the beam at its reflection from the SLM, the beam diameter is reduced via a telescope of lenses L1 and L2 and finally coupled into the few-mode fibre by the lens L3. The zeroth diffraction order beam reflected off the SLM is blocked with a spatial filter (SF). For some modes it is necessary to rotate the polarization with a half-wave plate (HWP). For trapping experiments, the unmodified laser beam is split off with the BSC to form the second beam in the dual-beam trap (its coupling into a single-mode fibre (SMF) is not shown).
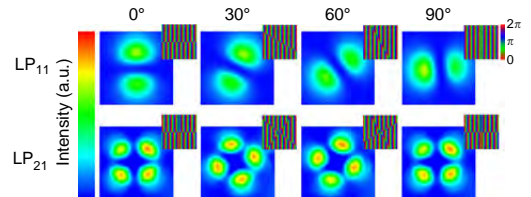


**Figure 3 | Rotational control of modes through an optical fibre with a spatial light modulator.** The image sequences show successive mode orientations of the laser beam ($\lambda = 633$ nm) emitted from the optical fibre (Nufern 1310B-HP) for an $LP_{11}$ mode (top row) and an $LP_{21}$ mode (bottom row). Callouts show the corresponding binary phase-modulating holograms displayed on the spatial light modulator. The four discrete orientations are exemplarily selected from a continuously varied angular orientation. See also Supplementary Movies 1 and 2.

rely on vectorial modes with orientational degeneracy caused by the symmetry of the fibre, field distributions at the fibre end-face can be readily rotated by the mere rotation of the input fields. Of note, a co-rotation of the polarization is required in the case of $LP_{11}$ modes, since here an additional dephasing of transverse electric and transverse magnetic fields may occur (cf., Fig. 1b; Supplementary Fig. 4). Co-rotation ensures that the same linear combination of vectorial fibre modes is excited at any angle.

While the rotation of non-trivial intensity distributions behind fibres using pre-calculated holograms has been demonstrated before, the methodology presented here complements these techniques since the mode-specific excitation of fibre modes *a priori* determines the phase distribution of the output field. More importantly, the use of select eigenfunctions of the propagation operator in this few-mode fibre, rather than many as in previous reports using multimode fibres, renders this approach rather insensitive to even significant bending of the optical fibre (Fig. 4).

**Cell rotation in a dual-beam laser trap.** Given the resulting 3D definition of the fibre output into free space, we demonstrate the beneficial application of this concept in the field of optical trapping of biological cells, objects much bigger than the wavelength of light. While single-beam gradient traps (commonly referred to as optical tweezers) are the established tool of choice to manipulate small biological samples down to the level of individual molecules via trapped colloids, the handle-free manipulation of entire cells with such tightly focused laser beams is difficult. A more appropriate approach to handle biological samples with sizes much in excess of the optical wavelength is offered by dual-beam laser traps[15] most conveniently implemented using optical fibres[16]. Here, axial trapping stability is guaranteed by two divergent, counter-propagating beams even for large[17] and multicellular samples[18,19]. One attractive aspect of fibre-based dual-beam laser traps is that the trap can be flexibly integrated into lab-on-chip setups for the convenient delivery of objects to be trapped[20–24]. At this point the insensitivity of the rotated output beams to fibre bending (Fig. 4) is particularly welcome.

Also, a fibre-based dual-beam laser trap is completely decoupled from the imaging optics, which renders it perfect for the contactless orientation of cells for tomographic microscopy purposes[25,26].

Towards this end, we demonstrate for the first time the trapping and precise rotation of cells perpendicular to the optical axis of a microscope in a dual-beam laser trap, eliminating the need for any mechanical rotation[18] or alignment[27,28] of optical fibres or apertures[29]. Figure 5a illustrates the working principle of a fibre-based dual-beam laser trap, into which we successfully integrated the setup presented above. The shaping and rotation of one of the laser beams via the SLM enables the dynamic control over the rotational degree of freedom of trapped cells about the laser-optical axis. The reorientation of cells in the trap is due to their tendency to maximize the overlap between regions of high refractive index and areas of high field intensity[29].

Red blood cells, exhibiting strong shape anisotropy with minimal internal structure, and HL60 cells, spherical cells with typical internal structure[30], were chosen as test objects based on their distinct morphological characteristics. For both cell types stable orientation and controlled rotation around the laser-optical axis could be achieved (Fig. 5b). This shows that both anisotropic shape and heterogeneous internal refractive index distribution are individually sufficient to determine the orientation of cells in the asymmetric trapping laser beam. The power in each of the beams can be <50 mW, so that the temperature in the trap is about 1.2 °C above ambient temperature and cell damage due to heating is avoided[31]. Of note, increasing the power leads to useful cell deformation (optical stretching)[32], so that cell rotation and cell stretching can be combined in one setup.

**Discussion**

A powerful future application is seen in combining this all-optical sample rotation technique with quantitative phase microscopy, thus enabling the determination of the 3D refractive index distributions of live cells[25,33,34], or in widefield fluorescent imaging from multiple angles with subsequent image fusion,
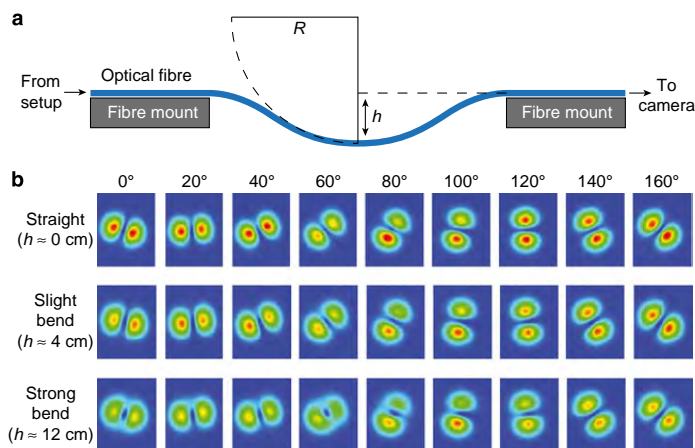


**Figure 4 | Insensitivity of mode rotation to fibre bending.** (**a**) Schematic illustrating the experimental setup. An $LP_{11}$ mode is coupled into a few-mode fibre and the output beam is monitored by a camera. The fibre is freely suspended over a 45-cm gap. Bending of the fibre can be induced by moving the fibre mounts closer together so that the fibre sags by different amounts, $h$, resulting in an approximate curvature of $1/R$. (**b**) Images of the output beam profiles as the input is rotated through 160° in 20°-steps for three different amounts of fibre bending. Mode rotations remain largely unaffected even in the slightly and strongly bent fibre configurations (that is, sagging by 4 and 12 cm, respectively) and still provide sufficient trapping potential for cell rotation.
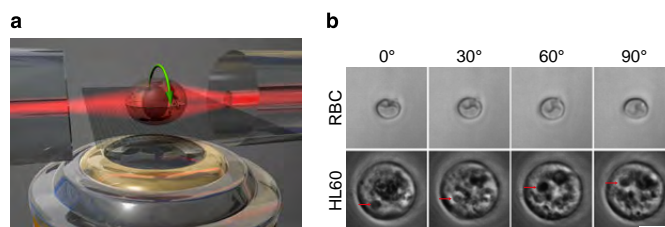
**Figure 5 | Rotation of biological cells in a fibre-based dual-beam laser trap operated beyond the single-mode regime. (a)** Schematic illustrating the basic setup of the trap. Two opposing, coaxially aligned optical fibres emit a near-Gaussian beam (single-mode fibre, from left) and a rotational orientation-enforcing $LP_{11}$ type beam (few-mode fibre, from right). The orientation of the $LP_{11}$ type beam on the right side is controlled by the adaptive manipulation of wavefronts with the SLM prior to fibre coupling. **(b)** Image sequence showing the precise orientation of a red blood cell (top row) and a spherical HL60 cell (bottom row) between 0° and 90°. Scale bar, 10 μm. To avoid cell damage, the wavelength was $\lambda = 1,072$ nm used with a Nufern 1310B-HP fibre. Arrows indicate object features, which help track the rotation (see also Supplementary Movies 3 and 4).

which would allow for significantly higher image quality and near-isotropic resolution[35].

We conclude that adaptive optics can offer a convenient way to deliver non-trivial beams of high quality through optical fibres. It is evident that, due to the strongly reduced number of modes in the fibres employed here, intermodal coupling is much less of an issue than in the multimode fibres extensively studied before[3]. We further demonstrate the beneficial use of the advancements presented by the rotational alignment of live cells, a prerequisite for a multitude of single-cell tomographic microscopy techniques. The robustness of our approach against fibre bending permits the convenient integration of optical cell rotation with microfluidic lab-on-chip systems for convenient cell delivery. The combination of robust fibre optics with a small and modular microfluidic chip renders the system ready to be used with any microscope system. This aspect sets it apart from previous dual-beam laser trap micromanipulation approaches using free-space optics[17,36] that do not easily permit this. More laboratory applications and completely novel approaches involving the delivery of spatial information through fibres, possibly extending the information content in fibre-based communication[37,38], seem possible.

## Methods

**Aberration correction.** Residual aberrations of the non-modulated beam in the back-focal plane of the coupling lens after alignment were conveniently corrected by displaying the appropriate Zernike polynomial on the SLM. The resulting root-mean-square flatness of the wavefront was better than $0.025\,\lambda$ as measured by a Shack–Hartman wavefront sensor (Supplementary Fig. 2). Aberrations of the fibre-coupled light field may also result from a not perfectly planar fibre end-face. To avoid unwanted coupling between modes, the fibre ends were manually polished to a root-mean-square flatness of $<5$ nm (Supplementary Fig. 3) in some experiments.

**Fibre choice and preparation.** The excitation of higher-order modes in single-mode fibres requires the use of light with appropriately shorter wavelength than the intended one. We used three kinds of commercial single-mode fibres (Nufern 780HP, 1060XP and 1310B-HP) and two different laser sources (5 mW HeNe laser, 05-LHP-151, Melles-Griot, UK for 633 nm or 5 W Ytterbium-doped fibre laser, YLG-1070-5LP, IPG Photonics, UK at 1,072 nm). Table 1 shows the different fibre and wavelength combinations and calculated V-parameters, which predict the guided mode groups ($LP_{01}$ only for $V < 2.405$, $LP_{01}$ and $LP_{11}$ for $2.405 < V < 3.83$ and $LP_{01}$, $LP_{11}$ as well as $LP_{21}$ for $V > 3.83$). All predicted mode groups could be experimentally excited and rotated through the fibre as indicated in the two rows on the right-hand side. In particular, the excitation and rotation of the two pure LP-type modes shown in Fig. 3 was conducted using a Nufern 1310B-HP at 633 nm. The same fibre type operated at 1,072 nm was used for the optical trapping experiments, as the smaller number of guided modes ensured the mode profile to be more stable under rotations.

For stably holding and rotating optically trapped samples, a strong azimuthal asymmetry in the fibre's output intensity profile is necessary. Thus, the phase relation between all vectorial fibre modes that are excited in the fibre has to be an

**Table 1 | Fibre types, V-parameters and observable mode groups.**

| | V 633 nm | V 1,072 nm | Observable mode groups (633 nm) | Observable mode groups (1,072 nm) |
|---|---|---|---|---|
| Nufern 780 HP | 2.58 | 1.64 | $LP_{01}$, $LP_{11}$ | $LP_{01}$ |
| Nufern 1060 XP | 3.50 | 2.06 | $LP_{01}$, $LP_{11}$ | $LP_{01}$ |
| Nufern 1310B-HP | 4.79 | 2.82 | $LP_{01}$, $LP_{11}$, $LP_{21}$ | $LP_{01}$, $LP_{11}$ |

For the three different fibre types and two different wavelengths (633 nm and 1,072 nm) used in the experiments, the first two columns show the V-parameters calculated and the second two columns the observed mode groups excited in the fibres.

integer multiple of $2\pi$ at the end of the fibre, as this will produce the ideal double-lobe $LP_{11}$ mode structure, which has initially been coupled into the fibre, without any donut-like contributions (see Fig. 1a for the effect of intermodal dephasing on the fibre's intensity profile). Hence, we developed a simple and reproducible iterative method that allows us to determine the fibre length $L_{fibre}$ to fulfil this condition: while projecting the desired mode onto one end-face, the opposite end is shortened in steps of $\sim 5$ mm until the output intensity profile resembles the $LP_{11}$ (that is, the desired, undistorted) mode shape when being inspected by eye or an infrared viewer. Then the coating is removed from the last 5–10 mm and the fibre is fixed to a metal plate. This allows the mode-mixture in the fibre output to be evaluated with a beam profiler while tiny pieces of the fibre's end are chopped off with a razor blade until the wanted modal content is achieved.

**Fibre-coupling optimization.** Fibre coupling into the few-mode fibre was optimized by scanning the laser beam over the fibre end-face in two orthogonal directions using the SLM. The measured coupling efficiency (Supplementary Fig. 4) was fitted with an appropriate function taking into account numerically evaluated coupling efficiencies[18]. The centre of these symmetric fits indicated the centre of the fibre core. The co-rotation of the polarization using a rotating half-wave plate (HWP) typically results in the orbiting of the laser focus on the fibre end-face around the optical axis due residual deviations from perfect surface parallelism. The radius of this orbit was determined to be 65 nm (Supplementary Fig. 4). The average deviation of the determined focus centres from this ideal orbit during rotation of the HWP indicates a 13-nm stability during the 30-min calibration procedure (Supplementary Fig. 4). The deviations introduced by the HWP rotation were compensated for by a fine-adjustable phase mirror implemented on the SLM.

**Optical trap.** To form a dual-beam laser trap, the scattering force from the anisotropic laser beam discussed so far was balanced by a second, counter-propagating laser beam with a rotationally symmetric Gaussian beam profile. That second trapping laser beam was generated by splitting the laser beam ($\lambda = 1,072$ nm) in the setup with a beam splitter (see Fig. 2) and then coupling it into a normal single-mode fibre (Nufern 1060 XP). The two optical fibres were mounted as described elsewhere[21] (see also Supplementary Fig. 5). It should be noted that mode dephasing, even at perfect fibre length, can result from bending, twisting or compressing the fibre, which induces birefringence[39], in principle. However, the setup described seems to be relatively robust against even considerable bending (cf. Fig. 4).

**Preparation of biological cells.** Human red blood cells and cells from a human leukaemia cell line (HL60/S4) were used as typical biological cells. Red bood cells were prepared by diluting 1 µl of fresh blood from a healthy male donor in 10 ml isotonic phosphate-buffered saline solution containing 1 p.p.t. EDTA to avoid blood coagulation. HL60 cells (gift from Ada and Donald Olins, University of New England) were cultured according to a well-established protocol[40]. Briefly, the culture medium was RPMI 1640 containing 10% heat-inactivated fetal bovine serum, $0.3\,g\,l^{-1}$ L-glutamine, and 1% penicillin/streptomycin at 37 °C and 5% $CO_2$. Cells were passaged every 2–3 days and diluted to concentrations of $\sim 10^5\,ml^{-1}$ for experimental use.

## References

1. von Hoyningen-Huene, J., Ryf, R. & Winzer, P. LCoS-based mode shaper for few-mode fiber. *Opt. Express* **21**, 18097–18110 (2013).
2. Snyder, A. W. & Love, J. *Optical Waveguide Theory* (Springer, 1983).
3. Carpenter, J., Eggleton, B. J. & Schröder, J. 110 × 110 optical mode transfer matrix inversion. *Opt. Express* **22**, 96–101 (2014).
4. Vellekoop, I. M. & Mosk, A. P. Focusing coherent light through opaque strongly scattering media. *Opt. Lett.* **32**, 2309–2311 (2007).
5. Čižmár, T., Mazilu, M. & Dholakia, K. *In situ* wavefront correction and its application to micromanipulation. *Nat. Photon.* **4**, 388–394 (2010).
6. Di Leonardo, R. & Bianchi, S. Hologram transmission through multi-mode optical fibers. *Opt. Express* **19**, 247–254 (2011).
7. Cizmar, T. & Dholakia, K. Shaping the light transmission through a multimode optical fibre: complex transformation analysis and applications in biophotonics. *Opt. Express* **19**, 18871–18884 (2011).
8. Mahalati, R. N., Askarov, D., Wilde, J. P. & Kahn, J. M. Adaptive control of input field to achieve desired output intensity profile in multimode fiber with random mode coupling. *Opt. Express* **20**, 14321–14337 (2012).
9. Papadopoulos, I. N., Farahi, S., Moser, C. & Psaltis, D. Focusing and scanning light through a multimode optical fiber using digital phase conjugation. *Opt. Express* **20**, 10583–10590 (2012).
10. Bianchi, S. & Di Leonardo, R. A multi-mode fiber probe for holographic micromanipulation and microscopy. *Lab Chip* **12**, 635–639 (2012).
11. Čižmár, T. & Dholakia, K. Exploiting multimode waveguides for pure fibre-based imaging. *Nat. Commun.* **3**, 1027–1029 (2012).
12. Plöschner, M., Straka, B., Dholakia, K. & Čižmár, T. GPU accelerated toolbox for real-time beam-shaping in multimode fibres. *Opt. Express* **22**, 2933–2947 (2014).
13. Euser, T. G. *et al.* Dynamic control of higher-order modes in hollow-core photonic crystal fibers. *Opt. Express* **16**, 17972–17981 (2008).
14. Siegman, A. E. *Lasers* (University Science Books, 1986).
15. Ashkin, A. Acceleration and trapping of particles by radiation pressure. *Phys. Rev. Lett.* **24**, 156–159 (1970).
16. Constable, A., Kim, J., Mervis, J., Zarinetchi, F. & Prentiss, M. Demonstration of a fiberoptic light-force trap. *Opt. Lett.* **18**, 1867–1869 (1993).
17. Thalhammer, G., Steiger, R., Bernet, S. & Ritsch-Marte, M. Optical macro-tweezers: trapping of highly motile micro-organisms. *J. Opt.* **13**, 044024 (2011).
18. Kreysing, M. K. *et al.* The optical cell rotator. *Opt. Express* **16**, 16984–16992 (2008).
19. Aabo, T., Banás, A. R., Glückstad, J., Siegumfeldt, H. & Arneborg, N. BioPhotonics workstation: a versatile setup for simultaneous optical manipulation, heat stress, and intracellular pH measurements of a live yeast cell. *Rev. Sci. Inst.* **82**, 083707 (2011).
20. Gast, F. U. *et al.* The microscopy cell (MicCell), a versatile modular flowthrough system for cell biology, biomaterial research, and nanotechnology. *Microfluid. Nanofluid.* **2**, 21–36 (2006).
21. Lincoln, B. *et al.* Reconfigurable microfluidic integration of a dual-beam laser trap with biomedical applications. *Biomed. Microdevices* **9**, 703–710 (2007).
22. Bellini, N. *et al.* Femtosecond laser fabricated monolithic chip for optical trapping and stretching of single cells. *Opt. Express* **18**, 4679–4688 (2010).
23. Bragheri, F. *et al.* Optofluidic chip for single cell trapping and stretching fabricated by a femtosecond laser. *J. Biophotonics* **3**, 234–243 (2010).
24. Bellini, N. N. *et al.* Validation and perspectives of a femtosecond laser fabricated monolithic optical stretcher. *Biomed. Opt. Express* **3**, 2658–2668 (2012).
25. Choi, W. *et al.* Tomographic phase microscopy. *Nat. Methods* **4**, 717–719 (2007).
26. Heintzmann, R. & Cremer, C. Axial tomographic confocal fluorescence microscopy. *J. Microsc.* **206**, 7–23 (2002).
27. Black, B. J. & Mohanty, S. K. Fiber-optic spanner. *Opt. Lett.* **37**, 5030–5032 (2012).
28. Kolb, T., Albert, S., Haug, M. & Whyte, G. Dynamically reconfigurable fibre optical spanner. *Lab Chip* **14**, 1186–1190 (2014).
29. Sato, S., Ishigure, M. & Inaba, H. Optical trapping and rotational manipulation of microscopic particles and biological cells using higher-order mode Nd: YAG laser beams. *Electron. Lett.* **27**, 1831–1832 (1991).
30. Chalut, K. J., Ekpenyong, A. E., Clegg, W. L., Melhuish, I. C. & Guck, J. Quantifying cellular differentiation by physical phenotype using digital holographic microscopy. *Integr. Biol.* **4**, 280–284 (2012).
31. Ebert, S., Travis, K., Lincoln, B. & Guck, J. Fluorescence ratio thermometry in a microfluidic dual-beam laser trap. *Opt. Express* **15**, 15493–15499 (2007).
32. Guck, J., Ananthakrishnan, R., Moon, T. J., Cunningham, C. C. & Käs, J. Optical deformability of soft biological dielectrics. *Phys. Rev. Lett.* **84**, 5451–5454 (2000).
33. Charrière, F. *et al.* Cell refractive index tomography by digital holographic microscopy. *Opt. Lett.* **31**, 178–180 (2006).
34. Su, J.-W., Hsu, W.-C., Chou, C.-Y., Chang, C.-H. & Sung, K.-B. Digital holographic microtomography for high-resolution refractive index mapping of live cells. *J. Biophotonics* **6**, 416–424 (2012).
35. Swoger, J., Verveer, P., Greger, K., Huisken, J. & Stelzer, E. H. Multi-view image fusion improves resolution in three-dimensional microscopy. *Opt. Express* **15**, 8029–8042 (2007).
36. Čižmár, T., Brzobohatý, O., Dholakia, K. & Zemánek, P. The holographic optical micro-manipulation system based on counter-propagating beams. *Laser Phys. Lett.* **8**, 50–56 (2011).
37. Ryf, R. *et al.* Mode-division multiplexing over 96 km of few-mode fiber using coherent 6 × 6 MIMO processing. *J. Lightwave Technol.* **30**, 521–531 (2012).
38. Richardson, D. J., Fini, J. M. & Nelson, L. E. Space-division multiplexing in optical fibres. *Nat. Photon.* **7**, 354–362 (2013).
39. Liu, J.-M. *Photonic Devices* (Cambridge Univ. Press, 2005).
40. Olins, A. L., Buendia, B., Herrmann, H., Lichter, P. & Olins, D. E. Retinoic acid induction of nuclear envelope-limited chromatin sheets in HL-60. *Exp. Cell. Res.* **245**, 91–104 (1998).

## Author contributions

M.K. and J.G. conceived the basic idea of an SLM-controlled optical cell rotator. M.K. and M.J.S. elaborated the theoretical aspects of the work. M.K. planned, supervised and supported the experimental implementation. D.O., M.J.S. and M.S. built the experimental setup. O.O., E.M.-B. and G.W. supported the SLM implementation and programming. M.J.S. performed the fibre-mode characterization and optimization experiments and D.O. performed the cell rotation experiments. M.K., D.O., M.J.S., G.W. and J.G. wrote the manuscript. The project was organized and coordinated by M.K. and J.G.

## Additional information

**Supplementary Information** accompanies this paper at http://www.nature.com/naturecommunications

**Competing financial interests:** The authors declare no competing financial interests.

**Reprints and permission** information is available online at http://npg.nature.com/reprintsandpermissions/

**How to cite this article:** Kreysing, M. *et al.* Dynamic operation of optical fibres beyond the single-mode regime facilitates the orientation of biological cells. *Nat. Commun.* 5:5481 doi: 10.1038/ncomms6481 (2014).
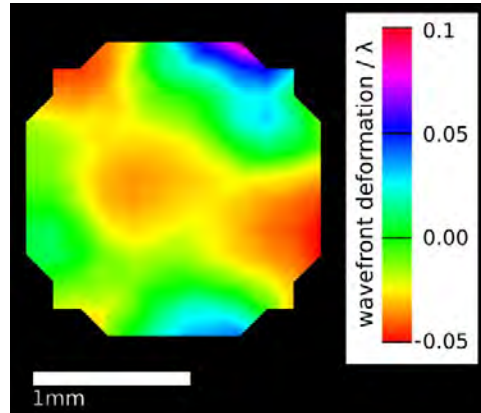
**Supplementary figure 1 | Wavefront correction.** Wavefront profile in the back focal plane of the coupling lens after alignment and minimization of residual aberrations, measured with a Shack-Hartman wavefront sensor. The route-mean-square deviation from a flat wavefront is below 0.025 λ.
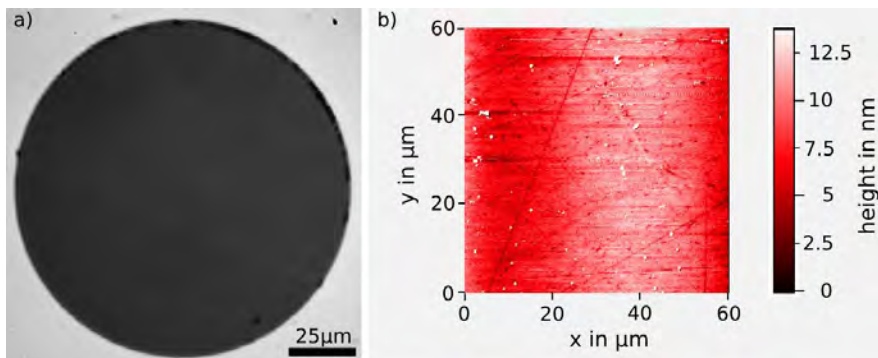


**Supplementary figure 2 | Polished fibre end-face.** Reflection light microscopy (a) and atomic force microscopy (b) images of typical polished fibre end-faces. The RMS roughness of the end face according to the AFM image was below 5 nm.
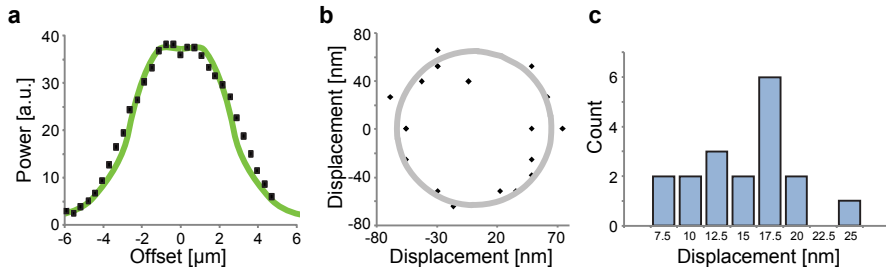
**Supplementary figure 3 | Optimisation of fibre coupling.** a) Laser power coupled into the few-mode fibre as a function of the lateral offset. b) Measurement of the deviation of the laser focus from the optical axis before fibre coupling due to the rotation of the polarization-adjusting half-wave plate. c) Radial distance of the laser foci from the ideal circular orbit resulting from the half-wave plate rotation shown in c). During the 30 min, which it took to obtain the measurement points shown in c), the real position of optimum coupling deviated slightly from the ideal orbit. The mean distance indicates an RMS centring stability of 13 nm over the 30 min.
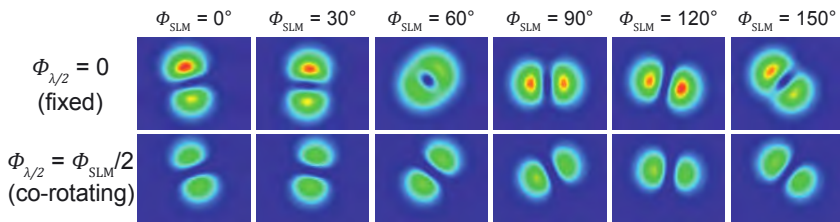


**Supplementary figure 4 | Influence of the polarization co-rotation during SLM-induced rotation of the LP11 mode.** Top row: Without co-rotation of the polarization using a half-wave plate a de-phasing of transverse electric and transverse magnetic fields is observed. Bottom row: With co-rotation of the half-wave plate the de-phasing is gone. Wavelength λ = 633 nm with Nufern 1060-XP fibre.
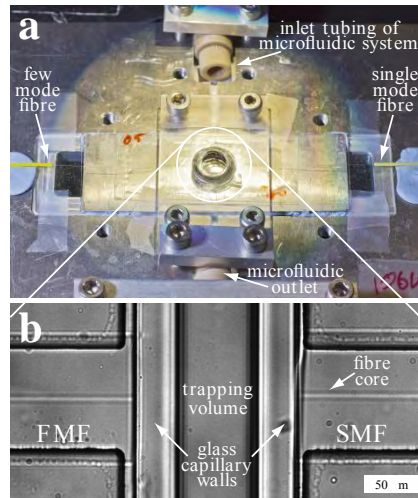
**Supplementary figure 5 | Experimental trapping setup.** a) Overview of the fibre alignment and the microfluidic capillary delivery system for the cell suspension on the microscope stage. b) Microscope image of the trapping region. The few-mode fibre (FMF) and the single-mode fibre (SMF) are coaxially aligned using an SU8-patterned surface (visible in the four corners). The fibre ends are moved onto the outer sides of a square glass micro-capillary, which runs perpendicularly from top to bottom.

# Nanoscale phase behavior on flat and curved membranes

**Thomas Andersen[1], Azra Bahadori[1], Dino Ott[1], Anders Kyrsting[1], S Nader S Reihani[1,2] and Poul M Bendix[1]**

[1] Niels Bohr Institute, University of Copenhagen, Blegdamsvej 17, DK-2100 Copenhagen, Denmark
[2] Department of Physics, Sharif University of Technology, Teheran 11365-9161, Iran

E-mail: bendix@nbi.dk

## Abstract

The diverse physical properties of membranes play a critical role in many membrane associated biological processes. Proteins responsible for membrane transport can be affected by the lateral membrane order and lateral segregation of proteins is often controlled by the preference of certain membrane anchors for membrane phases having a physically ordered state. The dynamic properties of coexisting membrane phases are often studied by investigating their thermal behavior. Optical trapping of gold nanoparticles is a useful tool to generate local phase transitions in membranes. The high local temperatures surrounding an irradiated gold nanoparticle can be used to melt a part of a giant unilamellar lipid vesicle (GUV) which is then imaged using phase sensitive fluorophores embedded within the bilayer. By local melting of GUVs we reveal how a protein-free, one component lipid bilayer can mediate passive transport of fluorescent molecules by localized and transient pore formation. Also, we show how tubular membrane curvatures can be generated by optical pulling from the melted region on the GUV. This will allow us to measure the effect of membrane curvature on the phase transition temperature.

S Online supplementary data available from stacks.iop.org/NANO/25/505101/mmedia

Keywords: nanoscale phase behavior, membrane curvature, membrane permeability, optical trapping, local phase transitions, optical heating, lipid tubes

(Some figures may appear in colour only in the online journal)

## 1. Introduction

Plasmonic heating resulting from irradiation of metal nanoparticles using resonant light has become a useful tool for localized thermal induction of heat in biological materials. There are huge prospects for this technique in photothermal therapy [1], but also for investigation of thermal effects at the molecular level on specific heat sensing proteins [2] or the exploration of local heat effects on membranes [3, 4]. The thermal properties of membranes have been studied for decades and only recently has it become possible to experimentally probe the thermal response of a membrane to a local heat gradient using optical trapping of metal nanoparticles as heat probes [3–6]. Such an experimental assay provides a tool to investigate recent theoretical predictions regarding the behavior of biological systems existing within temperature gradients [7].

Membrane permeability is well known to be enhanced during the main melting transition of lipid bilayers [8–10]. However, little is known about the nature and mechanism of this leakage. Measurements have so far been performed using electrical conductance measurements across flat black lipid membranes (BLMs) [11, 12]. BLMs can contain remnants of organic solvents used in the formation process which can potentially influence the results. Fluorescence permeability measurements have so far not confirmed the discrete events detected in electrical BLM measurements. One reason for this could be that transient fluorescent signals from permeability measurements are difficult to detect due to the rapid diffusion and consequent dilution of dyes.
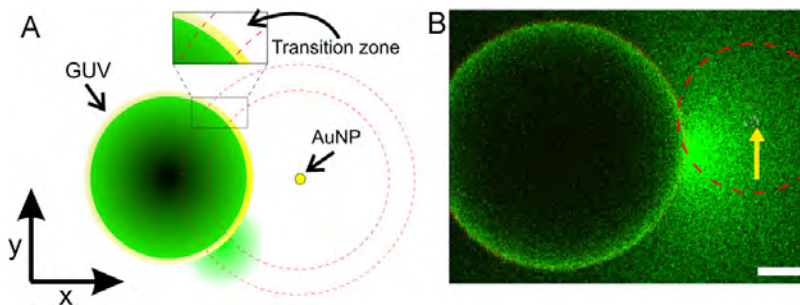
**Figure 1.** Setting up coexisting fluid and gel phases on a single GUV for studying membrane permeability. (A) Schematic depiction of an optically trapped $d = 80$ nm AuNP close to a GUV made from $DC_{15}PC$ which is gently adhered to a passivated glass surface. The GUV has a phase transition temperature of $T_m = 33\,°C$. The region within the annular ring corresponds to the membrane area that exists within the transition region ($\Delta T \sim 1\,°C$). The GUV stays in gel phase further away whereas the proximal part of the GUV is fluid. A leakage of calcein dye (green hazy disk) is depicted centered on the surface of the GUV. (B) Data showing detection of a leakage event. During leakage the calcein dilutes and de-quenches to yield a powerful burst in intensity. The red dashed circle marks a melting distance within the annular ring also depicted in (A). The scale bar is 5 $\mu$m.

Here we show how membrane permeability can be measured using fluorescence in conjunction with localized heating of GUVs using an optically trapped gold nanoparticle (AuNP). The fluorescent assay includes self-quenched calcein within the GUVs which dequenches during permeation across the GUV membrane and consequently gives a powerful burst in intensity that lasts up to a few seconds depending on the life-time of the pore event [4]. By using membrane incorporated phase sensitive dyes we can clearly visualize the melted region and confirm that melting actually takes place within the membrane.

We demonstrate the versatility of this assay and show how membrane tubes can be pulled from the fluid part of the membrane by combining optical heating with optical pulling in a dual trap system. This assay will provide the possibility to regulate the curvature and membrane phase within the same GUV and hence the effect of curvature on the membrane phase transition temperature can be investigated. Finally, we show how a local liquid disordered phase can be established on a tube pulled from a GUV existing in a liquid ordered phase, thus creating phase domain interfaces on a highly curved bilayer without fissioning of the tube.

## 2. Results

### 2.1. Localized melting of GUVs

Giant unilamellar lipid vesicles (GUVs) composed of $DC_{15}PC$ ($T_m = 33\,°C$) were locally heated using optically trapped AuNPs with a diameter of 80 nm. By changing the distance between the GUV and the nanoparticle, a transition zone was established on the GUV which allowed us to study permeability, as shown in figure 1.

As a reporter for permeability changes and phase changes within the GUV membrane we use the aqueous dye calcein and two different phase sensitive fluorescent markers: laurdan and di-4-ANEPPDHQ, respectively. Calcein, which was used

for detecting bilayer permeation, was encapsulated at self-quenched concentrations (up to 80 mM) but with significant variability in the encapsulation efficiency among the different GUVs. A typical image of the variability in encapsulation efficiency is shown in figure 2(A). GUVs containing calcein at self-quenched concentrations have a characteristic dark center region surrounded by a brighter peripheral region. The dark regions are caused by attenuation of excitation light due to absorption as it travels through the lumen of the GUV containing high concentrations of absorbing calcein. This effect is less pronounced at the peripheral regions due to the curvature of the GUVs.

To visualize the fluid region of a gel phase GUV we used the potentiometric dye, di-4-ANEPPDHQ, which incorporates predominantly into more disordered domains of GUVs [4, 13], as shown in figure 2(B). We did not measure a significant incorporation of the dye into the gel phase but found that the fluorophore incorporated directly from solution into the disordered fluid phase.

Lipid bilayers exhibit radically different hydration levels in gel and fluid phases [15]. To verify that the locally heated region as shown in figure 2(B) is in fact in fluid phase we measured the degree of hydration using laurdan which senses the hydration level of the bilayer. Laurdan exhibits a 50 nm spectral red shift in non-polar versus polar environments [15]. Since laurdan does not exhibit lateral partitioning it is possible to measure the spectral shift by quantifying the relative intensities from the spectral regions defined as: $I_{420-460}$ ($I_B$) and $I_{461-530}$ ($I_R$) respectively. In gel phase laurdan will predominantly emit in the region from 420–460 nm whereas in fluid phase the laurdan emission will red shift leading to an increased intensity in the wavelength interval 461–530 nm. This can be expressed as a single parameter called the generalized polarization $G_P$

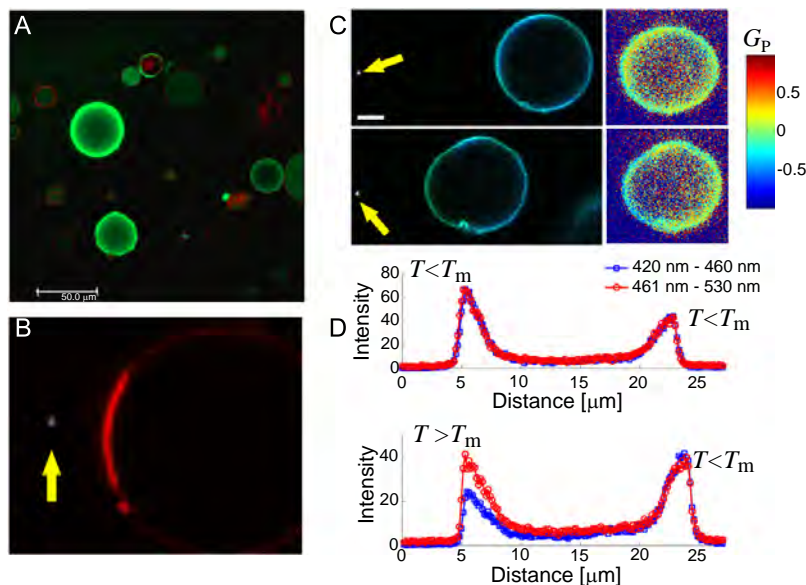$$G_P = \frac{I_B - I_R}{I_B + I_R}. \tag{1}$$

**Figure 2.** Fluorescent markers used for detecting permeability and co-existing phases originating from local heating. (A) Encapsulation of calcein within GUVs at self-quenching concentrations (maximum concentration, $c = 80$ mM). A dark region surrounded by a bright intensity indicates a high degree of self-quenching. GUVs containing variable concentrations of calcein, as well as multilamellar vesicles and lipid-aggregates are seen in the sample chamber. GUVs are labeled with the red membrane dye TR-DHPE. (B) Clear visualization of the extent of the fluid phase using di-4-ANEPPDHQ (red color) which strongly partitions into the fluid phase. (C) The environmentally sensitive fluorescent dye laurdan reveals the level of hydration within the bilayer. Top images show a GUV in gel phase at $T \sim 25$ °C (scale bar is 5 $\mu$m). Bottom images show a GUV which is locally melted. The top and bottom right images show a plot of the $G_p$ values based on equation (3). The melted region has lower $G_p$ values than the region which is still in gel phase thus revealing the increased level of hydration which is a signature of the fluid phase. (D) A line scan across the GUV at $T \sim 25$ °C (upper figure) and after local melting of the GUV (lower figure). The intensities in the two channels are shown by the blue squares ($I_B$) and red circles ($I_R$), respectively.

The $G_P$ value is thus a normalized range of values between 1 to −1 with smaller and negative values indicating deeper hydration of the bilayer and hence more fluid bilayers.

We measured the spectral shift of laurdan while translating a hot AuNP gradually closer to a GUV that was initially in the gel phase, as shown in the overlay in figure 2(C) (left panels). Initially the $G_p$ values of the GUV are close to 0 (see figure 2(C), upper right) but as the AuNP approaches the left side of the GUV a clear shift can be detected towards lower $G_p$ values on the left side of the GUV, see lower right panel in figure 2(C), thus verifying that the bilayer is indeed becoming more fluid. A quantification of the relative intensities within the intervals, $I_B$ and $I_R$ is shown in figure 2(D) as an average line scan (70 pixel lines) across the GUV before (upper panel) and after heating (lower panel). After local heating of the left side of the GUV a decrease is measured for the intensity in both channels but the decrease is more significant in the blue intensity channel, $I_B$, revealing that the bilayer has become more fluid.

### 2.2. Membrane pores exist in melting GUVs

Membranes undergoing a phase transition exhibit an anomalous high permeability which is thought to occur at the interface between co-existing gel and fluid nanodomains in melting membranes. We investigated the nature of this permeability by locally melting GUVs, containing self-quenching concentrations of calcein dye, by using the experimental setup depicted in figure 1. When the gel phase GUVs were locally heated above the phase transition temperature, $T_m$, we measured transient and local efflux of the calcein which was detected as a local burst in intensity, see figure 3(A). The pores were transient as could be verified by quantifying the intensity over time at a fixed distance away from the GUV, see figure 3(B). The intensity in figure 3(B) shows an initial increase followed by decay in intensity, thus indicating that the pore has closed. By comparing data, as shown in figure 3(B), with the expected concentration of molecules predicted from Fick's second law of diffusion for an instantaneous point source, we have previously shown that the pore lifetimes of these events were on the order of 100 ms [4].

### 2.3. Pulling membrane tubes from melted regions

Pulling of membrane tubes from GUVs has been previously used for studying effects related to membrane curvatures. Membrane tubes are readily formed from fluid phase GUVs and together with micropipette aspiration for regulating the
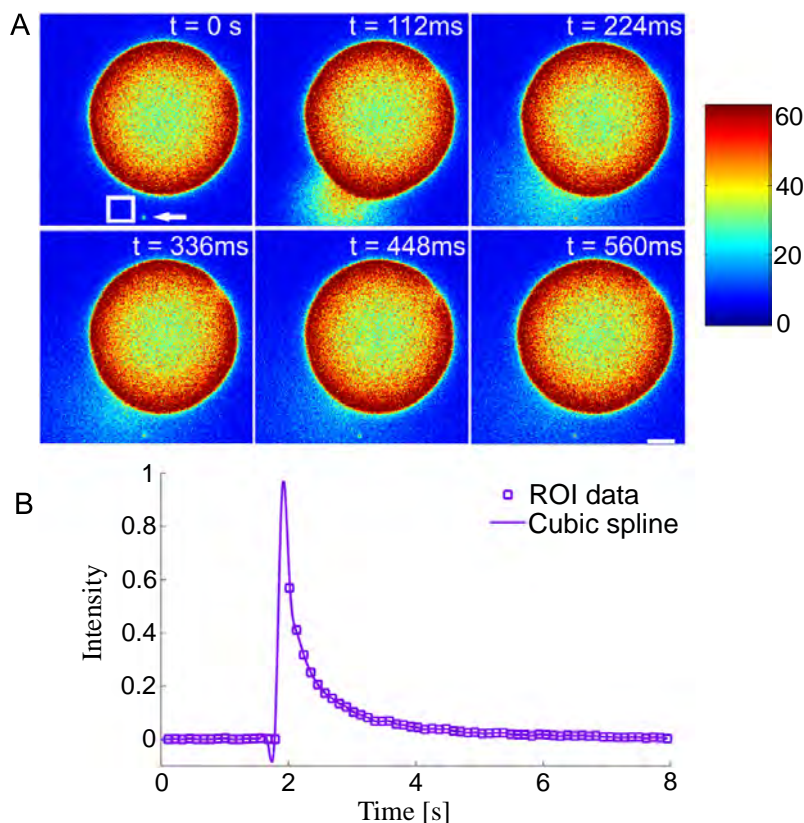
**Figure 3.** Transient and local permeability detected in a locally melted GUV. (A) Image sequence showing the dilution and de-quenching of calcein due to a local pore formation in the GUV membrane. The location of the optically trapped gold nanoparticle is indicated in the first image by a white arrow. Scale bar is 5 $\mu$m. (B) The intensity is quantified within a ROI positioned 5 $\mu$m away from the transient pore on the GUV. The position of the ROI and AuNP is indicated by the square and arrow, respectively, in the first image of figure 3(A). The single peak indicates a single and transient pore formation in the GUV membrane.

membrane tension it is possible to obtain tubes with a spectrum of curvatures on which curvature sensing of protein binding can be investigated [16]. However, due to the rigidity of the gel phase it has not, until now, been possible to extract tubes from gel phase GUVs. The force needed to hold a membrane tube is given by [2]

$$f = 2\pi\sqrt{2\sigma\kappa} \;, \qquad (2)$$

where $\sigma$ is the membrane tension and $\kappa$ is the bending rigidity of the membrane. $\kappa$ has been measured for gel phase bilayers to be 57 $K_BT$ (KB is the Boltzmann's constant) for DPPC bilayers [17] whereas $\sigma$ depends on osmotic pressure and the relative expansion of the bilayer due to aspiration or surface adhesion. According to equation (2) the force at a tension of e.g., $\sigma = 0.02$ mN m$^{-1}$, will be $\sim$19 pN, however it is well known that tube formation also involves a barrier for formation which scales with the size of the adhesion patch between the particle and the membrane [21]. This barrier can

easily reach tens of pN for fluid phase GUVs and for gel phase GUVs this barrier can be higher than what optical tweezers typically can deliver ($f_{max} \sim 200$ pN).

We therefore pulled membrane nanotubes from the fluid part of GUVs that were locally melted using a hot AuNP as shown schematically in figure 4(A). By combining optical heating (figure 4(B)) with optical pulling we could locally melt a GUV using an optically trapped AuNP and subsequently use a second trap to pull a membrane nanotube using a 4.95 $\mu$m polystyrene bead as shown in figure 4(A). The polystyrene bead was conjugated with streptavidin and the GUV contained a low fraction of biotinylated lipids to facilitate specific binding. The melted region was visualized by di-4-ANEPPDHQ (see figure 4(C)) and the nanotube was extruded from this region to a length exceeding 10 $\mu$m. In figure 4(D) we also used Texas Red DHPE (TR-DHPE) to show a more uniform labeling of the GUV and tube membrane. Although TR-DHPE has a preference for fluid regions
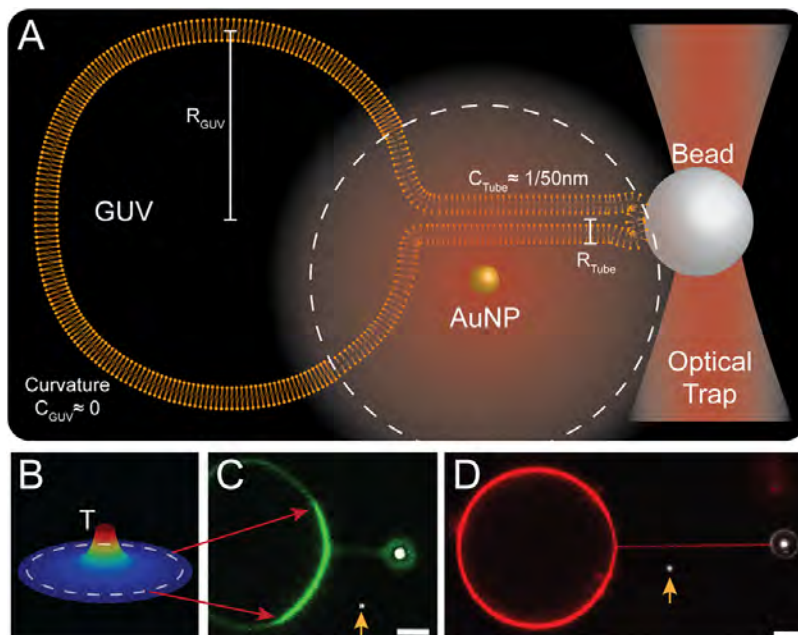
4

**Figure 4.** Tube pulling from local fluid regions within gel phase GUVs allows for studying membrane curvature effects on phase transitions. (A) Schematic diagram of tube pulling. An optically trapped AuNP is used to generate a fluid phase on the GUV and subsequently another trap holding a $d = 4.95\ \mu$m streptavidin coated polystyrene bead is used to pull out a membrane tether with $d \sim 100$ nm and thus with a curvature of $C \sim 1/50$ nm$^{-1}$. The curvature of the GUV was typically three orders of magnitude lower, thus $C \sim 0$ nm$^{-1}$. (B) The profile of the heating zone generated by the irradiated AuNP. The dashed circle in (A) and (B) marks the distance from the AuNP where the temperature equals the phase transition temperature, $T_m = 33\ °$C of the lipids. (C) Membrane tether and fluid region are imaged using di-4-ANEPPDHQ. The arrow indicates the location of the optically trapped AuNP. Scale bar is 5 $\mu$m. (D) Imaging of the membrane tether and GUV system using the Texas Red DHPE lipid dye. The yellow arrow indicates the location of the optically trapped AuNP. The tube could be extended such that the temperature at the tip region was below $T_m$, indicating that curvature affects the melting point of the tether. Scale bar is 5 $\mu$m.

it does not exhibit lateral partitioning on short time scales since the fluorophore exhibits very low mobility in the gel phase.

During nanotube extrusion we measure a uniform tube radius along the whole tube strongly indicating that the whole tube is in the same phase. Tube radius, $R$, membrane bending rigidity, $\kappa$, and membrane tension, $\sigma$, are related by

$$R = \sqrt{\frac{\kappa}{2\sigma}}. \qquad (3)$$

Since membranes are significantly stiffer in gel phase than in fluid phase we would expect that co-existing phases on the tube would have different radii. However, as shown in figure 4(D), the tube radius stays relatively constant even though the end of the tube reaches a distance where the temperature is lower than the phase transition temperature. Occasionally, when long tubes are pulled we observe fission events which might be due to the onset of a tubular transition. Future studies will show if an actual phase boundary induced by a temperature gradient can be established on a tube made from DC$_{15}$PC without fissioning of the tube.

The effect of curvature on membrane phase transitions has been shown in bulk to result in lower melting

temperatures for highly curved bilayers [18]. The lower melting transition can be rationalized in terms of outer leaflet lateral stress upon significant bending of the membrane. Future experiments will address the effect of curvature on the transition temperature for membrane tubes and our aim is to explore the effect of inducing local transitions which could, as mentioned above, well lead to fission of the tube due to the discontinuities between the elastic constants between the two co-existing phases [19].

### 2.4. Thermal regulation of tube diameter

In traditional GUV/tube experiments the nanoscale diameter is regulated by controlling the membrane tension through an aspiration pipette [16]. However, temperature can also be employed for changing the tube diameter simply by regulating the laser power of the optical trap holding the gold nanoparticle, see figure 5(A). Initially, a substantial part of the GUV is melted by the heated gold nanoparticle (first image in figure 5(A)) and by successively decreasing the laser power, and hence the heating, we measure a decrease in the tube intensity (figure 5(B)) which is linearly related to the tube diameter. We note that the dye used in the experiment in
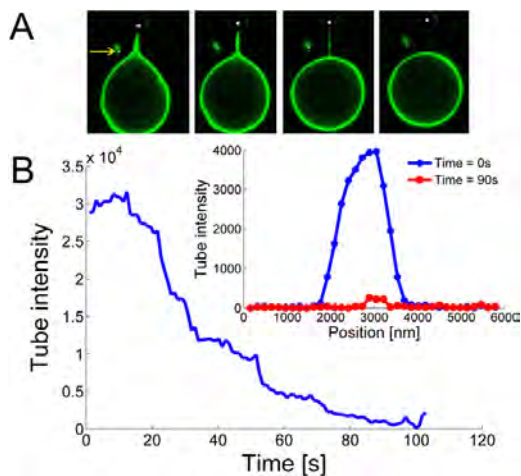
**Figure 5.** Variation of tube diameter with temperature. (A) Optical trapping of a gold nanoparticle (arrow) at decreasing laser powers results in a decrease in the tube intensity which is proportional to the tube diameter. See also supplementary movie 1. The GUV is labeled with TR-DHPE which does not partition notably between phases for this lipid mixture. (B) Quantification of the intensity as a function of time. The steps which are barely detectable in the curve correspond to sudden changes in laser power. Inset, intensity profile across the lipid tube, at $t = 0$ s (blue curve) and at $t = 90$ s (red curve).

figure 5 (TR-DHPE) does not partition between the gel and fluid phase on the time scale of this experiment and therefore we can assume a linear dependence between intensity and tube radius. An intensity profile across the initial and final tube in the inset of figure 5(B) reveals a substantial decrease in tube diameter. When the laser power is sufficiently low we observe fission of the tube as shown in supplementary information movie 1, available at stacks.iop.org/NANO/25/505101/mmedia.

A change in tube diameter can be rationalized by looking at the dependence of the radius on the bending rigidity as given in equation (3). The bending rigidity in equation (3) has been shown to change orders of magnitudes with small temperature changes (<1 °C) close to the phase transition temperature of $DC_{14}PC$ lipid bilayers [14]. Therefore, we also expect significant changes to the radius of the tube according to equation (3) for similar lipid bilayers made from $DC_{15}PC$. Near $T_m$ the lipid bilayer becomes extremely soft and the tube becomes consequently thinner and eventually fissions due to high curvature stress. We also note that membrane tension regulates tube radius through equation (3) and that the membrane tension does increase during cooling of the GUV/ tube system in figure 5 due to a significant shrinkage of membranes during the fluid-to-gel transition.

### 2.5. Nanoscale domains by local heating of tubes

We also show how local membrane transitions can be established on lipid tubes made from more complex mixtures of lipids. Ternary mixtures of cholesterol, DPPC and DOPC
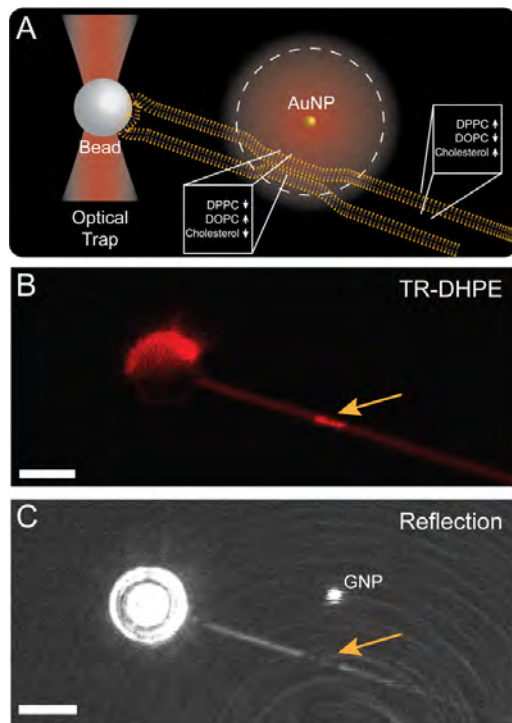


**Figure 6.** Local phase transition generated on a lipid tube pulled from a liquid ordered phase existing on a GUV made from DOPC, DPPC and cholesterol. (A) Schematic depiction of the experiment showing a local liquid disordered ($l_d$) phase being generated on a liquid ordered phase ($l_o$). The $l_o$ phase is enriched in cholesterol whereas the $l_d$ phase contains more unsaturated lipids (DOPC). (B) Local heating near a lipid tube results in transformation of the membrane from $l_o$ phase to $l_d$ phase (arrow) and a consequent enrichment of TR-DHPE in the nanoscale $l_d$ phase. (C) Reflection image of the same tube as in (B). The black region corresponds to less reflection due to a smaller tube radius which is consistent with the fact that $l_d$ phase has significantly lower bending rigidity than the $l_o$ phase and hence forms thinner tubes according to equation (3). The bright spots are the trapped polystyrene particle and gold nanoparticle (GNP) respectively. Scale bars in (B) and (C) are 5 $\mu$m.

can form GUVs containing two fluid phases with different order which are not as mechanically different as the gel and fluid phases presented in figure 4. In figure 6, a lipid tube is pulled from a GUV composed from a ternary mixture of DOPC, DPPC and cholesterol which contains co-existing phases of liquid ordered ($l_o$) and liquid disordered ($l_d$) phases labeled with TR-DHPE which partitions strongly into the ($l_d$) phase. A tube is pulled from the $l_o$ phase and subsequent local heating of the tube reveals a melting transition on the tube. The increase in intensity in figure 6(B) results from the partitioning of TR-DHPE dye into the $l_d$ phase but imaging of the tube in reflection mode [20] (figure 6(C)) reveals a dark region, with no detectable reflection light, which shows that the tube in fact becomes thinner at the region where local

melting occurs. This is consistent with the fact that the tube becomes fluid and hence attains a lower bending rigidity and consequently a smaller radius according to equation (3).

## 3. Conclusion

We have shown how local heating can be applied to investigate the physical properties of membranes. A locally induced membrane phase transition led to transient and local permeation of encapsulated calcein molecules which was detected as de-quenching of calcein as it left the interior of the GUV. The local phase change resulting from the heat gradient, established by the irradiated AuNP, was visualized by environmentally sensitive fluorophores that either selectively partition into the fluid phase or exhibit a spectral shift upon melting. Finally, this assay will allow further investigation of the interplay between curvature and phase transitions by performing local melting on lipid tubes pulled from GUVs being initially in an ordered phase.

## 4. Materials and methods

### 4.1. Sample preparation

GUVs were formed by using a standard electroformation device (Nanion Technologies, Germany). A lipid film was formed on an ITO coated glass slide and hydration was performed at $T = 50\,°C$ which ensured that GUVs were formed above the phase transition temperature, $T_m = 33\,°C$. The hydration solution contained either 600 mM sucrose (permeability experiments) or 300 mM sucrose (tube experiments). The GUVs were composed of 1,2-dipentadecanoyl-*sn*-glycero-3-phosphocholine (Avanti Polar Lipids, 850 350) and 0.3 mol% 1,2-dihexadecanoyl-*sn*-glycero-3-phosphoethanolamine, triethylammonium salt (Invitrogen, T1395MP, Texas Red DHPE) to label the vesicle membrane. Encapsulation of calcein within the GUVs was achieved by incubating 85 mM calcein (Invitrogen, C481) solution (adjusted to pH = 7.2 using NaOH) with GUVs briefly at the phase transition temperature ($T_m = 33\,°C$) or alternatively in the fridge at 5 °C for >12 h. For imaging the fluid part of the GUV we used 1 mol% di-4-ANEPPDHQ (Invitrogen, D36802). The relative hydration level of the membrane was measured by including 0.5 mol% laurdan (Invitrogen, D250) in the lipid mixture. The three dyes were used in separate experiments and were premixed with the lipids in chloroform. After the formation of the GUVs we noticed that the phase sensitive dye di-4-ANEPPDHQ does strongly partition into the solution when the GUVs were incubated below the phase transition temperature. However, after melting the GUV locally, the dye (which has a very low quantum yield in solution) strongly partitioned into the fluid phase of the GUV. In permeability experiments, the GUVs were allowed to settle on a clean glass coverslip, passivated with BSA or $\alpha$-casein (Sigma Aldrich), in a solution that was iso-osmolar with the inside solute concentration (calcein, sucrose and NaOH). The remaining

dye was carefully diluted from the sample by pipetting. In the permeability experiments 300 mM NaCl was used to balance the osmotic pressure from the interior solution. AuNPs ($d = 80\,nm$) were purchased from British Biocell International (British Biocell International, BBI). Tubes were pulled by using streptavidin coated polystyrene beads, purchased from Bangs Laboratories, with a diameter of 4.95 $\mu m$.

### 4.2. Experimental setup

The setup included a dual optical trapping system ($\lambda = 1064\,nm$, Spectra Physics J201-BL-106C) coupled into a confocal fluorescence microscope (Leica SP5) equipped with a water immersion objective (Leica, PL APO NA: 1.2, 63×) and a piezo electric stage for translating the sample (PI 731.20, Physik Instrumente, Germany). One of the laser traps could be controlled by a piezo mirror (Mad City Labs) allowing a trapped AuNP to be positioned near the GUV or near the membrane nanotube. In the permeability assay we continuously decreased the distance between the AuNP and the GUV at 100 nm s$^{-1}$. AuNPs were imaged using an argon laser line ($\lambda = 514\,nm$) and by collecting the backscattered light using an acousto optical beam splitter [20]. Excitation of calcein and di-4-ANEPPDHQ was performed at $\lambda = 488\,nm$ and TR-DHPE was excited at $\lambda = 594\,nm$. Fluorescent and scattered light was collected using photomultiplier tubes. Laurdan was excited at $\lambda = 405\,nm$ and the emission light was collected using a HyD detector installed on the SP5 Leica confocal system. Calcein plumes were recorded at 112 ms time resolution to capture the dynamics of the permeation events.

### 4.3. Data analysis

All data and image analysis was done in Matlab using the Image Processing Toolbox.

## Acknowledgments

## References

[1] Huang X *et al* 2006 Cancer cell imaging and photothermal therapy in the near-infrared region by using gold nanorods *J. Am. Chem. Soc.* **128** 2115–20

[2] Huang H *et al* 2010 Remote control of ion channels and neurons through magnetic-field heating of nanoparticles *Nat. Nanotechnology* **5** 602–6

[3] Bendix P M *et al* 2014 Optical trapping of nanoparticles and quantum dots *IEEE J. Sel. Top. Quantum Electron.* **20** 4800112

[4] Andersen T, Kyrsting A and Bendix P M 2014 Local and transient permeation events are associated with local melting of giant liposomes *Soft Matter* **10** 4268–74

[5] Kyrsting A *et al* 2011 Heat profiling of three-dimensionally optically trapped gold nanoparticles using vesicle cargo release *Nano Lett.* **11** 888–92

[6] Bendix P M, Reihani S N and Oddershede L B 2010 Direct measurements of heating by electromagnetically trapped gold nanoparticles on supported lipid bilayers *ACS Nano* **4** 2256–62

[7] Atia L and Givli S 2014 A theoretical study of biological membrane response to temperature gradients at the single-cell level *J. R. Soc. Interface* **11** 20131207

[8] Mouritsen O G and Zuckermann M J 1985 Softening of lipid bilayers *Eur. Biophys. J.* **12** 75–86

[9] Papahadjopoulos D *et al* 1973 Phase transitions in phospholipid vesicles. Fluorescence polarization and permeability measurements concerning the effect of temperature and cholesterol *Biochim. Biophys. Acta* **311** 330–48

[10] Cisse I *et al* 2007 Fueling protein DNA interactions inside porous nanocontainers *Proc. Natl Acad. Sci. USA* **104** 12646–50

[11] Blicher A *et al* 2009 The temperature dependence of lipid membrane permeability, its quantized nature, and the influence of anesthetics *Biophys. J.* **96** 4581–91

[12] Antonov V F *et al* 2005 Soft perforation of planar bilayer lipid membranes of dipalmitoylphosphatidylcholine at the temperature of the phase transition from the liquid crystalline to the gel state *Eur. Biophys. J.* **34** 155–62

[13] Jin L *et al* 2006 Characterization and application of a new optical probe for membrane lipid domains *Biophys. J.* **90** 2563–75

[14] Dimova R, Pouligny B and Dietrich C 2000 Pretransitional effects in dimyristoylphosphatidylcholine vesicle membranes: optical dynamometry study *Biophys. J.* **79** 340–56

[15] Sezgin E *et al* 2012 Elucidating membrane structure and protein behavior using giant plasma membrane vesicles *Nat. Protocols* **7** 1042–51

[16] Ramesh P *et al* 2013 FBAR syndapin 1 recognizes and stabilizes highly curved tubular membranes in a concentration dependent manner *Sci. Rep.* **3** 1565

[17] Picas L, Rico F and Scheuring S 2012 Direct measurement of the mechanical properties of lipid phases in supported bilayers *Biophys. J.* **102** L01–03

[18] Nagano H *et al* 1995 Effect of vesicle size on the heat capacity anomaly at the gel to liquid-crystalline phase transition in unilamellar vesicles of dimyristoylphosphatidylcholine *Phys. Rev.* E **52** 4244–50

[19] Allain J M *et al* 2004 Fission of a multiphase membrane tube *Phys. Rev. Lett.* **93** 158104

[20] Bosanac L *et al* 2008 Efficient optical trapping and visualization of silver nanoparticles *Nano Lett.* **8** 1486–91

[21] Kaster G, Cacciuto A, Derényi I, Frenkel D and Dogterom M 2005 Force barriers for membrane tube formation *Phys. Rev. Lett.* **94** 068101

# Enabling accurate photodiode detection of multiple optical traps by spatial filtering

Dino Ott[a], S. Nader S. Reihani[b], and Lene B. Oddershede[a]

[a]Niels Bohr Institute (NBI), University of Copenhagen, Blegdamsvej 17, DK-2100 Copenhagen, Denmark;
[b]Department of Physics, Sharif University of Technology, 11369-9161, Tehran, Iran

## ABSTRACT

Dual and multiple beam optical tweezers allow for advanced trapping geometries beyond single traps, however, these increased manipulation capabilities, usually complicate the detection of position and force. The accuracy of position and force measurements is often compromised by crosstalk between the detected signals, this crosstalk leading to a systematic error on the measured forces and distances. In dual-beam optical trapping setups, the two traps are typically orthogonal polarized and crosstalk can be minimized by inserting polarization optics in front of the detector, however, this method is not perfect because of the de-polarization of the trapping beam introduced by the required high numerical aperture optics. Moreover, the restriction to two orthogonal polarisation states limits the number of detectable traps to two. Here, we present an easy-to-implement simple method to efficiently eliminate cross-talk in dual beam setups.[1] The technique is based on spatial filtering and is highly compatible with standard back-focal-plane photodiode based detection. The reported method significantly improves the accuracy of force-distance measurements, e.g., of single molecules, hence providing much more scientific value for the experimental efforts. Furthermore, it opens the possibility for fast and simultaneous photodiode based detection of multiple holographically generated optical traps.

**Keywords:** Optical tweezers, Detection, Photodiodes, Crosstalk, Spatial filtering, Signal processing, Optical manipulation

## 1. INTRODUCTION

Since the invention of single-beam optical tweezers,[2] numerous extensions[3,4] and completely new generations of optical tweezers[5–7] have been presented. These innovations broadened the manipulation capabilities and paved the way for break-through experiments within biophysics.[8,9] One particularly successful technique within single molecule biophysics are dual-beam optical tweezers, as these double traps allow for the manipulation of the two ends of linear molecules by using two trapped beads as handles.[10]

Dual-beam optical traps can conveniently be generated by using two laser beams with perpendicular polarization. Using beams in different polarisation states has advantages both for beam generation and detection. For beam steering control, the optical paths for the two beams can be split by polarization optics like, e.g., polarizing beam splitters, allowing for individual positioning of the two traps. On the detection side, polarisation optics can again be used to separate the signals, originating from the two individual traps, for separate detection using photodiodes.

However, one problem, that has often been overlooked, is that signal separation techniques based on polarization do not allow for a complete signal separation. This is mainly due to the use of high numerical aperture optics, which are required for efficient optical trapping and which unfortunately cause de-polarisation. Moreover, polarisation optics are not perfect. E.g., polarizing beam splitting cubes typically have an extinction ratio of only 1:100 for the reflected beam. This incomplete separation of signals leads to a systematic error called crosstalk. Crosstalk in dual-beam optical tweezers means that one detector is not measuring exclusively the signal from one trap, but a small fraction of the light from the other trap is also being detected. Crosstalk thus results into

---

Email of corresponding author: oddershede@nbi.dk

measuring partly the position and force acting on the second bead, when the aim is to exclusively measure the position and force acting on the first bead.

Recently, a few different methods have been presented which tackle this problem and vary in complexity, cost and efficiency.[11–13] Here we contribute to this topic by presenting a simple and easy-to-implement method that can be used in combination with polarisation based signal separation.[1] The method is based on spatial filtering and allows for reduced crosstalk levels as low as 0.2%, i.e., an improvement compared to the standard technique by a factor five. Moreover, the presented signal separation technique can be advantageously used for enabling fast and accurate detection by photodiodes in holographically generated traps, where traditionally cameras had to be used for detection, since a separation of multiple signals based on polarisation is not possible.

## 2. OPTICAL SETUP

### 2.1 Trapping Setup

Dual-beam optical tweezers in orthogonal polarisations were integrated into an inverted microscope (Leica DM IRBE) in the standard way.[14] Briefly, the linear polarized beam from a 1064nm CW laser (Spectra Physics J20I-BL-106C-02) was expanded to slightly overfill the back aperture of the objective (63X, NA=1.2, Leica HCX PL APO W CORR CS). Using a half-wave plate in combination with a polarizing beam splitter, this initial beam was split in a 50:50-ratio to generate two separate trapping beams. Beam steering capabilities were added to one of the trapping beams by means of a 1:1-telescope. The optical plane of the telescope's first lens, the 'steering lens', was optically conjugated with the back-focal-plane of the objective. In this arrangement, lateral displacement of the steering lens via piezo actuators (Newport Picomotor, 9066-X-P-M) resulted in lateral displacement of the trap focus. The two trapping beams were recombined using a second polarizing beam splitter and sent into the objective to form the two optical tweezers in the objective's focal plane. The trap foci were optimized by adjusting the objective collar to compensate for spherical aberration.[15]

As a generic sample, we mounted a perfusion chamber, formed by two #1.5 cover slips separated by double-sided sticky tape and filled with a dilute suspension of $0.96\mu$m polystyrene beads (PS03N/9396, Bangs Laboratories) in Millipore water.

### 2.2 QPD detection using spatial filtering

For the interferometric, photodiode based position detection, a relay lens was used to image the back-focal-plane of the light-collecting condenser onto a quadrant photodiode (QPD) (Si-PIN photodiode, Hamamatsu S5981).[16] As the only modification to this standard detection, we added a pinhole in a plane that was conjugate to the sample plane. In a manner similar to confocal detection in microscopy, this added element restricts the imaging volume, i.e., the volume in the sample chamber from where light can reach the detector. Using xyz-micropositioners, the pinhole was positioned in this conjugate plane, where an image of the sample plane was formed, such that only light originating from one trap of interest could pass though the pinhole to the QPD, while the light from the second trap was blocked (Fig. 1A-C). This small addition to the optical system effectively suppresses crosstalk without the requirement of a specific polarisation.

## 3. RESULTS

### 3.0.1 Crosstalk suppression

After alignment of the pinhole to the trap of interest, we were able to measure the time-dependent position and the power spectrum of the trapped bead (Fig. 1E and 1F). Scanning a bead that was attached to the surface of the cover glass through the trap focus confirmed that the linear relation between bead position and QPD signal remained valid (Fig. 1D). This linear relation facilitates an easy calibration procedure due to a constant conversion factor between the travelled distance, measured in metre, and the photodiode voltage signal for small displacements of the bead from its equilibrium position.

Next, we investigated the crosstalk suppression due to spatial filtering. We used the quantity

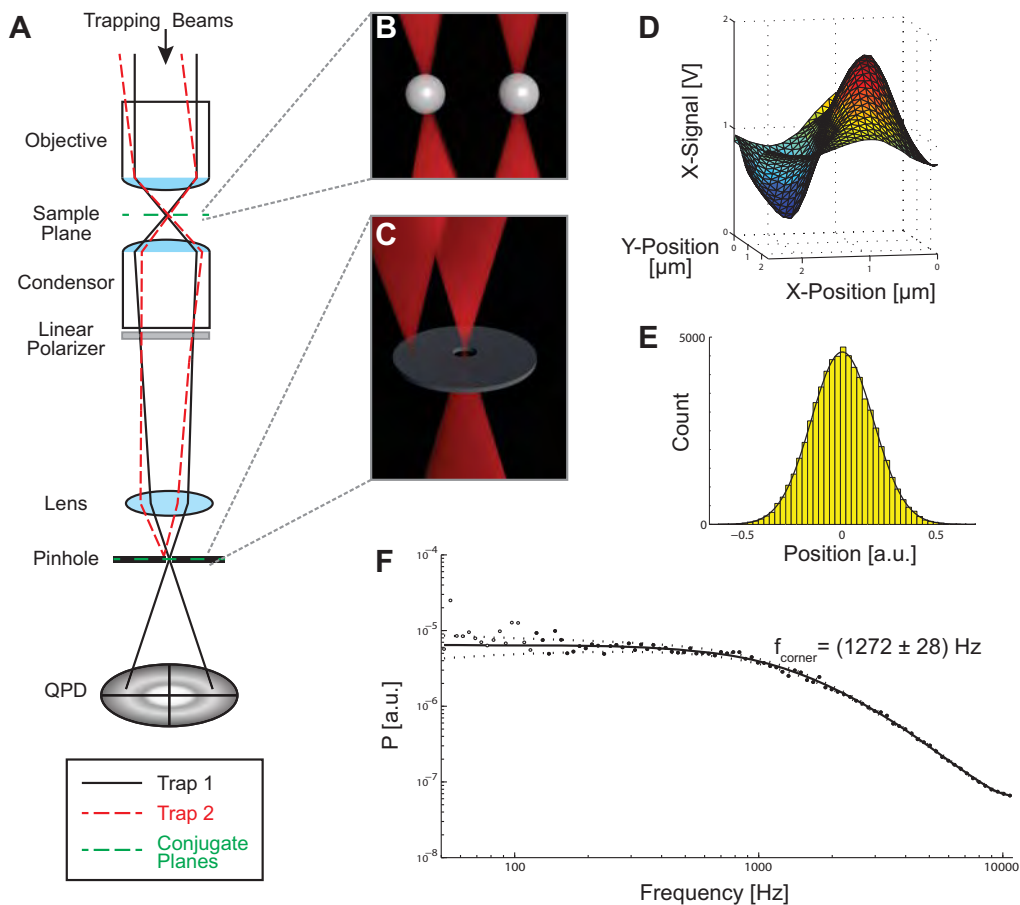$$\Psi = \frac{S_{\text{parasitic}}}{S_{\text{total}}}, \qquad (1)$$

Figure 1. Dual-beam optical tweezers with photodiode based detection and signal separation by spatial filtering. A) Two trapping beams enter the objective and generate two optical traps in the sample plane. A condenser collects the light for QPD detection and a relay lens images the back-focal-plane of the condenser onto the QPD. Selective transmission of light is achieved by placing a pinhole in a plane that is conjugate to the sample plane. B) Illustration of the sample plane where two beads are trapped. C) Illustration of the conjugate plane where the pinhole is located. Only light originating from one trap of interest can reach the QPD. D) Relation between lateral bead position and QPD signal. The graph shows the QPD output voltage for the X-channel, while a bead was raster-scanned through the focus. The signal shows a minor dependence on y-displacement and a linear relation between x-displacement and the output voltage of the QPD x-channel, confirming a constant conversion factor for small bead displacements. E) Position histogram with Gaussian fit. F) Power spectrum of the captured time-series. The corner frequency $f_{corner}$ was determined by a Lorentzian fit to the data (black dots). The fit is shown as solid black line with $\pm 1$ standard deviation (dotted lines). Empty dots are data points outside the fitting range. Data analysis was done using the freely available power spectrum analysis tool by Hansen et al.[17]

as a measure of signal crosstalk from the blocked trap to the trap of interest. Here the parasitic signal $S_{\text{parasitic}}$ is the light intensity measured when only the blocked trap was switched on, and the total signal $S_{\text{total}}$ denotes the intensity measured with both traps being active. It is expected that the amount of crosstalk will depend on the distance between the traps. The closer the traps are, the larger the crosstalk should be. We analyzed this dependency by changing the inter-trap distance between the two trap foci, while continuously recording the transmitted light intensities. The trap of interest was kept in place, while the position of the second trap was varied using the beam steering lens. The results for different pinhole sizes are shown in Fig. 2A. The measurements confirmed that the amount of crosstalk depends on the inter-trap distance and decreases faster for smaller pinholes. The diffraction limited spot size sets a limit to the minimal usable pinhole size.

The presented method can be combined with standard polarization based filtering. To investigate the added value of the presented technique, we compared the performance of this combined method with the standard polarisation based technique. For this purpose, we added a linear polarizer (Thorlabs LPNIR100) in front of the QPD to block the polarized light from the second trap.

With the polarizer but no pinhole installed, the crosstalk was at a constant level just above 1%, in accordance with earlier measurements where exclusively polarisation optics were used for crosstalk reduction.[11] As shown in Fig. 2B, the combination of spatial filtering and polarisation based signal separation allowed for crosstalk levels far below what is achievable with polarisation based filtering alone. Crosstalk levels were as low as 0.2% for a $20\mu$m pinhole, providing a factor five improvement over the standard technique. Notably, the measurements were limited by electronics noise, and not by the method itself. So even lower crosstalk levels, close to zero, appear to be possible.

## 3.1 QPD detection for holographic optical tweezers

The presented method, which was originally developed for crosstalk reduction, will prove useful in the field of holographic optical trapping. Holographic optical tweezers enable convenient generation of multiple traps and have found wide-spread use in various research fields.[7] However, on the detection side, a remaining challenge is to separate the signals from the individual traps for separate photodiode based detection. Photodiode based detection is desirable due to its unrivaled bandwidth, spatial resolution and low cost.

Along the lines of the reported detection for dual traps, it will be possible to position a pinhole such that only light from one individual trap, out of an array of traps, reaches the QPD. The principle advantage over existing methods is that it will be possible to parallelize the detection to allow for simultaneous detection of multiple traps using photodiodes. Current and future efforts are aiming at implementing this combination of holographic optical tweezers and the reported detection technique.

## 4. SUMMARY

Here we have presented a method for fast and simultaneous photodiode based detection of multiple optical traps. It was experimentally shown that performing spatial filtering in a conjugate plane to the sample plane allows for efficient suppression of crosstalk from a nearby trap. Combining the method with established polarisation based signal separation further reduced crosstalk to levels as low as 0.2%. By parallelizing this method, i.e., using several pinholes to detect several traps simultaneously, we will be able to track the position and measure forces of multiple traps in holographic optical tweezers.
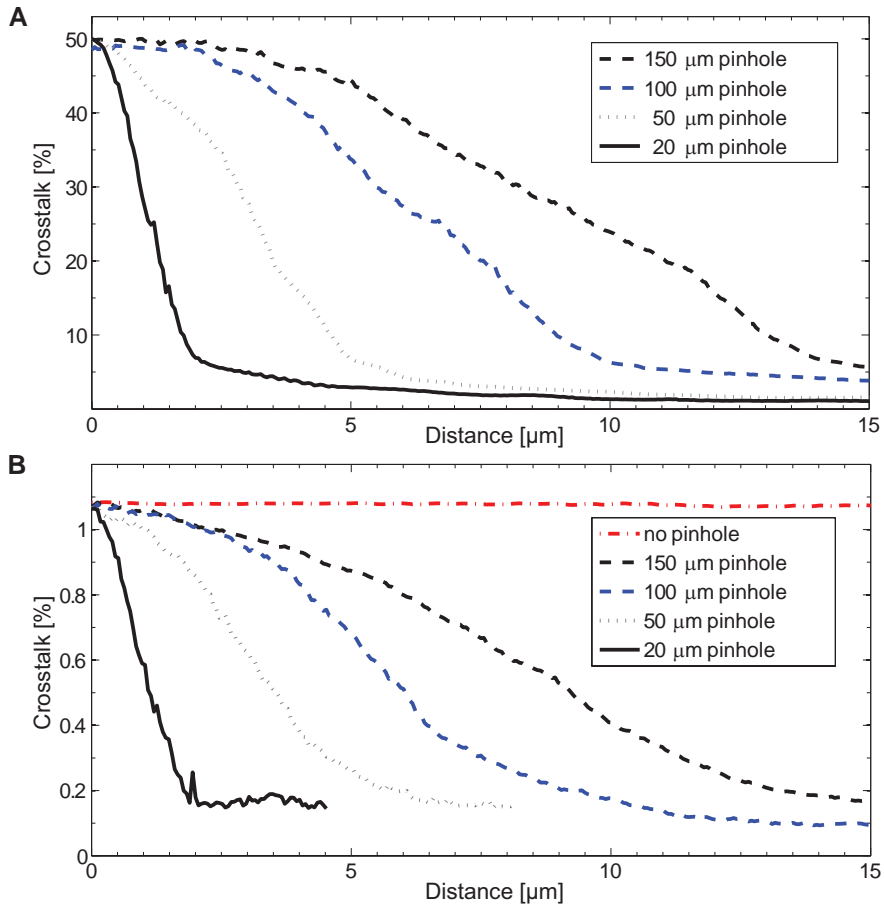
## ACKNOWLEDGMENTS

Figure 2. Crosstalk suppression. A) The dependence of crosstalk Ψ on inter-trap distance is shown for different pinhole sizes. Smaller pinholes allow for more effective crosstalk suppression at shorter inter-trap distances. B) Same as in A), but now for a combined spatial filtering and polarisation based signal separation. A factor five improvement over the standard technique, i.e., with polarisation only (dot-dash red line), can be achieved for small pinholes at trap-trap distances of more than $2\mu m$ (full black line). Figures adapted from Ref. 1.

# REFERENCES

[1] Ott, D., Reihani, S. N. S., and Oddershede, L. B., "Crosstalk elimination in the detection of dual-beam optical tweezers by spatial filtering," *Review of Scientific Instruments* **85**(May), 053108 (2014).

[2] Ashkin, A., Dziedzic, J. M., Bjorkholm, J. E., and Chu, S., "Observation of a single-beam gradient force optical trap for dielectric particles," *Optics Letters* **11**, 288 (May 1986).

[3] Neuman, K. C. and Block, S. M., "Optical trapping," *Review of Scientific Instruments* **75**, 2787–809 (Sept. 2004).

[4] Perkins, T., "Optical traps for single molecule biophysics: a primer," *Laser & Photonics Review* **3**, 203–220 (Feb. 2009).

[5] Dufresne, E. R., Spalding, G. C., Dearing, M. T., Sheets, S. A., and Grier, D. G., "Computer-generated holographic optical tweezer arrays," *Review of Scientific Instruments* **72**(3), 1810 (2001).

[6] Moffitt, J. R., Chemla, Y. R., Smith, S. B., and Bustamante, C., "Recent advances in optical tweezers.," *Annual Review of Biochemistry* **77**, 205–28 (Jan. 2008).

[7] Dholakia, K. and Čižmár, T., "Shaping the future of manipulation," *Nature Photonics* **5**, 335–342 (June 2011).

[8] Finer, J., Simmons, R., and Spudich, J., "Single myosin molecule mechanics: piconewton forces and nanometre steps," *Nature* **368**, 113–119 (1994).

[9] Fazal, F. M. and Block, S. M., "Optical tweezers study life under tension.," *Nature Photonics* **5**, 318–321 (May 2011).

[10] Gross, P., Laurens, N., Oddershede, L. B., Bockelmann, U., Peterman, E. J. G., and Wuite, G. J. L., "Quantifying how DNA stretches, melts and changes twist under tension," *Nature Physics* **7**, 731–736 (May 2011).

[11] Atakhorrami, M., Addas, K. M., and Schmidt, C. F., "Twin optical traps for two-particle cross-correlation measurements: eliminating cross-talk.," *Review of Scientific Instruments* **79**, 043103 (Apr. 2008).

[12] Mangeol, P. and Bockelmann, U., "Interference and crosstalk in double optical tweezers using a single laser source.," *Review of Scientific Instruments* **79**, 083103 (Aug. 2008).

[13] von Hansen, Y., Mehlich, A., Pelz, B., Rief, M., and Netz, R. R., "Auto- and cross-power spectral analysis of dual trap optical tweezer experiments using Bayesian inference.," *Review of Scientific Instruments* **83**, 095116 (Sept. 2012).

[14] Visscher, K., Gross, S., and Block, S., "Construction of multiple-beam optical traps with nanometer-resolution position sensing," *IEEE Journal of Selected Topics in Quantum Electronics* **2**(4), 1066–1076 (1996).

[15] Reihani, S. N. S., Mir, S. A., Richardson, A. C., and Oddershede, L. B., "Significant improvement of optical traps by tuning standard water immersion objectives," *Journal of Optics* **13**, 105301 (Oct. 2011).

[16] Gittes, F. and Schmidt, C. F., "Interference model for back-focal-plane displacement detection in optical tweezers.," *Optics Letters* **23**, 7–9 (Jan. 1998).

[17] Hansen, P. M., Tolić-Nørrelykke, I. M., Flyvbjerg, H., and Berg-Sørensen, K., "tweezercalib 2.0: Faster version of MatLab package for precise calibration of optical tweezers," *Computer Physics Communications* **174**, 518–520 (Mar. 2006).

# Revealing Hidden Dynamics within Living Soft Matter

**Dino Ott, Poul M. Bendix, and Lene B. Oddershede**[*]

Niels Bohr Institute, University of Copenhagen, 2100 Copenhagen, Denmark

**ABSTRACT** In the study of living soft matter, we often seek to understand the mechanisms underlying the motion of a single molecule, an organelle, or some other tracer. The experimentally observed signature of the tracer is masked by its thermal fluctuations, inherent drift of the system, and instrument noise. In addition, the timing or length scales of the events of interest are often unknown. In the current issue of *ACS Nano*, Chen *et al.* present a general method for extracting the underlying dynamics from time series. Here, we provide an easily accessible introduction to the method, put it into perspective with the field, and exemplify how it can be used to answer important out-standing questions within soft matter and living systems.
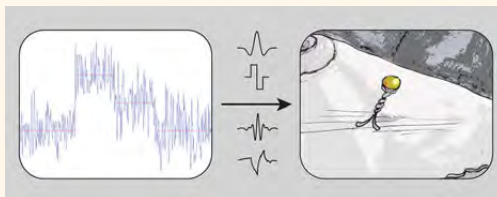
M otility at the nanoscale in living soft matter can be highly complex as the environment is often compartmentalized and hosts both passive and active processes.[1−3] This causes the tracers of interest, *e.g.*, single molecules, to undergo heterogeneous dynamics, and their experimentally observed trajectories are further complicated by the action of stochastic forces, originating both from the tracer's thermal fluctuations and from the inherent noise of the equipment and detection systems. To identify the locations of certain types of behaviors in time and space correctly, a scientist has to be equipped with experimental and analytical tools allowing the extraction of signals from noisy backgrounds. The standard output from many experiments consists of lengthy time series recordings of molecular dynamics or tracking of either endogenous objects or externally added tracer particles. The events of interest contained in such time series may occur randomly in time and furthermore be embedded within random noise. This renders extraction and the following correct interpretation of the data challenging. Existing analytical methods to discriminate active or anomalous behavior from random noise include the application of physical models in which thresholds are assigned to separate Brownian noise from heterogeneous events.[4] Also, transformation

of time recordings into the frequency domain is frequently used to extract spectral information about biophysical processes and has been applied in the analysis of, *e.g.*, acto-myosin networks to identify nonequilibrium activity fueled by ATP hydrolysis.[1] However, spectral analysis based on Fourier transformations, even short time Fourier transformations, are best suited for analyzing stationary processes in which the localization of certain events in the time domain is not necessary. The abundance of processes in nature exhibiting nonstationary behavior renders analysis purely in frequency domain inadequate since all information regarding the localization of events in the time domain is lost.

The localization of events in time is utterly important, *e.g.*, for understanding signaling processes, cellular trafficking, or the highly nonrandom chromosomal organization within the nucleus and how this relates to the cellular clock. Therefore, we are in need of general methods that both provide information regarding the scale of heterogeneous events and are able to localize biophysical events in time. This would allow robust extraction of important information embedded within time series originating from living cells and soft matter systems. Inspired by previous work[5,6] and by the challenges met during the analysis of nanoscale soft matter systems, Chen *et al.* present in the current issue of *ACS*

* Address correspondence to
oddershede@nbi.dk.

The abundance of processes in nature exhibiting nonstationary behavior renders analysis purely in frequency domain inadequate since all information regarding the localization of events in the time domain is lost.

Nano[7] a general wavelet-based method that can discriminate heterogeneous behavior from random noise in time series. They elegantly do this by applying a multiscale wavelet transform, thus preserving both the information contained in the time domain and the scale of the heterogeneous events. The success rate of the method in detecting heterogeneous events is tested both on simulated data and on real data obtained from three distinct areas of science. The methodology is independent of predefined physical models, thus making it powerful for analyzing time series originating from many different research fields. As outlined below, we expect this methodology to advance the field of nanoscale motility significantly, thereby answering important questions regarding fundamental transport mechanisms within living soft matter systems. In particular, new information is needed and will arise on the topic of nuclear organization and transportation in relation to the cell cycle, and light will be shed on the complicated aging mechanisms that give rise to weak ergodicity breaking in living organisms and how this alters the inherent cellular dynamics.

**Wavelet Analysis (WLA).** The so-called 'wavelet transform' mathematical technique was established in the 1980s and is now widely used for digital signal processing, such as

in image compression, denoising, and pattern recognition.[8] Wavelet transform analysis allows for local, time-resolved, multiscale detection of dynamic processes in time series, revealing important features that various other established signal analysis techniques, like the Fourier transform, fail to do. For instance, the WLA method has been used for characterizing the rotational and translational Brownian motion of a nanostructure that changes size over time;[6] however, it has not yet found widespread use for the analysis of soft matter living systems. The paper of Chen *et al.* shows that WLA is a most useful and advantageous technique for nanoscale soft matter systems as well, and the following section will take the reader through a 'crash-course' on WLA.

The WLA method comprises the three following steps: (i) To analyze a given time series (as shown in Figure 1A), one chooses a wavelet. Wavelets can take different forms and their capabilities to detect certain signal features are well-known.[5,8] A wavelet is a function that is square integrable and that integrates to zero. Typically, a wavelet is limited in time and could be a single oscillation, *e.g.*, the commonly used Haar wavelet shown in Figure 1B. (ii) During the wavelet transform, the time-dependent data, *e.g.*, the trajectory of a single marker, is transformed into a time- and scale-dependent representation of the original data (shown in Figure 1C). Mathematically, this involves convolution of the time series with scaled and translated versions of the wavelet. Translation simply means moving the wavelet along the time axis and forms the basis for locating the dynamics of interest in time, whereas scaling is achieved by stretching/compression of the wavelet in time and provides information on the scale of the dynamics. This scaling of the wavelet allows one to conduct the time series analysis on multiple scales without being bound to a specific scale. In other words, the transformation returns information regarding at which points in time

and on which scale the features of the wavelet match the time series. This information is given by the color scale in Figure 1C. In practice, the transformation is easy to conduct due to the availability of easily accessible toolboxes in, *e.g.*, MATLAB (MathWorks) and Mathematica (Wolfram Research). (iii) In the final step, the researchers impose a physically motivated restriction to a range of scales on which the heterogeneous dynamics are expected to occur, and an adaptive universal threshold is set. This threshold (a certain color between blue and pink in Figure 1C) serves as the decision criterion for classifying the type of dynamics and identifying dynamical heterogeneity. In the current issue of *ACS Nano*, Chen *et al.* present a general wavelet-based method that can discriminate heterogeneous behavior from random noise in time series.

By applying this methodology to analyzing the trajectories of fluorescently labeled endosomes in living cells, Chen *et al.* demonstrate the potential for detecting the switching between changing dynamics, in this case between active transport and passive diffusion (as sketched in Figure 2).

Furthermore, the authors conduct a performance evaluation using simulated data and show that the method is rather insensitive to multiple noise sources. The generality of the WLA method makes it valuable for analyzing time series of different origin. Moreover, it not only provides the means for more detailed insights, but also, importantly, precludes false

In the current issue of *ACS Nano*, Chen *et al.* present a general wavelet-based method that can discriminate heterogeneous behavior from random noise in time series.
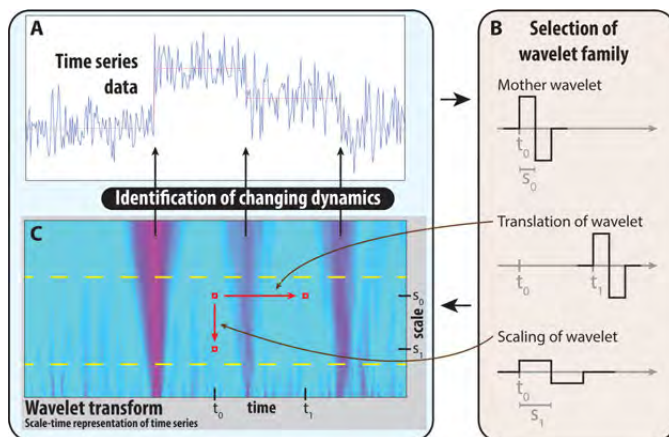
**Figure 1.** Wavelet analysis in a nutshell: (A) time series displaying discrete steps that are masked by stochastic noise. (B) the commonly used Haar wavelet, its translation, and scaling. (C) result of convoluting the time series shown in (A) with scaled and translated Haar wavelets. The color map shows the goodness of the match of the wavelet with the time series as the wavelet is moved in time (horizontal red arrow) and scaled (vertical red arrow). The area between the yellow lines denote the scales of interest and in the colormap, pink colors signify strong correlations and hence identify the masked steps in the time series shown in (A)).

conclusions from being drawn when blindly assuming homogeneous dynamics.

**Inside Cells.** The dynamics of single molecules or organelles inside living cells are known to be rich, complex, and of diverse character and origin.[9] Tracing individual molecules provides insight into the fundamental processes responsible for trafficking, signaling, and gene regulation inside living cells. There are several technical challenges connected to retrieving reliable trajectories of individual molecules inside the living cell. First, the molecules of interest need to carry a label (*e.g.*, a fluorescent marker) such that they can be followed in two or three dimensions. Some organelles (*e.g.*, lipid granules)[10] are relatively large and carry enough contrast themselves that they are visible in the microscope and need no further labeling. The technique of single particle tracking is extremely useful for tracing individual molecules or particles inside living cells, but optical traps operated at low laser powers can also provide traces with very high temporal and spatial resolution. A typical time trace is subject to a significant amount

of noise, not the least of which are the thermal fluctuations of the tracer, which are substantial at physiological temperatures and at the single-molecule level.

Inside the cell, most molecules and organelles exhibit subdiffusion, *i.e.*, slower diffusion than in normal Brownian motion. This is the case for single mRNA molecules inside bacteria[11] and also for lipid granules inside yeast.[10] Interestingly, although normal Brownian motion would be a faster way to transport molecules in a passive manner, subdiffusion is much more abundant in living cells than is Brownian motion. This could be due to two factors: one is that the cytoplasm needs to be tightly packed and dense in order to accommodate all the necessary cellular machinery, and the second is that it might be advantageous for a process involving a protein binding to DNA or RNA, for example, that the proteins or nucleic acids do not diffuse away quickly but rather stay in the vicinity of their correct targets longer, thus increasing the chance of successful attachment.

In addition to these passive types of motility, there is also active, biochemical energy-consuming transport inside living cells, for instance

of myosin along actin inside muscle cells or kinesin-mediated transportation along microtubules,[12] as sketched in Figure 2. Further complicating the picture, a given tracer, for example an endosome, may at certain times experience passive thermal diffusion and at other times active transport. The challenge of the scientist is then to deduce backward, from the observed heterogeneous time trace to the basic mechanisms governing the motion.

Another environment displaying highly heterogeneous dynamics that presently is gaining a great deal of attention is inside the nucleus. Chromosomes are spatially organized in the nucleus, where diffusion is extremely slow; it has been shown that the telomeres certainly do not explore the entire nucleus.[13] In addition, it was recently shown that certain genetic sequences mediate transportation of genetic information to a specific location.[14] Hence, nuclear transportation is highly regulated and far from random; however, still very little is known about the dynamics of the nucleus that are highly important for correct genetic regulation and expression.
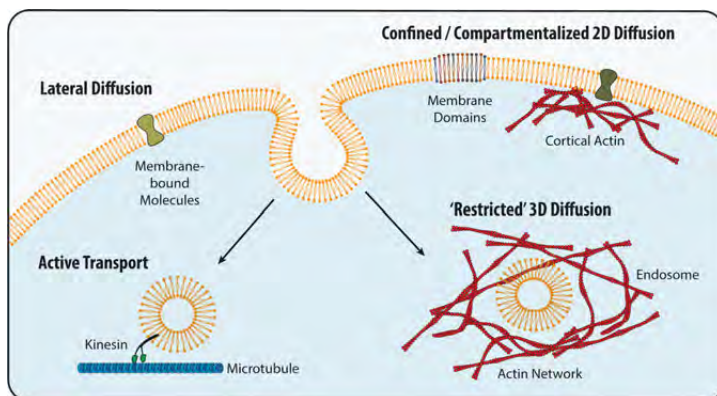
**Figure 2. Sketch of the variety of transport mechanisms inside living cells. Proteins restricted to the membrane perform lateral diffusion, this possibly being complicated by the presence of membrane domains containing other types of lipids or by tethering or confinement of the protein by the underlying cortical actin mesh. Inside the cell, a tracer can perform passive thermal diffusion, but this process is hindered by the presence of the cytoskeleton and other cellular components. Furthermore, molecular motors, for instance kinesin, perform active transportation of cargos inside the living cell.**

From the single-molecule or particle trajectories, it can be rather difficult to distinguish one type of motion from another and different measures exist for this purpose. One frequently applied measure is the mean square displacement, MSD = $\langle (x(t) - x(t_0))^2 \rangle \sim t^{\alpha}$, where the exponent, $\alpha$, provides information regarding whether the motion is confined ($\alpha = 0$), subdiffusive ($0 < \alpha < 1$), normal ($\alpha = 1$), or superdiffusive ($\alpha > 1$). Another useful method is the mean maximal excursion method,[15] which can be used to determine the physical nature underlying the observed stochastic motion. However, two major problems faced during *in vivo* detection are the noise and drift inherently present in experimental data taken at the single-molecule level over extensive periods of time. Also, it is most often not known *a priori* at which time and spatial scales the phenomenon of interest is taking place. It is likely that the multiscale wavelet method presented in this issue of *ACS Nano*[7] can overcome some of these challenges as the method extracts features without limiting the search to a certain time or spatial interval, while also being quite robust with respect to noise.

> It is likely that widespread use of the multiscale wavelet method will significantly advance the field and expand our knowledge on the origin of stochastic motion inside living systems.

**Ergodic *versus* Nonergodic Behavior.** Recent reports have shown that time averages obtained over *in vivo* single-particle traces often are not reproducible. In other words, ensemble averages do not yield the same results as temporal averages, which means that one of the hallmarks of ergodicity is violated.

This phenomenon has been observed both for lipid granules in living yeast cells[16] and, at certain locations, in living endothelial cells,[17] as well as for membrane proteins.[18] As living organisms undergo life cycles and age over time, it is reasonable that their physical observables

also change properties with time and that such systems therefore violate strict ergodicity.

In the above-mentioned experiments, not all hallmarks of ergodicity are broken, only some of them, and therefore, this effect has been named 'weak ergodicity breaking'. The concept of weak ergodicity breaking is currently highly debated; it is certainly not yet well-defined and poses serious challenges to statistical physics. One of the problems is the difficulty in pointing out the signatures that may provide clues as to the underlying processes from time traces. Moreover, it is likely that tracers at certain time scales exhibit ergodic behavior, possibly well described by the fractional Brownian motion, whereas at other time scales, the tracer's dynamics may be better defined by a continuous time random walk, which has nonergodic properties. The scientific community interested in anomalous diffusion has long been in need of tools to distinguish between different stochastic models, and it is likely that widespread use of the multiscale wavelet method will significantly advance the field and expand our knowledge on the origin of stochastic motion inside living systems.
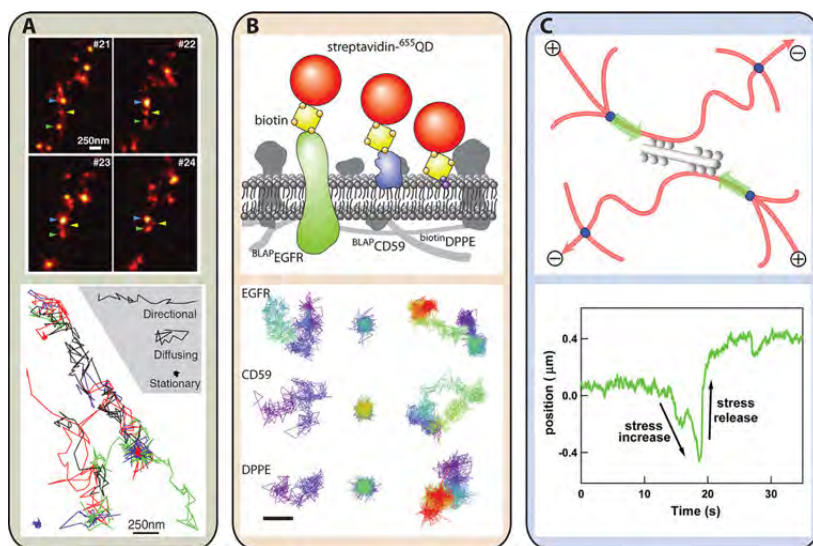
**Figure 3.** Heterogeneous dynamics in membranes and reconstituted systems. (A) Upper images show stimulated emission depletion images of fluorescently labeled synaptic vesicles. The lower plot shows the two-dimensional vesicle motility, which exhibits signs of stationarity, directional motion, and normal diffusion. Reprinted with permission from ref 2. Copyright 2008 American Association for the Advancement of Science. (B) Upper sketch shows a schematic drawing of the epidermal growth factor receptor (EGFR) transmembrane protein, the CD59 lipid anchored protein, and the DPPE glycerophospholipid (1,2-dipalmitoyl-*sn*-glycero-3-phosphoethanolamine), all specifically attached to quantum dots. The lower figure shows the traces of these proteins and lipids inside the membrane of mouse fibroblast cells, the scale bar is 400 nm. Reprinted from ref 20. Copyright 2013 American Chemical Society. (C) Upper drawing shows how the sliding of myosin filaments along actin cables generates tension in the actin network. Lower graph shows that the contractile event is detected by probe particles embedded in the actin network. Reprinted with permission from ref 1. Copyright 2007 American Association for the Advancement of Science.

**Membrane Dynamics.** Membranes are essential components of living systems, and the lipids composing the membranes as well as the proteins embedded therein display highly interesting dynamics at different levels. Within the two-dimensional membrane sheet, proteins undergo different types of lateral diffusion dictated by the phase state of membrane domains as well as by interactions with cytoskeletal elements (as sketched in Figure 2). Inside the cytoplasm, trafficking of endosomal membranes takes place by vesicle diffusion and active transport through the cytoplasm, a process which is important to understand in the context of nanomedicine delivery.[19] Super-resolution microscopy techniques enable localization of multiple fluorescent markers with spatial resolution down to 20 nm, and are thus powerful tools to extract time series displaying heterogeneous dynamics from living and soft-matter

systems. Recently, experiments performed using stimulated emission depletion (STED) microscopy revealed that synaptic vesicle mobility in the boutons of axons performs stick-and-diffuse motion due to the transient association of vesicles with cellular elements[2] (Figure 3A). The data analysis used in ref 2 relied on both temporal averaging and some user-defined thresholds to identify 'hot spots' where vesicles became transiently trapped. The WLA method presented in this issue of *ACS Nano*[7] would enable a more objective treatment of the raw data obtained from super-resolution microscopy and could likely retrieve new hidden dynamics embedded within the time traces acquired.

New developments with ultra-sensitive high-speed cameras have allowed tracking of membrane proteins diffusing in the two-dimensional plasma membrane with impressive

time resolution[20,21] (Figure 3B). Data from such experiments has fundamentally contributed to our understanding of how the underlying actin matrix interacts with the membrane and the cytoplasmic domain of transmembrane proteins. The cytoskeleton splits the membrane into compartments and causes the membrane proteins to perform hop-diffusion between the individual membrane compartments;[21] examples of such hop-diffusion motility within membranes are shown in Figure 3 for a transmembrane protein (epidermal growth factor receptor, EGFR), a lipid-anchored protein (CD59), and a glycerophospholipid (1,2-dipalmitoyl-*sn*-glycero-3-phosphoethanolamine, DPPE).[20] In this context, an unresolved question remains regarding the effect on the diffusional motion from disputed membrane rafts. It is known that diffusion in liquid disordered domains

> *Existing data cries out for more sophisticated methods of analysis that are capable of extracting the underlying interesting heterogeneous dynamics, which are the footprints of the biological processes.*

is only approximately twice that in liquid ordered domains (resembling these rafts) and it is rather challenging to detect the dynamic partitioning of lipids or proteins between different domains. Here, wavelet analysis could be an appropriate analytical tool to improve the analyses of such data and to contribute to the understanding of the nanoscale membrane structure and motility within membranes.

**In Vitro Reconstituted Biological Systems.** To elucidate the cellular dynamics and cytoskeletal architecture in a more detailed manner, it is often beneficial to design and to study an artificial system composed of only a few essential components selected from the complex *in vivo* system. A simplified *in vitro* reconstituted and minimal system allows for investigation of the influence of one well-controlled parameter at a time. For instance, the influence of the network structure on tracer diffusion has been studied successfully in an actin network where the actin concentration was varied in a controlled manner.[22] In this and other *in vitro* studies of crowded environments, subdiffusion appears to be the predominant passive motility mode. To elucidate how myosin motors collectively remodel an actin network, the before-mentioned experiment was further developed by adding molecular motors to the actin network.[1,23] Myosin motors from bundles would walk along the actin filaments and create

substantial tension in the actin network, as depicted in Figure 3C. In the analysis of Stuhrman *et al.*,[23] they used thresholds to segment the time series locally to discriminate between oriented and random motion. In general, even reconstituted biological systems display rich heterogeneity and could benefit greatly from WLA to extract quantitative information of the hidden dynamics.

## OUTLOOK AND FUTURE CHALLENGES

Wavelet analysis has by no means yet reached its full potential in the life sciences. A combination of WLA and new experimental techniques, like super-resolution microscopy, provides powerful tools to unravel detailed kinetics embedded within time series recordings of processes in living systems. The examples presented above point to the fact that there already exists a huge amount of data on anomalous diffusion of tracers displaying heterogeneous dynamics. Although much valid analysis has been done, existing data cries out for more sophisticated methods of analysis that are capable of extracting the underlying interesting heterogeneous dynamics, which are the footprints of the biological processes. It is straightforward to use the multiscale wavelet method, presented in the current issue of *ACS Nano*, to this overwhelming amount of existing data and thereby uncover fundamental new insights hidden in the original analyses.

## REFERENCES AND NOTES

1. Mizuno, D.; Tardin, C.; Schmidt, C. F.; Mackintosh, F. C. Nonequilibrium Mechanics of Active Cytoskeletal Networks. *Science* **2007**, *315*, 370–373.
2. Westphal, V.; Rizzoli, S. O.; Lauterbach, M. A.; Kamin, D.; Jahn, R.; Hell, S. W. Video-Rate Far-Field Optical Nanoscopy Dissects Synaptic Vesicle Movement. *Science* **2008**, *320*, 246–249.
3. Pierce, S. K.; Liu, W. The Tipping Points in the Initiation of B Cell Signalling: How Small Changes Make Big Differences. *Nat. Rev. Immunol.* **2010**, *10*, 767–777.
4. Arcizet, D.; Meier, B.; Sackmann, E.; Rädler, J.; Heinrich, D. Temporal Analysis of Active and Passive Transport in Living Cells. *Phys. Rev. Lett.* **2008**, *101*, 248103.
5. Daubechies, I. *Ten Lectures on Wavelets*; SIAM: Philadelphia, PA, 1992.
6. Yang, H. Detection and Characterization of Dynamical Heterogeneity in an Event Series using Wavelet Correlation. *J. Chem. Phys.* **2008**, *129*, 074701.
7. Chen, K.; Wang, B.; Guan, J.; Granick, S. Diagnosing Heterogeneous Dynamics in Single Molecule/Particle Trajectories with Multiscale Wavelets. *ACS Nano* **2013**, DOI: 10.1021/nn402787a.
8. Percival, D. B.; Walden, A. T. *Wavelet Methods for Time Series Analysis*; Cambridge University Press: Cambridge, U.K., 2006.
9. Barkai, E.; Garini, Y.; Metzler, R. Strange Kinetics of Single Molecules in Living Cells. *Phys. Today* **2012**, *65*, 29.
10. Tolić-Nørrelykke, I.; Munteanu, E.-L.; Thon, G.; Oddershede, L.; Berg-Sørensen, K. Anomalous Diffusion in Living Yeast Cells. *Phys. Rev. Lett.* **2004**, *93*, 078102.
11. Golding, I.; Cox, E. Physical Nature of Bacterial Cytoplasm. *Phys. Rev. Lett.* **2006**, *96*, 098102.
12. Schnitzer, M. J.; Block, S. M. Kinesin Hydrolyses One ATP per 8-nm Step. *Nature* **1997**, *388*, 386–390.
13. Bronstein, I.; Israel, Y.; Kepten, E.; Mai, S.; Shav-Tal, Y.; Barkai, E.; Garini, Y. Transient Anomalous Diffusion of Telomeres in the Nucleus of Mammalian Cells. *Phys. Rev. Lett.* **2009**, *103*, 018102.
14. Jakociunasa, T.; Jordo, M. D.; Mebareka, M. A.; Bunnera, C. M.; Verhein-Hansen, J.; Oddershede, L. B.; Thon, G. Subnuclear Relocalization and Silencing of a Chromosomal Region by an Ectopic rDNA Repeat. *Proc. Natl. Acad. Sci. U.S.A.* **2013**, in press.
15. Tejedor, V.; Bénichou, O.; Voituriez, R.; Jungmann, R.; Simmel, F.; Selhuber-Unkel, C.; Oddershede, L. B.; Metzler, R. Quantitative Analysis of Single Particle Trajectories: Mean Maximal Excursion Method. *Biophys. J.* **2010**, *98*, 1364–1372.
16. Jeon, J.-H.; Tejedor, V.; Burov, S.; Barkai, E.; Selhuber-Unkel, C.; Berg-Sørensen, K.; Oddershede, L.; Metzler, R. *In Vivo* Anomalous Diffusion and Weak Ergodicity Breaking of Lipid Granules. *Phys. Rev. Lett.* **2011**, *106*, 048103.
17. Leijnse, N.; Jeon, J. H.; Loft, S.; Metzler, R.; Oddershede, L. B. Diffusion Inside Living Human Cells. *Eur. Phys. J.: Spec. Top.* **2012**, *204*, 75–84.
18. Weigel, A. V.; Simon, B.; Tamkun, M. M.; Krapf, D. Ergodic and Nonergodic Processes Coexist in the Plasma Membrane as Observed by

Single-Molecule Tracking. *Proc. Natl. Acad. Sci. U.S.A.* **2011**, *108*, 6438–6443.

19. Zhao, F.; Zhao, Y.; Liu, Y.; Chang, X.; Chen, C.; Zhao, Y. Cellular Uptake, Intracellular Trafficking, and Cytotoxicity of Nanomaterials. *Small* **2011**, *7*, 1322–1337.

20. Clausen, M.; Lagerholm, B. Visualization of Plasma Membrane Compartmentalization by High-Speed Quantum Dot Tracking. *Nano Lett.* **2013**, *13*, 2332–2337.

21. Kusumi, A.; Shirai, Y. M.; Koyama-Honda, I.; Suzuki, K. G. N.; Fujiwara, T. K. Hierarchical Organization of the Plasma Membrane: Investigations by Single-Molecule Tracking *vs.* Fluorescence Correlation Spectroscopy. *FEBS Lett.* **2010**, *584*, 1814–1823.

22. Wong, I.; Gardel, M.; Reichman, D.; Weeks, E.; Valentine, M.; Bausch, A.; Weitz, D. Anomalous Diffusion Probes Microstructure Dynamics of Entangled F-Actin Networks. *Phys. Rev. Lett.* **2004**, *92*, 178101.

23. Stuhrmann, B.; Soares e Silva, M.; Depken, M.; MacKintosh, F. C.; Koenderink, G. H. Nonequilibrium Fluctuations of a Remodeling *In Vitro* Cytoskeleton. *Phys. Rev. E* **2012**, *86*, 020901.